Emerging Quantum Correlations from Interacting Fibre-Cavity Polaritons

By

Andrew Wood

A thesis submitted to Macquarie University
for the degree of Doctor of Philosophy
Department of Physics and Astronomy
October 2019

MACQUARIE
University
SYDNEY · AUSTRALIA

© Andrew Wood, 2019.

Typeset in LaTeX 2_ε.

Except where acknowledged in the customary manner, the material presented in this thesis is, to the best of my knowledge, original and has not been submitted in whole or part for a degree in any university.

Andrew Wood

Acknowledgements

This PhD candidature has been a great struggle for me, and as with many things in life, was full of problems and bad luck. However, I have made it through with the help of alot of important people to whom I wish to bestow my deepest gratitude. To Thomas Volz, my supervisor. Thank you for the opportunity to continue my studies, for your guidance and for your wisdom. We got there in the end, despite all the hurdles.

To my family, especially mum who pushed me all the way, even when I felt like giving up numerous times. Without you all propping me up, encouraging me to persevere, comforting me, guiding me and helping me complete this thesis, I wouldn't be here at one of my greatest achievements in my life. Also, a big thank you to Amy for doing the proof-reading. Words cannot express the overwhelming thanks and praise for you all. I am eternally indebted to you, and I love you all dearly.

To Guillermo Muñoz-Matutano: the brains behind the operation. To put it simply mate, this project would not have gotten off the ground if it were not for you knowledge, skill and expertise. We battled with this project and we put in alot of hard yards with long weeks of taking measurements, but we found our treasure. My complete thanks for your guidance and mentoring and putting up with me through these last few years as well as the riveting games of kicker/fusball. You will go far my friend!

To Xavi Vidal: you got me started on the way with this project and without your input, I would still be stuck firmly at square one. Thank you for your guidance and insight which started me off on this journey.

To Mattias Johnsson, who nutted out alot of the theoretical work. Your knowledge and insight gave us the model we needed to know where to look in our experiments. Your discussions with me on how the model worked and the implications helped me understand the subtleties of the phenomenon and helped me write this thesis. Your work also gave us a fantastic paper. Thank you for your patience with me and your support.

To my friends which I didn't see alot of during this PhD in and outside of uni, especially a certain Thomas Guff. The times we had together were always fun and I felt so included when I was with you. I'm sorry I haven't been a better friend: this PhD has been a struggle and has taken alot of my time and energy. I hope you all reach the stars and live happy, long lives. Thank you for your support and friendship.

To the staff at CSIRO, especially the canteen staff. Thank you for all your help with issues in the lab, getting us the parts we needed, keeping me fed and the awesome games of kicker/fusball. Working with you in such an institution was humbling and inspiring. Thank you for your support and generosity.

And, although I know you will most likely never read this, to Jane. Although we didn't make it together, your love, support, nurturing and just being there helped drive me to get to the finish line. I simply could not have done this without you. I owe you an unrepayable debt and give to you my loving thanks and best wishes. Know that I am truly and deeply sorry and that I'm trying, with greatest earnestness, to be a better person.

And finally, I would like to congratulate myself. This has been an unbelievably arduous journey for me and I have sacrificed too much to put words onto these pages. Andrew, you should be proud of yourself for staying with it, overcoming the hard obstacles and most importantly, not giving up on yourself. You've shown everyone you can do it. You have made it, and life awaits you.

Again, to everyone who helped me make this happen, words will never be enough to convey my unwavering and deepest thanks and love. . . . . .words will never be enough.

This thesis is for you all.

And trust me, I'm (going to be) a doctor. . . . . . .

"The aim of science is not to open the door to infinite wisdom, but to set a limit to infinite error."

in "Life of Galileo", Bertolt Brecht

List of Publications

- G. Muñoz-Matutano, A. Wood, M. Johnsson, X. Vidal, B. Q. Baragiola, A. Reinhard,A. LemaÃőtre, J. Bloch, A. Amo, G. Nogues, B. Besga, M. Richard, and T. Volz. *Emergence of quantum correlations from interacting fibre-cavity polaritons.* NatureMaterials **18**(3), 213 (2019). URL https://doi.org/10.1038/s41563-019-0281-z.
- A. Wood, X. Vidal, G. Muñoz-Matutano, and T. Volz. *Non-invasive zero-delaytime calibration of hanbury-brown and twiss interferometers.* Measurement **137**, 562 (2019). URL http://www.sciencedirect.com/science/article/pii/S0263224119300880.

Abstract

The research presented in this thesis reports on experimental investigations into photon-photon interactions facilitated by strongly interacting microcavity polaritons. We use a highly flexible fibre Fabry-Pérot microcavity setup to impose photonic-mode confinement of the polariton mode to create zero-dimensional polariton boxes. The strong optical confinement afforded by the geometries of the fibre mirror, polariton interactions are effectively enhanced, introducing significant system nonlinearities noticeable at the single particle level. This nonlinear behaviour results in the polariton blockade regime where the system can only support one polariton at a time and observable through the antibunching of the transmitted photons.

Using the excellent tunability of the fibre microcavity, we probe the lower polariton (LP) mode from which we measure the photon statistics of the transition. Under pulsed, resonant excitation, we selectively excite the polariton transition. We observe photon antibunching of $g^{(2)}(0) = 0.93 \pm 0.04$ which demonstrates the emergence of quantum correlations of interacting polaritons at the single particle level and the onset of the polariton blockade regime. Tuning the resonant laser across the polariton transition from red to blue detuning, we observe the photon statistics change from antibunching to bunching predicted by our modified polariton blockade model. Fitting of the autocorrelation measurements to this model, we find a polariton-polariton nonlinearity of $\hbar g_0 = 0.020 \pm 0.011$ meV$\cdot\mu$m^2. We also report on photon antibunching observed in preliminary photon correlation measurements of confined polaritons under non-resonant excitation.

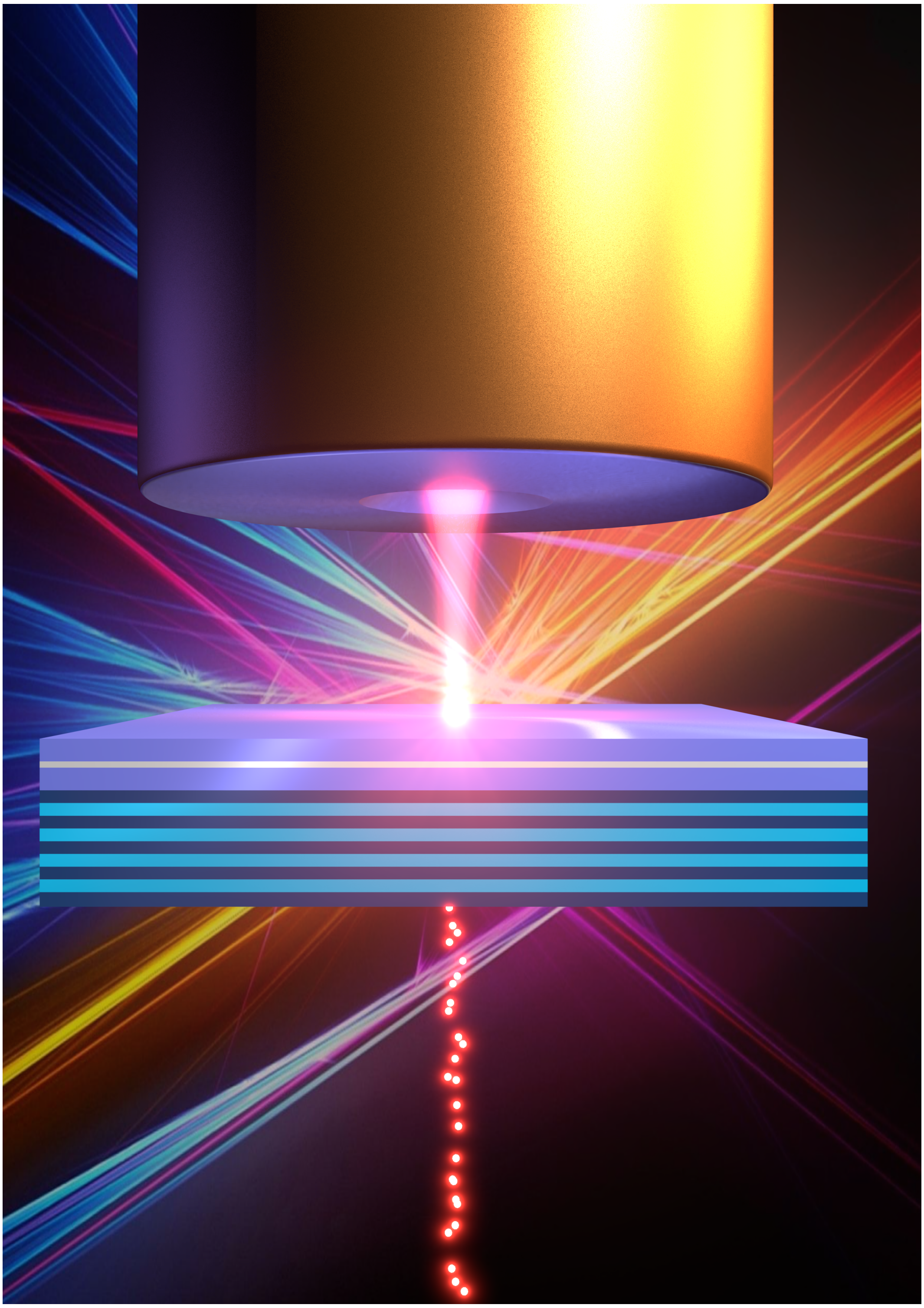

Contents

Acknowledgements **v**

List of Publications **ix**

Abstract **xi**

Contents **xiii**

List of Figures **xv**

1 Introduction **1**

2 Semicondutor Quantum Well Polaritons **9**
2.1 Excitons 9
2.1.1 Quantum Well Excitons 11
2.1.2 Exciton-Exciton Interaction 12
2.2 Microcavity Polaritons 13
2.2.1 Exciton Polaritons 13
2.2.2 Fabry-Pérot Microcavities 16
2.2.3 Microcavities for Polaritons 19
2.3 Photon Correlations 22
2.4 Polariton-Polariton Interaction 23
2.4.1 Polariton Blockade - Photonic Dot 24
2.4.2 Pulsed Excitation Regime 28

3 Experimental Methods **35**
3.1 Experimental Setup - Overview 36
3.1.1 Fibre Cavity Microscope 38
3.2 Fabry Pérot Fibre Microcavity Fabrication 40
3.2.1 Fibre Imaging and Machining System - FIMS 40
3.2.2 Fibre Indentation Analysis 42
3.3 Cavity Mode Simulation with InGaAs Quantum Well Sample 45
3.4 Photoluminescence Spectroscopy 46
3.4.1 Photoluminescence of Microcavity Polaritons 46
3.4.2 Photoluminescence through Excitation 48
3.5 Resonant Transmission of Microcavity Polaritons 49
3.5.1 Resonant Laser Spectroscopy - Polariton Lineshape 50
3.5.2 Resonant Polariton Lifetime 51
3.5.3 Modified Resonant Laser Pulses for Photon Correlations 53

3.6 Photon Correlation Measurement Calibration 56
3.6.1 Optical Cross-talk Calibration 56

4 Quantum-correlated photons from semiconductor cavity polaritons 61
4.1 Photon Correlation of Optically Confined Microcavity Polaritons 61
4.1.1 Photon Correlation Measurements 61
4.1.2 Photon correlation measurement in a second cavity 66
4.1.3 Second order correlation function analysis protocol 67

5 Emerging quantum correlations of non-resonantly excited polaritons 71
5.1 Photon correlations of spectrally filtered polariton photoluminescence 71
5.2 Spectrally filtered polariton photoluminescence 75

6 Conclusion 79

References 81

List of Figures

1.1 ***Quantum many-body system of light.*** *A 2D lattice of photonic crystal cavities, each containing a a nonlinear quantum material, leading to strong, on-site, photon-photon interactions. The interplay between on-site interactions, U, and the photon hopping, κ determines the system dynamics. Such a platform was proposed as a quantum simulator for drive-disspative many-body quantum system. From [1].* 2

1.2 ***Bose-Einstein condensation of microcavity polaritons.*** *Images of the far-field emission distribution of microcavity polaritons as they condense into the lowest momentum state,* $\boldsymbol{k}_{||} = 0$*, as excitation power is increased (left to right). From [2].* 3

1.3 ***Superfluid flow of microcavity polaritons.*** *Experimental images in real space (I-III) and momentum space (IV-VI) of a polariton fluid flow hitting a localised defect. From left to right, the columns show increasing polariton density. In panel III, superfluid flow is established with the suppression of scattering around the defect and the disappearance of the Rayleigh scattering ring in panel VI. From [3].* 4

1.4 ***Microcavity architectures for photonic confinement of microcavity polaritons.*** *Top left: Micropillar cavity constructed using photolithography to etch pillars out of planar QW microcavities. Photons are confined due to the physical shape of the micropillar. From [4]. Top right: Mesa structure etched into the spacer layer of a planar microcavity. The local difference in the spacer layer creates a potential trap for confined photons. From [5]. Bottom left: Photonic crystal cavity structure. A photonic band-gap is created by etching holes in the sample substrate and a cavity is created by the absence of a hole in the structure or defect site. From [6]. Bottom right: Plasmonic microcavity structure cross-section using multilayer trench gratings. From [7].* 5

1.5 ***Fibre Fabry-Pérot microcavity.*** *A single mode fibre tip is machined with a small concave indentation to reduce the mode waist to increase optical confinement of the microcavity polaritons. The air gap between the QW sample and fibre allows for in-situ tuning of the cavity energy over a greater range afforded by other designs.* 6

2.1 ***Wannier Exciton inside a semiconductor crystal lattice.*** *A bound electron-hole pair (red electron, blue hole) with a large Bohr radius extending over several lattice sites (black dots). The non-localised nature of these excitons allows propagation through the lattice.* 10

2.2 ***Band structure of GaAs.*** *The six-fold degeneracy of the valance band electrons divides the electron states into 3 pairs of states, heavy hole (HH), light hole (LH) and split off (SO). The difference in effective masses of the HH and LH electrons lifts the degeneracy of the HH and LH electron bands for $k > 0$. E_Γ is the band-gap energy.* . . . 11

2.3 ***Quantum well exciton.*** *The thick large-energy band-gap GaAs surrounding the thin, low-energy band-gap InGaAs creates a confinement potential for the electron and hole states, in the growth direction, z, of the QW. The resulting quantised excitonic states can be optically accessed with typical transition energies of in our case, near 1.46 eV* . . . 12

2.4 ***2D microcavity with QW.*** *To achieve maximum coupling of the QW excitons to the cavity mode, the QW is placed at the anti-node of the electric field inside the cavity. The polariton dispersion curves can be obtained using angle resolved photoluminescence. Image taken from [2].* . . . 14

2.5 ***Exciton polariton dispersion curves.*** *Cavity-exciton detuning is $\Delta = 0$ meV. The curvature of both upper (blue) and lower-polariton (orange) branches is inherited from the photonic-dispersion relation. The black dashed lines denote the bare exciton and photon dispersion relations respectively.* . . . 15

2.6 ***Zero dimensional polariton dispersion curves.*** *0D polaritons at a cavity-exciton detuning is $\Delta = 0$ meV. The discrete intervals of emission demonstrated by the green and red ovals for the LP and UP respectively across momentum space is a result of in-plane confinement of the polaritons. The orange and blue lines denote the bare (2D) polariton modes and the black dashed lines are the bare exciton and photon dispersion relations respectively.* 16

2.7 ***Planar microcavity profile.*** *The DBR layers sandwich the cavity layer which is on the order of a few wavelengths of light. The DBR layers almost completely reflect light back into the cavity, reducing the cavity loss rate and at the same time helping to maintain large electric field amplitudes inside the cavity.* . . . 17

2.8 ***Stopband function for a dielectric DBR.*** *The calculated stopband function for a DBR with 33 paired layers of Ta_2O_5/SiO_2 at 830nm. The blue curve shows reflection efficiency of the cavity. The large high reflectivity window centred at 830nm is know as the stopband. Increasing the number of layers, in principle, reduces the stopband window and increases the reflectivity of the cavity. In practice however, residual absorption in the layers effectively limits the achievable reflectivity (see chapter 3.3).* . . . 18

2.9 ***Electric field distribution for a dielectric DBR.*** *The electric field distribution for the DBR. The red line is the DBR profile while the blue is the electric field intensity.* . . . 19

2.10 ***Planar microcavity with embedded QW.*** *The QW layer (yellow) is sandwiched between two DBR mirrors (alternating dark blue/light blue) which produces a maximum of the electric field at the QW layer (yellow), shown by the red solid line.* . . . 20

2.11 ***Fibre microcavity with embedded QW.*** *The fibre microcavity design replaces one of the integrated, semi-conductor DBR mirrors with a machined fibre tip with a DBR mirror coating. Since the electric field distribution is dependent on $n^2(z)|E(z)|^2$, the electric field (red solid line) reduces within the air gap.* 21

2.12 ***Polariton excitation ladder.*** *With significant polariton-polariton interactions, the two-polariton state is blue-shifted to higher energies by an amount, U. If this shift is larger than the polariton linewidth, γ_{LP}, the two-polariton state can no longer be populated as photons resonant (or slightly red detuned) to the single-polariton state are of insufficient energy (red lines). However, there is an increased probability for two photon processes to excite the two photon state with blue detuned photons.* 25

2.13 ***Second order coherence function as a function of laser-polariton detuning.*** *The three traces are for different cavity-exciton detunings (blue = −5 meV, orange = 0 meV and green = 5 meV) across the polariton avoided crossing. These traces were produced using the parameters:* $\hbar\gamma_X = \hbar\gamma_C = 0.1$ *meV,* $\hbar\Omega_R = 2.5$ *meV, polariton interaction strength* $\hbar\omega_{nl} = 0.4$ *meV, pump field* $\hbar F = 0.1$ *meV and* $\Delta_{LP} = 0$. 27

2.14 ***Second order coherence function as a function of normalised nonlinear coefficient.*** *The three traces are for different cavity-exciton detunings (blue = −5 meV, orange = 0 meV and green = 5 meV) across the polariton avoided crossing. These traces were produced using the parameters:* $\hbar\gamma_X = \hbar\gamma_C = 0.1$ *meV,* $\hbar\Omega_R = 2.5$ *meV,* $\hbar F = 0.1$ *meV and* $\Delta_{LP} = 0$. 27

2.15 ***Second order coherence function at zero time delay*** $g^{(2)}(0)$ ***as a function of pump power.*** *The blue line shows the intra-cavity photon number and the red line shows the value of* $g^{(2)}(0)$. *These traces were produced using the parameters:* $\hbar\gamma_X = \hbar\gamma_C = 0.1$ *meV,* $\hbar\Omega_R = 2.5$ *meV,* $\hbar\omega_{nl} = 1.0$ *meV, and* $\Delta_{LP} = 0$. 28

2.16 ***Two-time photon correlation map for pulsed excitation.*** *(a) 35ps laser pulse profile for time scale reference. (b) Intra-cavity photon number over the duration of the laser pulse. (c) the two-time photon correlation,* $g^{(2)}_{phot}(t,t')$*, map for all combinations of t and t'. The black dotted line indicates* $g^{(2)}_{phot}(t,t')$. *Parameters:* $\hbar\gamma_x = 0.0621$*meV,* $\hbar\gamma_c = 0.0411$*meV,* $\hbar\omega_{nl} = 0.01$ *meV,* $\hbar\Omega_R = 1.4$ *meV,* $\Delta = 1.1$ *meV,* $\Delta_{LP}/\gamma = -0.875$ *and average incident power* $P = 15$ *pW.* 29

2.17 ***Second order autocorrelation at zero time delay*** $g^{(2)}(0)$ ***as a function of laser-polariton detuning for pulsed excitation.*** *The solid curves show the pulsed regime simulations while the dashed curves show the corresponding CW (steady state) regime simulations using the same experimental parameters for comparison for different cavity-exciton detunings* Δ *(blue = −0.5 meV, orange = 0 meV, green = 0.4 meV and red = 1.1 meV) moving across* $\Delta = 0$. *Parameters:* $\hbar\gamma_x = 0.062$ *meV,* $\hbar\gamma_c = 0.041$ *meV,* $\hbar\omega_{nl} = 0.01$ *meV,* $\hbar\Omega_R = 1.4$ *meV, pulse duration = 35 ps and average incident power* $P = 40$ *pW.* 31

2.18 ***Second order autocorrelation at zero time delay*** $g^{(2)}(0)$ ***as a function of normalised nonlinear coefficient for pulsed excitation.*** *The solid curves show the pulsed regime simulations while the dashed curves show the corresponding CW (steady state) regime simulations using the same experimental parameters for comparison for different cavity-exciton detunings* Δ *(blue = −0.5 meV, orange = 0 meV, green = 0.4 meV and red = 1.1 meV) moving across* $\Delta = 0$. *Parameters:* $\hbar\gamma_x = 0.062$ *meV,* $\hbar\gamma_c = 0.041$ *meV,* $\hbar\Omega_R = 1.4$ *meV,* $\Delta_{LP}/\gamma = -0.875$*, pulse duration = 35 ps and average incident power* $P = 40$ *pW.* 32

2.19 ***Second order autocorrelation at zero time delay*** $g^{(2)}(0)$ ***as a function of normalised average incident pump power for pulsed excitation.*** *Parameters:* $\hbar\gamma_x = 0.062$ *meV,* $\hbar\gamma_c = 0.041$ *meV,* $\hbar\Omega_R = 1.4$ *meV,* $\hbar\omega_{nl} = 0.01$ *meV,* $\Delta = 1.1$ *meV,* $\Delta_{LP}/\gamma = -0.875$ *and pulse duration = 35 ps.* 32

3.1 ***Fibre-based microcavity system schematic.*** *The SM fibre with mirror (yellow cylinder with mirror on end facet) is brought close to the planar sample to form a microscale optical cavity. The inset image is a cross section of the cavity where the blue layers form the fibre DBR mirror and conforms to the machined concave indentation on the fibre facet. The red layer between the two grey layers is the QW sample which is followed by the alternating grey/orange layers which constitute the other mirror which is grown directly onto the sample. The white curved line is the electric field of the cavity mode. From [8].* 36

3.2 ***Microcavity experimental setup.*** *(1) MIRA 900D laser operating in picosecond pulse mode with pulse width duration of 5-6ps at 76.3MHz repetition. (2) Acton SP2750 spectrometer for pulse modification. (3) Optronis SC-10 streak camera for measuring modified pulse widths. (4) High Finesse WS8-10 wavemeter for measuring pulse wavelength. (5) Fibre microcavity inside Liquid Helium dewar (inset) cross-section of fibre microcavity showing sample and fibre mirror structure. (6) Hanbury Brown and Twiss interferometer to measure emitted photon statistics of microcavity polaritons.* 37

3.3 ***Fibre microscope configuration.*** *The fibre mirror is glued vertically into a Titanium mounting block (trapezoidal piece) using a Silicon V-groove. This mounting block is situated upon a vertically moving Attocube nanopositioning piezo stage. The sample is glued onto a Titanium holder which can move in the XY plane via two horizontally moving Attocube nanopositioning piezo stages. The inset shows a magnified view of the fibre mirror as it approaches the sample. This mounting setup is placed at the end of an approx. 1.5 m long dipstick which is inserted into an airtight sleeve, establishing a vacuum inside the sleeve, and is then placed into a liquid Helium dewar. Light is collected at the top of the dipstick via a collimating lens (inside black square holder) situated just above the sample.* 38

3.4 ***FIMS experimental setup***. *This system comprises of two subsystems, the CO_2 laser ablation system and laser interferometry imaging system. The CO_2 laser ablation system starts in the top right corner with the water-cooled Synrad Firestar v30 CO_2 laser. Following the path of the beam left out of the laser is M0 which is a silicon coated mirror to guide the beam into the Brewster attenuators. The beam passes through BP1 and BP2 which are the Brewster attenuators which control beam power and polarisation. The beam exits BP2 into the beam expander BX which alters the size and position of the beam waist. The beam then reflects from M1 which is a silicon coated mirror onto M2 which is a $\lambda/4$ reflecting phase retarder for conversion of linearly polarised light into circularly polarised light. The CO_2 beam then passes through CO_2 OBJ which is the aberration free focusing double lens for beam focusing onto the fibre, with a working distance of 20.5mm. The laser interferometry imaging system starts in the lower right corner with a HeNe laser (632.8 nm) coupled into the system with the fibre coupler, FC, which incorporates a focal screw and polariser for maximum interference contrast. The beam then impinges on the large fused silica beamsplitter, BS, used to create the two arms of the interferometer. The split beams are reflected onto the silver mirrors M3 then M4. The beams travel towards the beamsplitter/mirror combination. The beams are collected by COBJ which is a Mitotuyo microscope objective with a 50x magnification. Finally, the camera is a DSLR Cannon CCD camera for image capture of the fibre facet.* 41

3.5 ***Movable Michaelson interferometer for fibre characterisation.*** *The beamsplitter along with a mirror is placed on a linear nanopositioning stage to allow the interferometer to be moved out of the CO_2 laser beam path for ablation. The stage can then be precisely returned to its original position infront of the fibre to image the fibre indentations for characterisation.* . . . 42

3.6 ***Interferometric fibre image with ROI selection box.*** *A thin rectangular ROI box is placed over the fringes produced by the indentation. Note the how the ROI box is parallel to the large fringes on the flat part of the fibre facet.* . . 43

3.7 ***Pixel intensity graph of the interference fringes.*** *The maxima and minima of the pixel intensity values correspond directly to the respective interference fringes. The red and green crosses indicate to the user where the programme has found the position of bright (red) and dark (green) fringes to be.* 43

3.8 ***Fitted indentation profile.*** *The extracted indentation profile (blue circles) is fitted with a Gaussian function (red curve). At the centre of the Gaussian, RoC variation is small and can be approximated to be spherical in this region, allowing an RoC value to be given to this structure.* 44

3.9 ***Cavity mode simulation.*** ***(a)*** *Schematic cross-section of microcavity with experimental parameters and sample.* ***(b)*** *Exploded view of the QW sample layer composition.* ***(c)*** *Simulation of the electric field of the cavity mode. The bright parts are places of large electric field intensity.* 45

3.10 ***Photoluminescence (PL) under non-resonant excitation at 798 nm.*** *The signature of the strong coupling regime, the classic avoided crossing with the two polariton mode branches. Vacuum Rabi splitting $2\hbar\Omega_R = 2.8$ meV. The red dotted lines show the manual fitting of the polariton modes with the respective exciton transition and photon/cavity mode. Δ is the detuning between the photon and exciton resonant frequencies such that $\Delta = \omega_C - \omega_X$.* 47

3.11 ***Photoluminescence (PL) under non-resonant excitation at 825 nm.*** *The black anti-crossing lines are the upper and lower polariton modes. The red and blue vertical dotted lines show the neutral exciton (X^0) and negative trion (X^{-1}) states. The top spectrum is a slice in this map, taken for a slightly negative detuning, shown by the red solid line. The X^{-1} state is found ~1.2 meV red detuned from the neutral exciton state.* 48

3.12 ***Photoluminescence through Excitation (PLE) of the LP mode.*** *The main graph shows individual spectra taken at increasing laser excitation wavelengths (front to back). The inset graph shows the same graph as a 2D intensity graph. The two 'windows' of emission at 1.557 eV and 1.506 eV are evident with a considerable difference in emitted intensity due to the GaAs absorption edge at 1.589 eV. Note the two peaks present are most likely due to birefringence in the GaAs.* 49

3.13 ***Resonant laser scans of the LP mode.*** *Each graph shows the LP lineshape as the detuning is swept across from negative to positive (top to bottom). Due to birefringence, the LP mode is polarisation split which is indicated by the double Lorentzian fit (dark blue and grey). The third broad Lorentzian fit (light blue) is added to demonstrate the contribution from the X^{-1} trion state. The red line shows the total fit of all these contributions to the the data (black dots). Since the LP intensity decreases for more positive detunings, some of the graphs have been magnified to show the relevant detail denoted by the x2 and x5.* 50

3.14 ***Trion contribution to LP lifetime.*** *Resonant lifetime traces of the LP mode at two different detunings. Trace ① shows a monoexponential decay for detunings far red detuned from the trion resonance. Trace ② shows a biexponential decay near the trion resonance, where a second fast decay is introduced by the loss mechanism mediated by the trion state.* 51

3.15 ***Resonant LP lifetimes as a function of detuning.*** *The lifetimes are fitted to the neutral exciton X^0 (black dotted line) and trion X^{-1} (red solid line) decay rates, indicating a large contribution from the trion state. Inset: Spectra of the LP mode showing the presence of the X^{-1} state red detuned from the neutral exciton.* 52

3.16 ***Effect of excitation pulse width on*** $g^{(2)}(0)$. *Simulations of* $g^{(2)}(0)$ *as a function of Δ_{LP} for different pulse widths. Simulation parameters: Δ =1.1 meV, τ_{LP} =7.8 ps, ω_{nl} =0.01 meV.* 54

3.17 ***Pulse modification setup.*** *A variable diameter iris alters the effective NA of incoming pulsed laser beam (1) which enters a grating spectrometer (2), spatially expanding the frequency components of the pulse. The output from the spectrometer is coupled into a fibre (4) which acts as pinhole for spectral filtering. The modified pulse is measured for both pulse duration and centre wavelength using a streak camera (5) and a wavemeter (6).* 54

3.18 ***Pulse width characterisation.*** *Temporal profiles of the modified laser pulses. There is some slight distortion of the pulse profile in the 30-40ps range, however this can be corrected in real time by using the continuous run function on the streak camera and fine tuning the fibre coupling.* 55

3.19 ***Optical cross-talk calibration of the ZDT experimental setup.*** *Free-space optics* **(a)** *and fiber-based* **(b)** *HBT interferometers. A retro-reflecting extra mirror is placed in the free 'vacuum' port in both of the interferometric setups. The mirrors reflect any secondary emission from the APDs (blue arrows) back into the detection arms. The extra pellicle beamsplitter and CCD camera (near green arrow) in the right hand detection arm of* **(a)** *is used for alignment purposes only.* 57

3.20 ***Free optics HBT photon correlations with optical cross-talk.*** *Raw photon correlation data in the free optics HBT configuration in both pulsed* **(a)** *and CW* **(b)** *laser operation. The upper traces of both* **(a)** *and* **(b)** *correspond to having the extra 'vacuum' port mirror while the bottom traces do not. In the upper traces of both* **(a)** *and* **(b)** *two sets of additional cross-talk peaks appear at ~3 ns (A, A') and ~6 ns (B, B') delay (positive and negative) from the main peak. They correspond to the time of flight of approximately 1 m between the two detectors. These peaks vanish in the bottom plots of* **(a)** *and* **(b)** *when the extra mirror is removed.* 58

3.21 ***Fibre based HBT photon correlations with optical cross-talk.*** *Raw photon-autocorrelation data in the fibre-based HBT configuration for both pulsed* **(a)** *and CW* **(b)** *laser operation. The upper traces of* **(a)** *and* **(b)** *were taken with the extra 'vacuum' port mirror present while for the lower traces the mirror was removed. The upper traces of* **(a)** *and* **(b)** *show peaks A, A' ~30 ns away from the main peak. This corresponds to the in-fiber time-of-flight between the two detectors and an effective fiber length of approximately 2 x 3 m (entire optical path of the reflected light). These peaks vanish in the lower traces of panels* **(a)** *and* **(b)** *with the extra mirror removed.* 60

4.1 ***Antibunched raw coincidence data and integrated coincidences histogram.*** *Upper panel: Extended coincidence counts histogram for the raw data. The mean peak value is indicated by a dotted black line. Lower panel: Integrated coincidences histogram (blue bars) extracted from the raw data by following the analysis protocol described in section 4.1.3. The mean integrated value is indicated by the dotted green line.* 62

4.2 ***Quantum correlated photons with cavity-exciton detuning**. **(a)-(c)** Photon autocorrelation data $g^{(2)}(0)$ for three different cavity-exciton detunings $\Delta =$ 0.14 **(a)**, 0.83 **(b)** and 1.11 meV **(c)**. At each Δ, we measure $g^{(2)}(0)$ for five different laser detunings, Δ_{LP}. Each subfigure contains three subpanels, with the top panel showing the corresponding resonant laser scan. The bottom panel displays the corresponding correlation data (black dots) along with the calculation from the single-mode theory (two lines corresponding to upper and lower bounds of the interaction strength). The middle panel contains a plot of the transmission fraction $\tilde{T}$. This parameter gives an indication of the perturbation of the mode of interest, π_x through the presence of the orthogonally polarized polariton mode π_y and the trion resonance. Both are expected to lead to a significant deviation of the measured $g^{(2)}(0)$ from the single-mode theory. Hence, only regions with large $\tilde{T}$ are expected to give correlation data that are close to the expected theory values. In subfigure **(c)** only the data point **(i)** around zero detuning Δ_{LP} shows negligible influence from π_y and the trion resonance. It exhibits antibunching around $g^{(2)}(0) =$ 0.93 ± 0.04, with the corresponding raw data displayed in subfigure **(d)**. The dip at zero time delay is clearly visible both in the raw correlation trace and the integrated coincidences plot.* 63

4.3 ***Polariton-Polariton interaction constant**. **(a)** Correlation data near cavity-exciton resonance. The top panel contains the corresponding resonant transmission laser scan while the middle panel shows the calculated transmission fraction $\tilde{T}$. The bottom panel displays $g^{(2)}(0)$ as a function of laser detuning Δ_{LP} from the position of the LP π_x-resonance for a cavity-exciton detuning of $\Delta = 0.07$ meV. Except for the two rightmost points which are heavily influenced by the π_y mode, all other data points are from almost pure π_x-mode photons. **(b)** Example raw correlation traces from the two points **(ii)** and **(iii)** in subfigure **(a)**. **(c)** Coefficient of determination R^2 of the data fit with the theoretical model versus interaction parameter $\hbar g$. The most likely value is $\hbar g_0 = 0.020 \pm 0.011$ meV·µm^2.* 64

4.4 ***Optical characterisation and photon correlation measurement in a second fiber cavity.** **(a)** Low-temperature photoluminescence (PL) map as a function of cavity detuning (Δ). **(b)** Experimental LP linewidth (γ_{Exp}) (blue filled circles) and the calculated LP radiative linewidth (γ_{Rad}) (black filled squares) as a function of Δ. **(c)** Evolution of the figure of merit ρ_0 as a function of Δ. In both **(b)** and **(c)** figures $\Delta = -0.45$ meV (redish shadow) shows the best signal-to-noise ratio for the photon correlation measurements. **(d)** Measured resonant transmission spectra of the the π_X LP transition (black dots), and Lorentzian fitting to both linear LP transitions (bluish shadows). The red continuous line represents the cumulative fit. **(e)** Photon correlation measurements as a function of laser detuning (Δ_{LP}) for $\Delta = -0.45$ meV and two excitation powers: 700 pW (open circles) and 200 pW (filled circles).* . . 66

4.5 ***Typical zero-delay raw coincidences peak.** The FWHM of the zero-delay peak is 0.6 ns, with a maximum of 95 coincidence counts. Dark coincidence counts from the detectors are delay independent, and amount here to 0.5 counts on average (Inset).* 68

4.6 ***Extracted second order autocorrelation function at zero time delay.** $g^{(2)}(0)$ values extracted following the analysis protocol described.* 69

4.7 ***Sensitivity of the result on the analysis parameters.*** *Values obtained for* $g^{(2)}(0)$ *(at* Δ_{LP}*) = -0.010 meV and +0.037 meV in Fig 4.6), from analysis of the raw data, using W = {0.512,0.832,1.216,1.600} ns, and* n_p *= {300, 100,30,10} peaks.* 69

4.8 ***Raw photon correlation histograms.*** *(i) Raw photon correlation histogram from main text Figure 4.b with laser detuning* Δ_{LP} *= -0.010 meV until 11 consecutive correlated pulses. (ii) Raw photon correlation histogram from main text Figure 4.b with laser detuning* Δ_{LP} *= +0.037 meV until 11 consecutive correlated pulses. Arrows indicate the position of the zero delay peak.* . . . 70

5.1 ***Biexciton cascade with two-colour correlations. (a)*** *The biexciton cascade with two-colour correlations where* $\Delta_{LP} = \omega_{LP} - \omega_{filter}$*. Note in this graph frequency is used, but in reality, this is actually* $g^{(2)}(\tau)$ *as a function of delay time. With the spectrometer providing the spatial filtering of the photoluminescence, bunching will occur on the red side of the neutral exciton transition, and antibunching on the blue side for the two-colour correlation shown in the graph on the RHS of* ***(a)***. ***(b)*** *Polariton cascade with a monochromatic filter with centre frequency* ω_{filter}*. Due to the cascade nature of the process, photon antibunching is expected on the red-detuned of the neutral exciton, and photon bunching on the blue-detuned side.* 72

5.2 ***Non-resonant*** $g^{(2)}(0)$ ***measurements as a function of filter-polariton detuning.*** *Measurements were taken at a cavity-exciton detuning of* δ *= 0.94 meV and show clear signs of antibunching when the filter is red detuned from the centre of the polariton transition. Photon bunching is also present when the filter is blue detuned, following similar behaviour to the resonant measurements.* 73

5.3 ***Spectrally filtered photoluminescence.*** *From left to right: the pump laser excites an incoherent long-lived excitonic population dubbed the 'excitonic reservoir'. This reservoir induces upward transitions in the polaritonic anharmonic excitation ladder. Downward transitions correspond to the emission of a photon in the detection channel. The emitted photons are frequency selected by a narrow band filter of transmission spectrum* $T(\omega - \omega_F)$ *prior to photodetection. L(t) is the pulsed laser excitation,* $<n_r>$ *is the expectation value of the reservoir population,* γ_r *is the reservoir linewidth,* γ *is the polariton emission rate and g is the polariton-polariton interaction constant.* 75

5.4 ***Quantum events for microcavity polaritons under non-resonant excitation.*** *There are four possible events for the system to evolve in a time interval* $t + dt$*.* $\hat{K}^{det}$ *involves a photon emission from the system which passes through the filter and is detected.* $\hat{K}^{no\ det}$ *involves an emission event, but the photon either is rejected by the filter or is not detected due to the quantum efficiency of the detector.* $\hat{K}^{pump}$ *involves the injection of a polariton into the system. Finally,* $\hat{K}^{no\ jump}$ *describes a no emission event. All these possibilities describe the system dynamics when placed in the Master equation.* 76

5.5 $g^{(2)}(0)$ ***under non-resonant excitation as a function of filter frequency-LP detuning.*** $g^{(2)}(0)$ *becomes antibunched on the red detuned side of the transition and bunched on the blue detuned side. This behaviour resembles what has been observed previously with the system under resonant excitation. Parameters:* $\omega_{nl} = 12\ \mu eV$*, input power = 12 pW, pulsewidth = 40 ps.* . . . 77

1

Introduction

Quantum fluids of light is an actively emerging field of study which explores the concept that, in certain situations, light could be considered a fluid composed of many particulate photons that exhibit substantial photon-photon interactions. The very notion of a photonic fluid is at odds with our usual understanding of light. While this rules out photon fluids in vacuum, nonlinear optical materials exhibit sizeable photon-photon interactions [9] by mediating them through interactions between matter excitations. A holy grail both in quantum optics and in the field of light-based quantum fluids is to engineer these driven-dissipative systems such that strong quantum correlations between individual photons build up. Sizeable photon-photon interactions would result in a strongly nonlinear photonic system where a single photon can change the response of the system, similarly to what has been seen with cold atomic gases [10, 11]. An array of such strongly nonlinear photonic system arranged in a lattice geometry constitutes a platform for studying quantum many-body systems of light [12] as shown in Fig 1.1. This is decidedly interesting since the photonic platform is inherently driven and dissipative. In particular, the photonic platform could be used to study the rich physics of the driven-dissipative Bose-Hubbard model [13], quantum phase transitions of light [1], superfluid to Mott transitions [14], **XY** spin Hamiltonian physics [15] and for realizing a so-called Tonks-Girardeau gas of impenetrable photons [16, 17]. Ultimately, the driven-dissipative nature of the photon fluid would provide a non-equilibrium platform in which individual particle systems can be controlled and measured. This capability could be used to simulate realistic many-body systems that involve driven and dissipation mechanisms which would be the ideal platform for a photonic quantum simulator [18].

While the potential for the study of quantum fluids of light is highly interesting and appealing, the challenge now faced is finding and developing nonlinear optical material systems that exhibit sizeable single-photon nonlinearities.

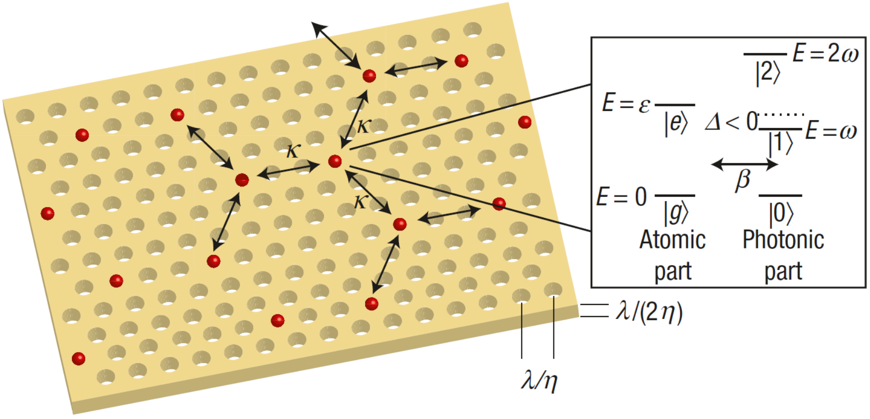

Figure 1.1: ***Quantum many-body system of light.*** *A 2D lattice of photonic crystal cavities, each containing a a nonlinear quantum material, leading to strong, on-site, photon-photon interactions. The interplay between on-site interactions, U, and the photon hopping, κ determines the system dynamics. Such a platform was proposed as a quantum simulator for drive-disspative many-body quantum system. From [1].*

Single emitter nonlinear systems

In the search for nonlinear optical material systems with potential of realizing strong single-photon nonlinearities, it has been recognised that cavity-quantum electrodynamics (cavity-QED) systems in the so-called *strong coupling regime* of light and matter hold particular promise. In systems that are in the strong coupling regime, the new *dressed* eigenstates of the system that emerge are a result of the linear coherent coupling between one or more matter excitations and an optical field which surpasses the dissipative processes in the system. The new eigenstates are a superposition of the matter excitations and photon states and are distinctly separated in energy by the *Vacuum Rabi Splitting* and can be treated as half light-half matter quasiparticles known as *polaritons*. One system in the strong-coupling regime that has attracted considerable attention and research is Quantum Dots (QD) coupled to photons inside microcavities. QDs are artificially constructed, semiconductor nanostructures which behave as a two-level quantum emitter, much like an atom. In strongly coupled single QD cavity systems, the resulting Jaynes-Cummings energy ladder of cavity-QED is distinctly *anharmonic* in structure [19]. The nonlinear structure occurs due the imprinting of the quantum nature of the QD emitter on the Jaynes-Cummings energy ladder. The inherent nonlinearity present in the coupled system allows for sizeable photon-photon interactions to occur at the single photon level, resulting in the so-called *photon blockade* effect [20]. The photon blockade effect, termed in analogy to the electron blockade effect in condensed matter physics, occurs when the presence of a single photon produces system nonlinearities large enough to shift the system transition frequency by an amount larger than the transition linewidth. This means that a first photon resonant with the fundamental system transition will block the entrance of a second photon of the same colour into the system due to the mismatch in energy with the now shifted system transition. The first ever observation of the photon blockade effect was demonstrated with single atoms coupled to a Fabry-Pérot cavity [21] in 2005 with the observation of photon antibunching. This was followed by the first clear demonstration with QDs coupled to photonic crystal (PC) defect cavities in 2012 [22]. Follow-up works using QDs strongly coupled to microcavities have shown ultra-fast optical switching [23–26] and polariton transistor behaviour, [27] as well as quantum information processing techniques using controlled phase gates[28].

As a side note, it is important to mention that photon blockade has also been demonstrated in the microwave domain using superconducting qubits in stripline resonators [29]. Also, at the time of writing this thesis, the microwave community has demonstrated the use microwave superconducting circuits to dissipatively stabilise a Mott insulator of photons [30].

Considering the presence of single-photon nonlinearities in QD-cavity systems and the well established fabrication techniques used to manufacture QDs in solid-state structures, QDs could be an ideal system for integration into larger lattice geometries to create a strongly interacting quantum fluid of light platform. However, a major drawback of such a device based on self-assembled QDs is the distribution of resonant frequencies and nucleation positions of individual QDs due to the random nature of the QD growth process. These large variations limit the easy scalability of QD-cavity systems to coupled lattice systems to create a strongly interacting quantum fluid of light. While work is continuing on improving the ordering, positioning and uniformity of QD arrays [31], it is clear that two-dimensional lattices of coupled quantum cavities based on self-assembled QDs are currently not feasible.

Microcavity Polaritons

Alongside the development of coupled QD-cavity nonlinear systems, quantum well (QW) exciton polaritons or microcavity polaritons are being studied as a compelling strongly coupled cavity-QED contender. These systems are the result of the hybridisation of multiple quantum well (QW) *excitons* which are bound electron-hole pairs, with a single mode of a planar optical microcavity [32]. However, unlike QD-cavity systems where photon-photon interactions occur due to the inherent nonlinear nature of a single quantum emitter, photon-photon interactions in microcavity polaritons occur through polariton-polariton scattering mediated by repulsive, contact exchange, exciton-exciton interactions. The exciton mediated polariton interactions and the small effective mass of microcavity polaritons on the order of 10^{-5} m_e provoked considerable interest in the possibility of Bose-Einstein condensation (BEC) of microcavity polaritons.

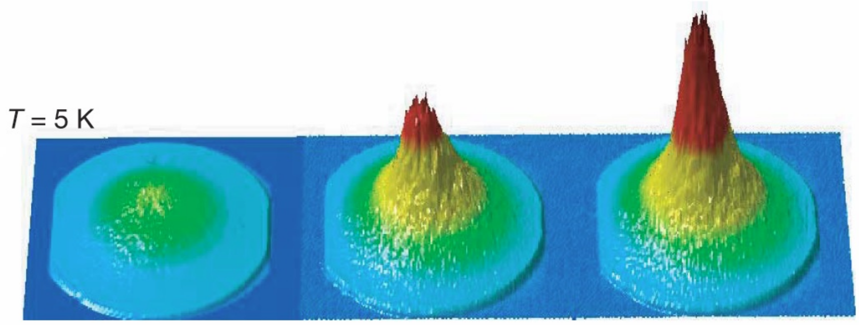

Figure 1.2: ***Bose-Einstein condensation of microcavity polaritons.*** *Images of the far-field emission distribution of microcavity polaritons as they condense into the lowest momentum state,* $\boldsymbol{k}_{||} = 0$*, as excitation power is increased (left to right). From [2].*

With the prediction of a microcavity polariton BEC in 1996 [33], it was not until 2006 that the BEC of microcavity polaritons was conclusively demonstrated [2], showing the accumulation of polaritons into the fundamental energy state in real and momentum space resulting from the emergence of long-range coherence shown in Fig 1.2. Here the incoherently injected polariton gas relaxes towards the LP via acoustic-phonon, optical-phonon and polariton-polariton interaction assisted decay. At the critical density controlled by excitation power, the polaritons attain a quasi-thermal equilibrium state where the polariton lifetime is sufficiently long compared to the thermalisation time. However, since this is a driven-dissipative system, the system is intrinsically non-equilibrium in nature, raising interesting questions about non-equilibrium quantum fluid physics [34–36].

With the demonstration of microcavity polariton condensates, it was proposed that polariton condensates should exhibit superfluid behavior when encountering an obstacle or defect [37] using generalised Gross-Pitaevskii equations to describe the resonant driving and relaxation processes. Experimental validation of these predictions was observed in 2009 with the demonstration of superfluid flow of microcavity polaritons [3]. In this work, superfluid flow was shown by the suppression of real-space disturbances and elimination of the Rayleigh scattering ring in momentum space of a propagating polariton fluid around a localised defect, shown in Fig 1.3.

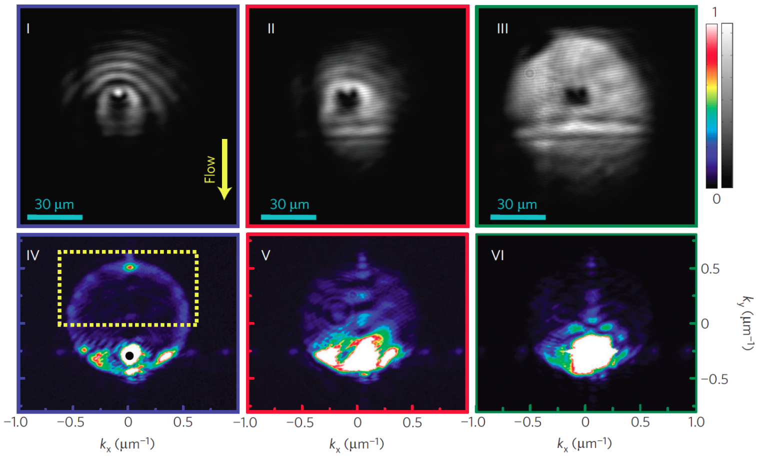

Figure 1.3: ***Superfluid flow of microcavity polaritons.*** *Experimental images in real space (I-III) and momentum space (IV-VI) of a polariton fluid flow hitting a localised defect. From left to right, the columns show increasing polariton density. In panel III, superfluid flow is established with the suppression of scattering around the defect and the disappearance of the Rayleigh scattering ring in panel VI. From [3].*

In later experiments, hydrodynamic effects associated with polariton superfluid flow were observed with the formation of vortex-antivortex pairs [38, 39] and half integer vortices, [40] as well as dark solitons [41]. However, these quantum fluid effects are the result of the collective interactions of a large number of coherent polaritons as the interaction between individual particles is weak. To shift microcavity polaritons into the strongly interacting photon regime, polariton-polariton interactions must be enhanced such that large system nonlinearities at the single particle level emerge.

Strongly interacting polaritons

The regime of strongly interacting microcavity polaritons resulting in single-photon nonlinearities was first proposed in 2006 [42] with the so-called *polariton blockade effect*, so termed in analogy to the photon blockade effect. In the polariton blockade regime, strong polariton-polariton interactions would induce noticeable system nonlinearities such that injection of a single polariton into the system would inhibit the injection of subsequent polariton of the same energy. A microcavity polariton system in the polariton blockade regime would exhibit sizeable quantum correlations in the form of photon antibunching, similarly to what has been observed with the photon blockade phenomenon. To achieve the strong polariton interactions required to induce large system nonlinearities, several ideas were put forward in the last decade. A recent idea is to use dipolar polaritons in coupled QW structures in one-dimensional waveguides [43, 44]. In this system, large interactions arise from the long-range dipole-dipole interactions of indirect excitons rather than exciton contact exchange interactions. An earlier idea suggested the use of the polariton Feshbach resonance [45] which seeks to exploit the biexciton Feshbach resonance effect. This requires the tuning of the cavity energy to bring the two-polariton state in resonance with the biexciton state, dramatically enhancing the system scattering cross-section similar to what has been observed with cold atoms [46]. One idea that has drawn extensive activity and interest is the concept of a *photonic dot* [42], inspired by the QD nano-structure. The idea of the photonic dot centres on the creation of very small lateral sizes of the cavity mode. This imposes confinement on the polariton wavefunction through the photonic component of the polariton rather than the matter component which is the case with QDs. If this photonic confinement is small enough, strong polariton-polariton interactions mediated by the excitonic component will occur due to the shrinking of the effective interparticle distance.

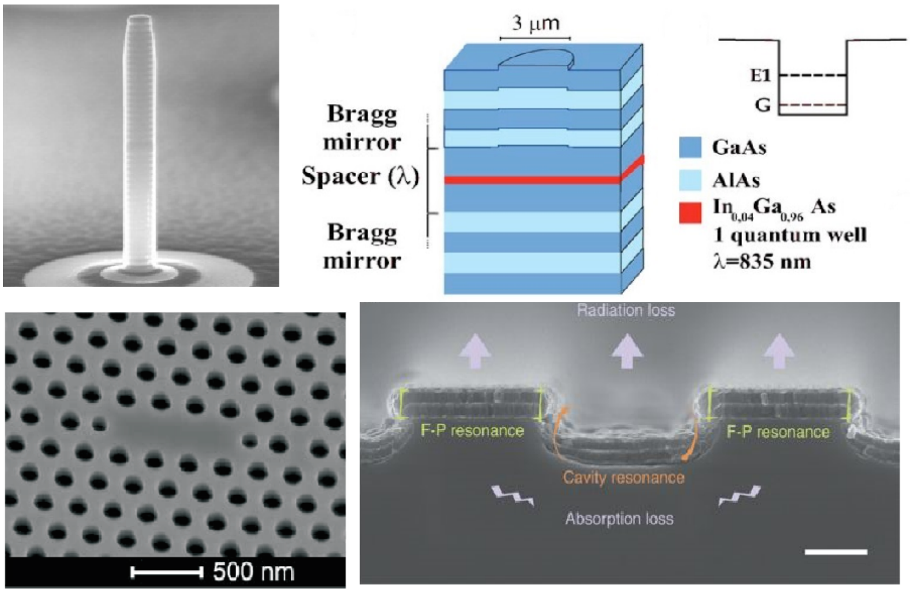

Figure 1.4: ***Microcavity architectures for photonic confinement of microcavity polaritons.*** *Top left: Micropillar cavity constructed using photolithography to etch pillars out of planar QW microcavities. Photons are confined due to the physical shape of the micropillar. From [4]. Top right: Mesa structure etched into the spacer layer of a planar microcavity. The local difference in the spacer layer creates a potential trap for confined photons. From [5]. Bottom left: Photonic crystal cavity structure. A photonic band-gap is created by etching holes in the sample substrate and a cavity is created by the absence of a hole in the structure or defect site. From [6]. Bottom right: Plasmonic microcavity structure cross-section using multilayer trench gratings. From [7].*

The resulting non-trivial quantum correlations could be then further enhanced by coupling the nonlinear system to another microcavity, creating Mach-Zender interferometer, leading to a quantum interference phenomenon, the so-called *unconventional polariton blockade effect* [47]. If strongly interacting polaritons could be achieved in a photonic dot microcavity system, the high uniformity of the QW structure could be used to place several identical photonic dot cavity systems on the same sample, coupled by hopping photons, providing an ideal platform for creating a scalable platform for studying strongly interacting quantum fluids of light.

The stipulation of photonic confinement on the polariton wavefunction necessitates the careful engineering of the cavity mode to have a mode waist size approaching the μ-scale. For this purpose, several integrated microcavity architectures have been developed to study confined polaritons such as mesa structures [5]; which are etched into the spacer layer of a planar microcavity where the local difference in the spacer layer creates a potential trap for confined photons, micropillars; [4] constructed using photolithography to etch pillars out of planar QW microcavities where the photons are confined due to the physical shape of the micropillar, photonic-crystal cavities [48]; where a photonic band-gap is created by etching holes in the sample substrate and a cavity is created by the absence of a hole in the structure or defect site, and finally, plasmonic structures [49]; which use multilayer trench gratings. These integrated microcavity architectures are shown in Fig 1.4. However, the polariton blockade phenomenon has not yet been observed in these systems as they typically suffer increased losses and reduced coupling as the lateral dimensions of the cavity approach the μ-scale.

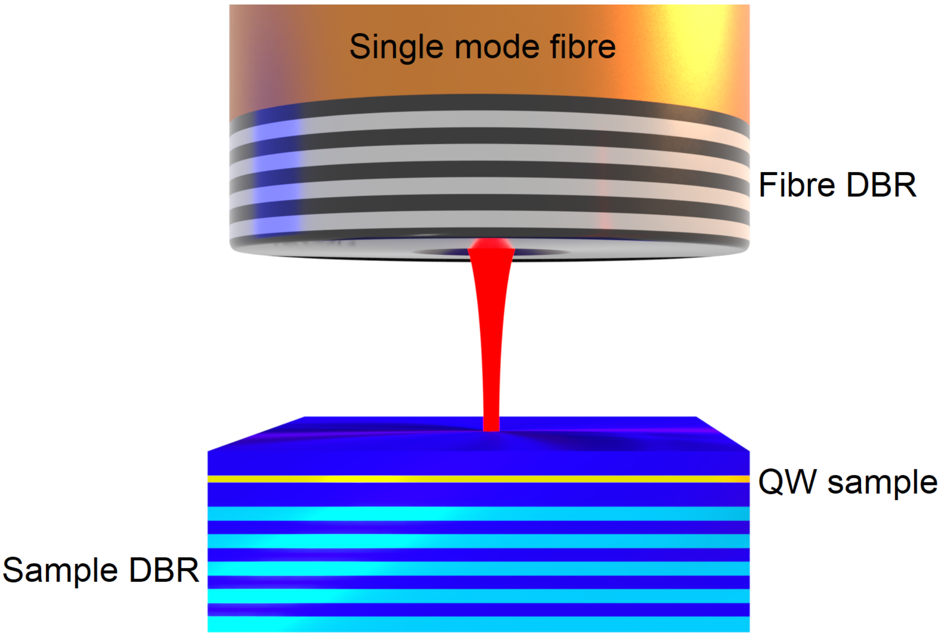

Figure 1.5: ***Fibre Fabry-Pérot microcavity.*** *A single mode fibre tip is machined with a small concave indentation to reduce the mode waist to increase optical confinement of the microcavity polaritons. The air gap between the QW sample and fibre allows for in-situ tuning of the cavity energy over a greater range afforded by other designs.*

A more recent microcavity architecture that has become available is a flexible, semi-integrated Fabry Pérot fibre microcavity platform [50, 51] that allows *in situ* tuning of the cavity length and hence the polariton energy and lifetime, as shown in Fig 1.5. Already, these microcavity platforms have been shown to exhibit equal if not better quality factors than their integrated counterparts in confined microcavity polariton systems [8]. The added benefits of open-accessibility and fabrication control over the fibre mirror geometries presents an ideal experimental platform for studying microcavity polaritons. In this thesis, we use a fibre-based microcavity polariton system to allow the study of polariton interactions of optically confined polaritons. In doing so, we observe for the first time, in parallel with a group at ETH Zürich [52] - the emergence of quantum correlations from strongly interacting microcavity polaritons, which is the main result of this thesis.

Scope of this thesis

This thesis is structured in the following way:

In **Chapter 2**, the theoretical background of QW excitons strongly coupled to the mode of an optical microcavity is presented, with the inclusion of discussions on exciton-exciton interactions. Important information about Fabry-Pérot microcavities is given with discussion on cavity engineering to introduce optical confinement of microcavity polaritons. Finally, the concept of polariton-polariton interactions and their role in the polariton blockade effect is discussed. A model of the system dynamics is presented from which simulation results of expected photon correlations in both CW and pulsed pumping regimes are derived using experimental parameters.

Chapter 3 presents the QW microcavity setup based on a fibre microcavity An overview of the fibre mirror fabrication and characterisation process is given. Photoluminescence (PL) measurements of microcavity polaritons are given showing the presence of the negative trion state. This is followed by resonant measurements of the lower polariton (LP) branch which include lifetime and lineshape measurements of the LP mode with a discussion on the impact of the trion state on the system dynamics. Finally, a calibration technique for determining the zero delay time (ZDT) of the Hanbury-Brown and Twiss (HBT) inteferometer is presented and its importance to photon correlation measurements is discussed.

Our main findings of emerging quantum correlations from optically confined, interacting microcavity polaritons under resonant excitation are presented in **Chapter 4**. Photon correlation measurements taken scanning the resonant excitation laser across the LP transition are quantitatively analysed with respect to the system dynamics model presented in Chapter 2. Also included is a detailed explanation of the second-order correlation function analysis protocol used, with emphasis on the sensitivity of the results on the analysis parameters.

Chapter 5 presents preliminary results on the observation of quantum correlations from microcavity polaritons under non-resonant excitation. A work-in-progress model for the observed correlations is discussed and the possible implications of the existence of a large, incoherent exciton reservoir are presented.

Finally, **Chapter 6** concludes this thesis with an outlook for future work.

2

Semicondutor Quantum Well Polaritons

In this chapter, the theoretical frame work of microcavity polaritons and the interactions that can occur between them is presented. In Section 2.1, the exciton quasi-particle is introduced along with a discussion on interactions between particles. With the concept of excitons and interparticle interactions established, Section 2.2 describes the underlying physics of microcavity polaritons as well as an introduction into Fabry-Pérot microcavities and designs used for studying microcavity polaritons, specifically with regards to optically confined systems. Section 2.3 gives a definition of the different photon statistics that can be used to characterise microcavity polariton systems. Finally, Section 2.4 discusses polariton-polariton interactions in reference to the polariton blockade regime. Also in this section, theoretical simulations of an interacting polariton system are given.

2.1 Excitons

In our most basic understanding of semiconductor materials, the highest valence electron band is completely occupied while the lowest conduction electron band is vacant. These bands are separated in energy, the so-called 'band-gap' energy, E_g, which is the energy required for an electron transition into the conduction band. Once an electron is excited to the conduction band, it effectively leaves behind a positive 'hole' in the valence band. While transitions between the valence and conduction band can not occur for free electrons with energies less than E_g, electron-hole pairs can form bound (Rydberg) states due to Coulomb attraction called *excitons*, which lie just below the energy band-gap. These quasi-particles have wave-functions analogous to hydrogen atoms. However, the exciton Bohr radius a_X is larger than its atomic counter-parts and can extend over several lattice sites due to their low effective mass and large dielectric constant ($\epsilon = 12.9$ for GaAs) of the semiconductor material. The energy levels of these excitons can be given by a modified Rydberg equation [53]:

$$E_n = E_g - \frac{e^2}{8\pi\epsilon a_x n^2} + \frac{\hbar^2 k^2}{2\,(m_e + m_h)} \qquad (2.1)$$

where n is the principle quantum number, m_e and m_h are the electron and hole effective masses, e is the electron charge, ϵ is the appropriate dielectric constant and a_x is the exciton Bohr radius:

$$a_x = \frac{4\pi\hbar^2\epsilon}{e^2\mu} \tag{2.2}$$

$$\mu = \frac{m_e m_h}{m_e + m_h}. \tag{2.3}$$

Excitons decay by radiative recombination, whereby the electron relaxes back into the corresponding hole in the valence band. As a result of this process, a photon is emitted equal to the binding energy plus the band-gap energy of the exciton. Excitons are classified into two categories; Frankel excitons and Wannier excitons. Frenkel excitons are characterised by tightly bound excitons with a very small Bohr radius, typically confined to one lattice site.

Wannier excitons on the other hand are weakly bound excitons with a large Bohr radius that can extend over several lattice sites (see Fig 2.1) and are found typically in inorganic semiconductor crystals. Unlike Frenkel excitons, Wannier excitons are relatively free to move around the lattice with typical diffusion lengths of up to several micrometers.

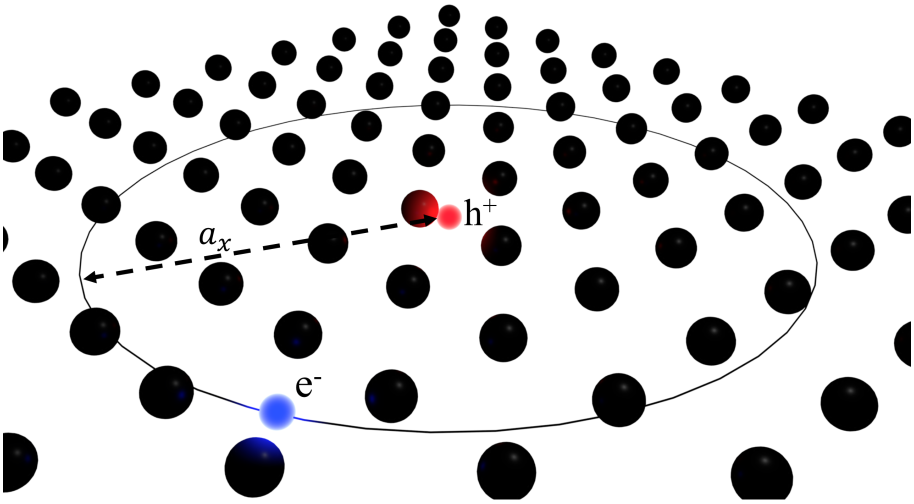

Figure 2.1: ***Wannier Exciton inside a semiconductor crystal lattice.*** *A bound electron-hole pair (red electron, blue hole) with a large Bohr radius extending over several lattice sites (black dots). The non-localised nature of these excitons allows propagation through the lattice.*

The energy structure for these excitons can be understood by studying the band energy structure of bulk semiconductor material. For convenience and relevance, GaAs will be focused upon. At the band-gap edge, the electrons in the conduction band at the lowest energy has an s-like structure and is two-fold degenerate due to 1/2 spin. The holes at the highest point in the valence band have a p-like structure which holds a six-fold degeneracy at the high symmetry Γ-point. Due to spin-orbit coupling, a pair of states are separated from the others, the so-called spin-orbit or split-off (SO) band, which is shifted to lower energy. The remaining 4 states are a pair of two-fold spin degenerate states. However, this degeneracy is lifted for large k values as shown in Fig 2.2. The different curvatures of these two bands arise from the nearly order of magnitude difference in effective masses of those bands. These two bands are therefore aptly named the heavy hole (HH) and light hole (LH) valance bands.

Therefore, there are four transitions available for the creation of excitons due to the spin degeneracy of the charge carriers. For the case of optical transitions, the difference in total angular momentum between initial and final states must conserve the total angular momentum of a photon. Consequently, only two of the states can recombine optically, emitting either left or right circularly polarised photons and are called *bright excitons*.

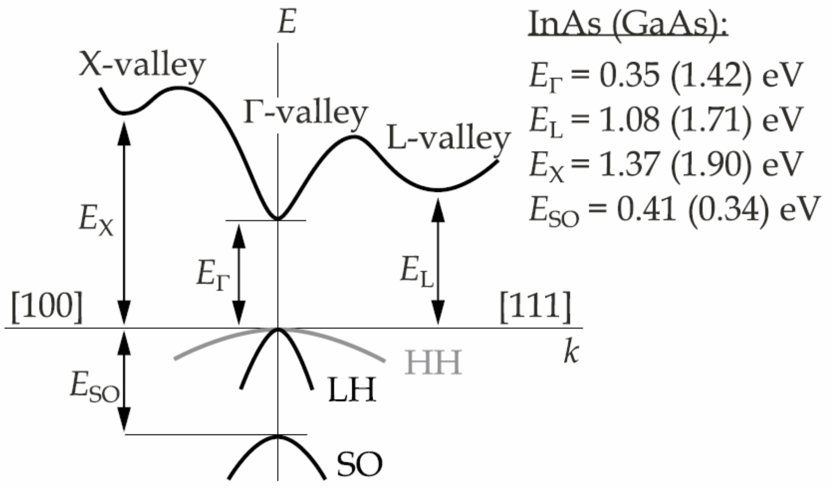

Figure 2.2: ***Band structure of GaAs.*** *The six-fold degeneracy of the valance band electrons divides the electron states into 3 pairs of states, heavy hole (HH), light hole (LH) and split off (SO). The difference in effective masses of the HH and LH electrons lifts the degeneracy of the HH and LH electron bands for* $k > 0$. E_Γ *is the band-gap energy.*

2.1.1 Quantum Well Excitons

Quantum wells (QW) are two dimensional planar nanostructures, designed to alter the electronic properties of semiconductors. A QW consists of a layer of a low-energy band-gap semiconductor material such as InGaAs, sandwiched between high-energy band-gap materials such as GaAs. Typically grown using the molecular beam epitaxy (MBE) technique which allows layers of material to be deposited one atomic layer at a time, the thickness of the low-energy band-gap material is designed and grown to be close to the exciton Bohr radius $a_X \sim 10$ nm, creating an effective potential well in the growth direction. This means that electrons and holes as well as excitons created in the low-energy band-gap material will be confined in the growth direction, however, their in-plane momentum is unaffected.

The confinement of excitons considerably affects the exciton energy structure as the width of the confinement potential approaches the same order as the exciton spatial wavefunction. In this situation, the energy structure of excitons can be established by direct numerical solutions to the three-dimensional Schrödinger equation (SE) for the excitons [54]. This process is somewhat simplified in regards to the degenerate HH and LH valence bands as this degeneracy is lifted due to the dependence of the Hamiltonian on the effective masses of the particles, which can therefore be separated. Solutions to the SE give a quantised energy ladder for electrons and holes in which energy level spacing (and hence for QW thicknesses comparable to or smaller than a_x), the exciton binding energy is dictated by the QW width. A diagram of the energy level structure of QW excitons is shown in Fig 2.3. This means, exciton binding energies can be tuned by varying the width of the QW layer with increasing binding energies for smaller widths.

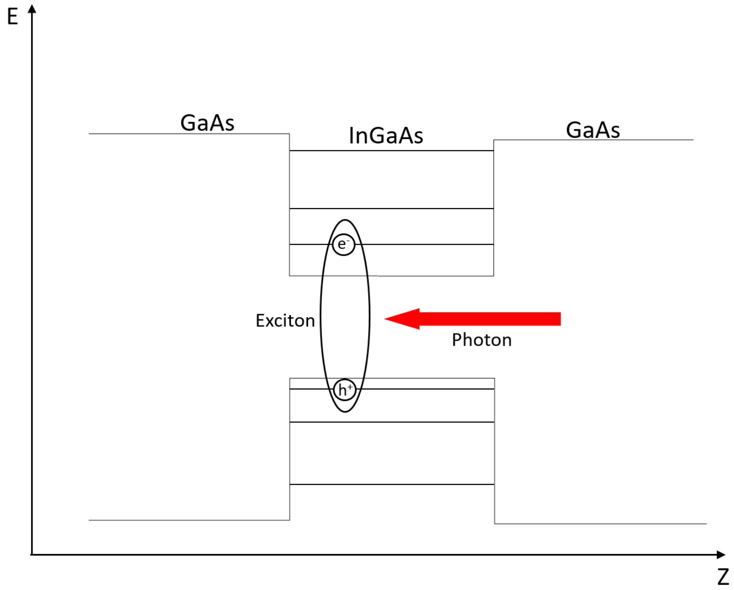

Figure 2.3: ***Quantum well exciton.*** *The thick large-energy band-gap GaAs surrounding the thin, low-energy band-gap InGaAs creates a confinement potential for the electron and hole states, in the growth direction, z, of the QW. The resulting quantised excitonic states can be optically accessed with typical transition energies of in our case, near 1.46 eV*

2.1.2 Exciton-Exciton Interaction

Excitons can be viewed as *composite bosons* which comprise of two fermionic particles which give the exciton its integer spin. The bosonic nature of excitons suggests that excitons can form a Bose gas/condensate which has been theoretically predicted [55] and investigated experimentally [56]. However, while excitons appear to be bosons by way of their integer spin, they cannot be treated as true elementary bosons due to their composite nature despite several attempts to do so in the past [57–59]. This means that interactions between excitons occur through Coulombic interactions of the charge carriers.

Coulombic interactions acts through two main processes. The first process is direct Coulomb scattering that arises from electron-electron, hole-hole and electron-hole Coulomb potentials. The second process is an exchange scattering which acts at short ranges as the exciton's constituent particles come into contact with each other, or more accurately, their wave functions begin to overlap. In work presented in [60] as well as [61], it is shown that in the limit as the transferred exciton wave-vector approaches zero, the contribution from the direct Coulomb scattering also approaches zero, while the contribution from the exchange scattering attains its maximum value. This clearly demonstrates that for excitons with small in-plane wave-vectors, the fermionic exchange scattering dominates over the static Coulomb scattering and is thus the driving mechanism for exciton interactions.

Recently, large dipole-dipole interactions between indirect excitons [44] have been shown to rival, if not exceed, the exchange scattering [43]. Indirect excitons are formed in multi-QW systems, whereby the electron and hole are in adjacent QWs rather than the same QW for direct exciton, and which has been the focus of our discussions in this thesis. Through spatially stretching the exciton over multiple QWs by applying a voltage across the QW layers, a large dipole is formed. This means that several indirect excitons can interact through direct dipole-dipole interactions over larger ranges, providing an appealing alternative to the short range exchange scattering approach. The Coulomb exchange scattering is the dominant mechanism behind polariton-polariton interactions presented later in this thesis.

2.2 Microcavity Polaritons

Microcavity polaritons are half-light/half-matter quasi-particles resulting from the coherent, linear coupling or, *strong coupling*, of photons with semiconductor excitons. First theorised in 1958 by Hopfield [62], polaritons were initially demonstrated as the normal mode coupling between an optical field and bulk semiconductor excitons. Due to the translational symmetry of bulk semiconductors, this imposes that momentum is conserved in all directions which allows the polariton free movement in any direction. Polaritons remained firmly in the realm of bulk semiconductors until significant advancements in semi-conductor growth technology were developed. In 1992, these advancements came to fruition with the first observation of vacuum Rabi splitting by Weisbuch *et.al.* [32] of QW excitons coupled to a Fabry-Pérot microcavity mode. With this one dimensional confinement of the polariton, the polariton field had become quantised along the growth direction of the QW structure, as the translational symmetry is now broken. With the ability to address discrete polariton transitions, microcavity polaritons have become the testbed for exploring quantum fluids of light with remarkable results, such as polariton BEC [2] and polariton superfluidity [63] having been observed.

2.2.1 Exciton Polaritons

When describing polaritons and their physical origins, it is the easiest to view the coupling of N excitons to cavity photons as a sequence of several absorption and emission events. Initially, a photon is absorbed ,creating an exciton. After a short time, this exciton recombines, emitting a cavity photon which is reflected by the cavity mirrors and has a high probability to be reabsorbed by the QW, starting the process again. This exchange of energy between exciton and cavity photon mode is given by the Rabi frequency, Ω_R. If this exchange between the cavity and photons occurs at a much faster rate than any decay mechanisms of the system, then the system is said to be in the *strong coupling regime*, allowing the creation of polaritons: the bound state of photons and excitons. This cycle of coherent exchange between cavity mode photons and excitons can be described by using the exciton equation of motion Hamiltonian in the Rotating Wave Approximation (RWA) in the presence of a photon field. Using the Bose exciton operators, the Hamiltonian of the couple exciton and photon mode becomes:

$$\hat{H} = \sum_k \hbar\omega_C(k)\hat{a}_k^\dagger\hat{a}_k + \sum_k \hbar\omega_X(k)\hat{b}_k^\dagger\hat{b}_k + \sum_k \hbar\Omega_R(k)\left(\hat{b}_k^\dagger\hat{a}_k - \hat{a}_k^\dagger\hat{b}_k\right) \tag{2.4}$$

where ω_C and ω_X are the photon and exciton resonant frequencies respectively, $\hat{a}_k^\dagger(\hat{a}_k)$ and $\hat{b}_k^\dagger(\hat{b}_k)$ are the photon and exciton creation (annihilation) Bose operators respectively and Ω_R is the Rabi frequency or the collective coupling rate of non-interacting excitons to a cavity mode. For excitons in QW nanostructures, the excitons are now confined in the growth direction of the QW structure but still free to move in-plane. The confinement in the growth direction modifies the exciton wavefunction, enhancing the overlap between the electron and hole wavefunctions. In this new system, the exciton momentum is not conserved along the growth axis (z-axis) as the translational invariance of the material is broken along this axis

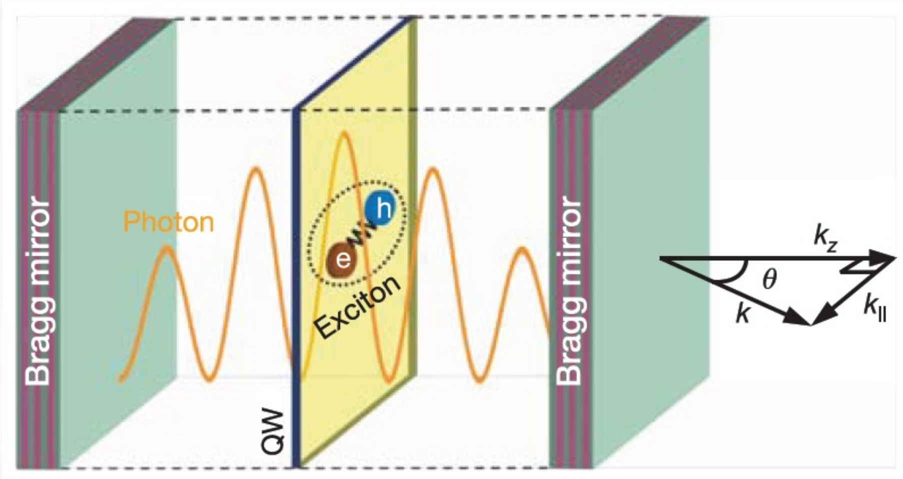

Figure 2.4: ***2D microcavity with QW.*** *To achieve maximum coupling of the QW excitons to the cavity mode, the QW is placed at the anti-node of the electric field inside the cavity. The polariton dispersion curves can be obtained using angle resolved photoluminescence. Image taken from [2].*

due to the QW structure. The Hamiltonian given in Eqn (2.4) can therefore be written in terms of the in-plane momentum so that $k = k_{||}$. With the introduction of 2D excitons, the Rabi frequency can be written thus:

$$\Omega_R = \sqrt{\frac{4\pi\omega_C f_{2D}}{L_{eff}}}\,|\phi(\boldsymbol{r}_a)| \tag{2.5}$$

where f_{2D} is the 2D excitonic oscillator strength, L_{eff} is the effective cavity length, ω_c is the cavity resonant angular frequency and $\phi(\boldsymbol{r}_a) = \frac{E(z_{QW})}{E_{max}}$ is the normalised electric field amplitude at the QW position z_{QW}. The Hamiltonian given in Eqn (2.4), in effect, is described by two harmonic oscillators coupled with strength Ω_R. When the Rabi frequency exceeds the decay rates of the photons and excitons, the system enters the so-called *strong coupling regime* where the photon and exciton states are no longer eigenstates of the system. The system now forms new eigenstates which are superpositions of photons and excitons which are called the Upper Polariton (UP) and Lower Polariton (LP) states. These new eigenstates can be found by applying the Bogoluibov transformation to diagonalise the coupled oscillator Hamiltonian given in Eqn (2.4) to give:

$$\hat{p}_k^{LP} = X_k\hat{a}_k + C_k\hat{b}_k \tag{2.6}$$

$$\hat{p}_k^{UP} = -C_k\hat{b}_k + X_k\hat{a}_k, \tag{2.7}$$

where X_k and C_k are the so-called *Hopfield coefficients* and represent the photonic fraction (C_k) and the excitonic fraction (X_k) of the polariton state. The Hopfield coefficients are given by:

$$|X_k|^2 = \frac{1}{2}\left(1 + \frac{\Delta}{\sqrt{\Delta^2 + 4\Omega_R(k)^2}}\right) \tag{2.8}$$

$$|C_k|^2 = \frac{1}{2}\left(1 - \frac{\Delta}{\sqrt{\Delta^2 + 4\Omega_R(k)^2}}\right) \tag{2.9}$$

where $\Delta = \omega_{cav}(k) - \omega_{exc}(k)$ is the detuning between the cavity and exciton resonances and $\Omega_R(k)$ is the collective coupling rate. The Hamiltonian of the system in the new coupled basis now writes as:

$$\hat{H}_k^{pol} = E_k^{UP}\hat{p}_k^{\dagger}\hat{p}_k + E_k^{LP}\hat{q}_k^{\dagger}\hat{q}_k \tag{2.10}$$

with the eigenenergy dispersion relations for the UP and LP states are given by:

$$E_{LP}^{UP}(k) = \frac{1}{2}\left[E_X(k) + E_C(k) \pm \hbar\sqrt{\Delta^2 + 4\Omega_R(k)^2}\right]. \tag{2.11}$$

where $E_X(k)$ and $E_C(k)$ are the bare exciton and cavity dispersion relations respectively. The polariton states are identified by a distinct energy separation as the cavity resonant energy is tuned across the exciton transition. This separation attains its maximum value when $\Delta = 0$ known, as the *collective Vacuum Rabi Splitting* given by:

$$\Delta E = 2\hbar\Omega_R. \tag{2.12}$$

The polariton states as a function of cavity-exciton detuning and as a function of in-plane wavevector is shown in Fig 2.5 as well as the Vacuum Rabi splitting when $\omega_C = \omega_X$.

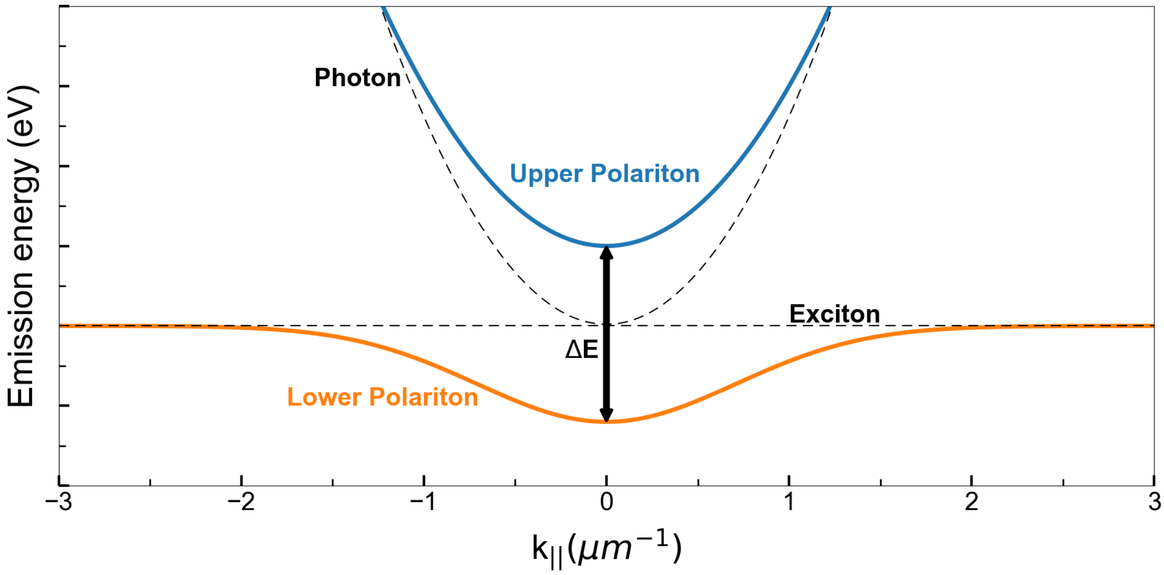

Figure 2.5: ***Exciton polariton dispersion curves.*** *Cavity-exciton detuning is $\Delta = 0$ meV. The curvature of both upper (blue) and lower-polariton (orange) branches is inherited from the photonic-dispersion relation. The black dashed lines denote the bare exciton and photon dispersion relations respectively.*

In Fig 2.5, the dispersion curves are smooth and continuous as the in-plane momentum and hence wavevector, is conserved due to the in-plane symmetry of the QW and thus is able to have a continuum of in-plane momentum. This is why polaritons in this state are often referred to as 2D polaritons. However, if confinement of the polariton state could be imposed on the in-plane axes and full quantum confinement established, momentum conservation would not be conserved in any direction. As a result, the quantisation of the in-plane momentum occurs as can be seen in Fig 2.6 where instead of the smooth, continuous curve seen in Fig 2.5, there are discrete intervals of emission from allowed momenta as the in-plane wavevector is probed. Polaritons in this state are called zero dimensional polaritons (0D polaritons).

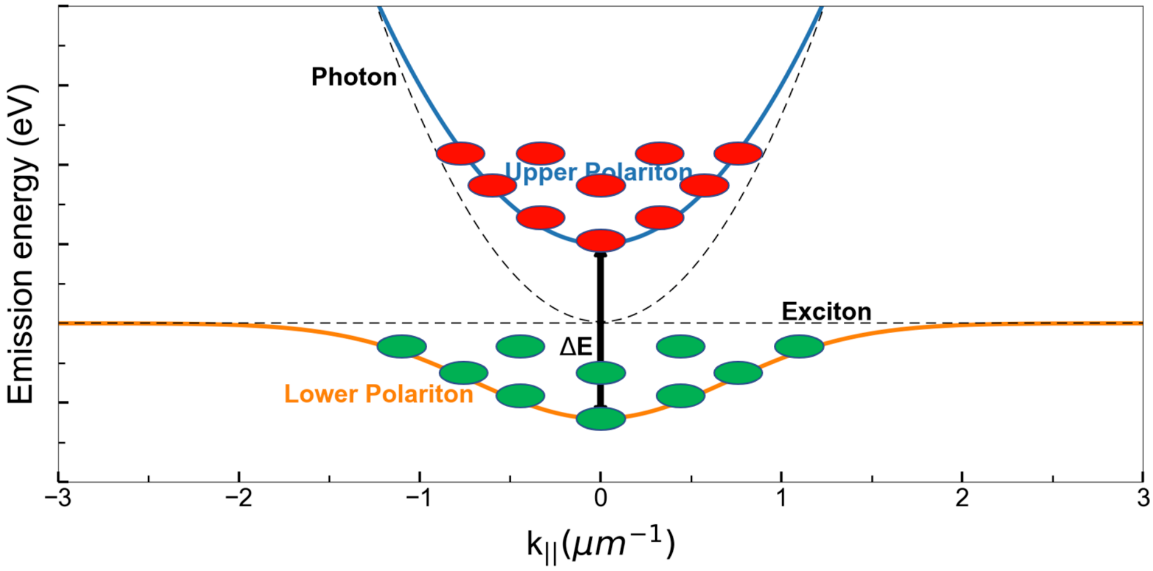

Figure 2.6: ***Zero dimensional polariton dispersion curves.*** *0D polaritons at a cavity-exciton detuning is $\Delta = 0$ meV. The discrete intervals of emission demonstrated by the green and red ovals for the LP and UP respectively across momentum space is a result of in-plane confinement of the polaritons. The orange and blue lines denote the bare (2D) polariton modes and the black dashed lines are the bare exciton and photon dispersion relations respectively.*

From the polariton dispersion, the polariton effective mass is given as the combined mass of the exciton and photon components which are weighted according to the fraction that each component has in the polariton state [64]:

$$\frac{1}{m_{LP}} = \frac{|X|^2}{m_{exc}} + \frac{|C|^2}{m_{cav}} \tag{2.13}$$

$$\frac{1}{m_{UP}} = \frac{|C|^2}{m_{exc}} + \frac{|X|^2}{m_{cav}} \tag{2.14}$$

where X and C are the Hopfield coefficients, $m_{exc} = 0.082m_e$ (in GaAs) is the effective exciton mass of its centre-of-mass motion and m_{cav} is the effective cavity-photon mass calculated from the band curvature of photon dispersion inside the microcavity. Eqn (2.13) gives an effective LP mass in the region of $\mathbf{k} \sim 0$ of $m_{LP} \sim 10^{-4}m_e$, where m_e is the mass of an electron. The very light effective mass of the polariton in the region of $\mathbf{k} \sim 0$ has exposed exciton polaritons as a new and very promising candidate for observing Bose-Einstein condensation (BEC) in solids. The four orders of magnitude lighter effective mass of the polariton than bare excitons means that that reaching polariton BEC is significantly easier, as the critical temperature can four orders of magnitude higher (at the same particle density) and the critical particle density can be four orders of magnitude lower (for the same temperature) than needed to reach the equivalent exciton BEC.

2.2.2 Fabry-Pérot Microcavities

A Fabry-Pérot optical cavity constricts or confines light by the use of two highly reflective mirrors along the optical axis. In between these mirrors, a quantum emitter can be placed to interact with the cavity photons. In cavity-QED experiments, the electric field of the cavity mode must be maximised to ensure the coupling rate between the optical field and the quantum emitter exceeds the optical and material losses of the system. To fulfill this requirement, a cavity with a small effective mode volume while maintaining a high *Q-factor* is critical. The effective mode volume is defined as the physical size of the cavity mode, given by:

$$V_{eff} = \iiint d^3r|\phi(\mathbf{r})|^2 = \frac{1}{4}w_0^2\pi L_{eff} \tag{2.15}$$

where $\phi(\mathbf{r})$ is the normalised electric field amplitude, w_0 is the cavity mode waist radius, and L_{eff} is the effective cavity length. The quality or Q-factor is a dimensionless quantity which describes effectiveness of the cavity to retain or store energy, given by the equation:

$$Q = \frac{\nu}{\delta\nu} = \frac{2L_{eff}\nu}{c}F \tag{2.16}$$

where ν is the cavity frequency, $\delta\nu$ is the cavity linewidth, L_{eff} is the effective cavity length, and F is the cavity *finesse* which is a measure of the effectiveness of the cavity mirror's reflectivity, which is independent of the physical cavity length. The finesse is defined as:

$$F = \frac{\pi\sqrt{R}}{1-R} \tag{2.17}$$

where R is the mirror reflectivity. From Eqn (2.16), the Q-factor of a given cavity can be increased by increasing the physical length component of the effective cavity length L_{eff}. However, the coupling between 2D excitons and cavity photons scales as $\Omega_R \propto 1/\sqrt{L_{eff}}$ (see Eqn (2.5)). Therefore, to achieve the large electric fields for a strongly coupled system, an ultra short cavity length on the order of a few wavelengths of light or increasing the cavity Finesse is needed. To maintain high Q-factors at short cavity lengths, ultra-high reflectivity mirrors (R > 99.999%) must be used, corresponding to a large finesse F.

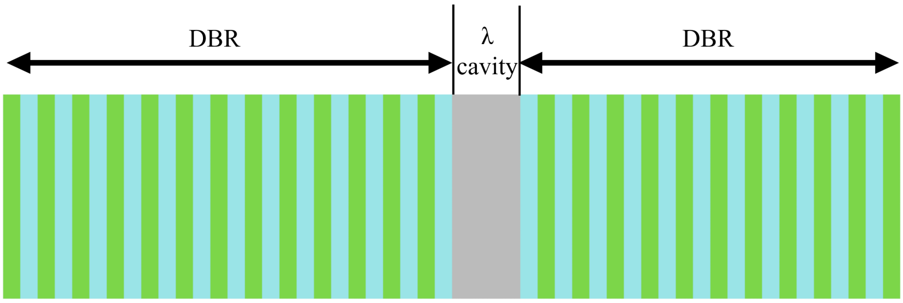

Figure 2.7: ***Planar microcavity profile.*** *The DBR layers sandwich the cavity layer which is on the order of a few wavelengths of light. The DBR layers almost completely reflect light back into the cavity, reducing the cavity loss rate and at the same time helping to maintain large electric field amplitudes inside the cavity.*

The ultra high reflectivity mirrors required for these types of cavities are typically achieved using dielectric *distributed Bragg reflector* (DBR) coatings. DBRs are composed of layers of alternating refractive index dielectric material of thickness $d = \lambda_0/4n_{layer}$ where λ_0 is the wavelength of light and n_{layer} is the refractive index for each material. The DBR operates using the thin film interference principle where some light is reflected from each of the low/high refractive index layer interfaces back towards the cavity. While some light is not reflected back, the successive low/high refractive index layer interface will reflect some of this light back into the cavity as well, and so on. With the thickness of the layers, d, all the reflected light will constructively interfere. With enough pairs of these layers, nearly all of the light is reflected back into the cavity which is shown in Fig 2.7. However, this only occurs in a window around λ_0 known as the stopband as shown in Fig 2.8 and is a function on the number of paired layers.

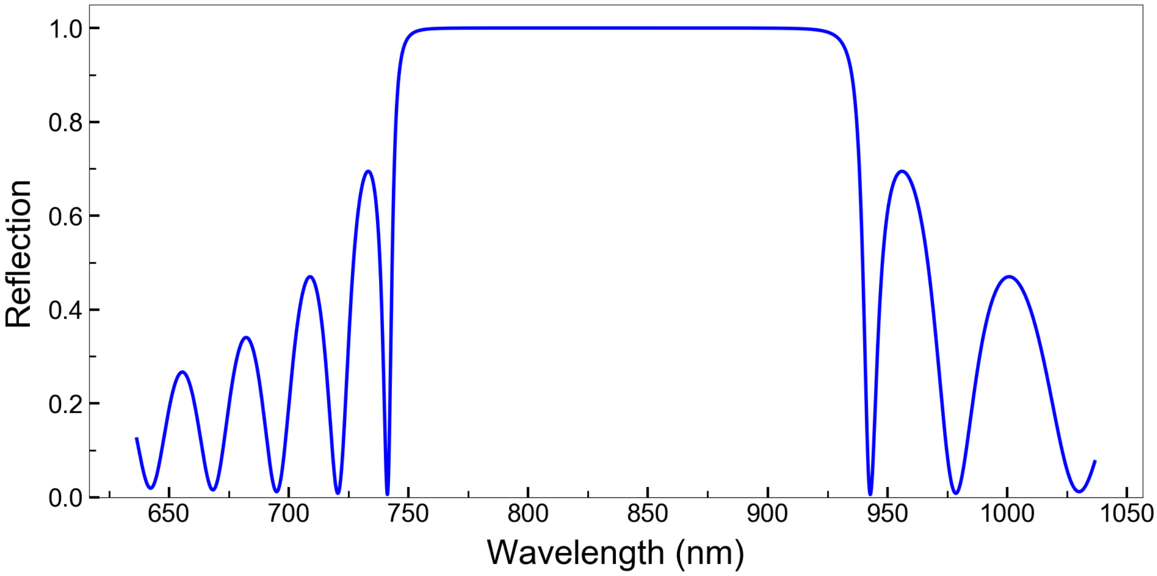

Figure 2.8: ***Stopband function for a dielectric DBR.*** *The calculated stopband function for a DBR with 33 paired layers of* Ta_2O_5/SiO_2 *at 830nm. The blue curve shows reflection efficiency of the cavity. The large high reflectivity window centred at 830nm is know as the stopband. Increasing the number of layers, in principle, reduces the stopband window and increases the reflectivity of the cavity. In practice however, residual absorption in the layers effectively limits the achievable reflectivity (see chapter 3.3).*

To reach the strong coupling regime, the QW is placed inside the microcavity such that it coincides with an anti-node (maximum) of the cavity field. Therefore, the electric field distribution inside the cavity is crucial to the design of the microcavity. The electric field distribution can be calculated using the transfer matrix method [65]. From the transfer matrix simulation of the electric field distribution of a DBR deposited on a fibre tip adjacent to an air gap as part of a fibre-based microcavity in Fig 2.9, it is obvious that the cavity mode penetrates substantially into the mirrors. The penetration depth into the DBR for a typical 2D planar microcavity is:

$$L_{DBR} = \frac{\lambda}{4} \frac{n_1 n_2}{n_1^2 (n_1 - n_2)} \tag{2.18}$$

where n_1 and n_2 are the refractive indices of the DBR layers, $n_1 > n_2$ and λ is wavelength of light. The effective length of the cavity is the sum of the effective optical length of the QW spacer layer (λ / n_{Spacer}) and the penetration depth of the two mirrors multiplied by the square QW spacer layer refractive index [8]:

$$L_{eff} = n_{Spacer}^2 \left(L_{DBR} + \frac{\lambda}{n_{Spacer}} + L_{DBR} \right). \tag{2.19}$$

L_{eff} can be substituted into Eqn (2.5) to obtain a value for the Rabi frequency or coupling strength of the polariton system.

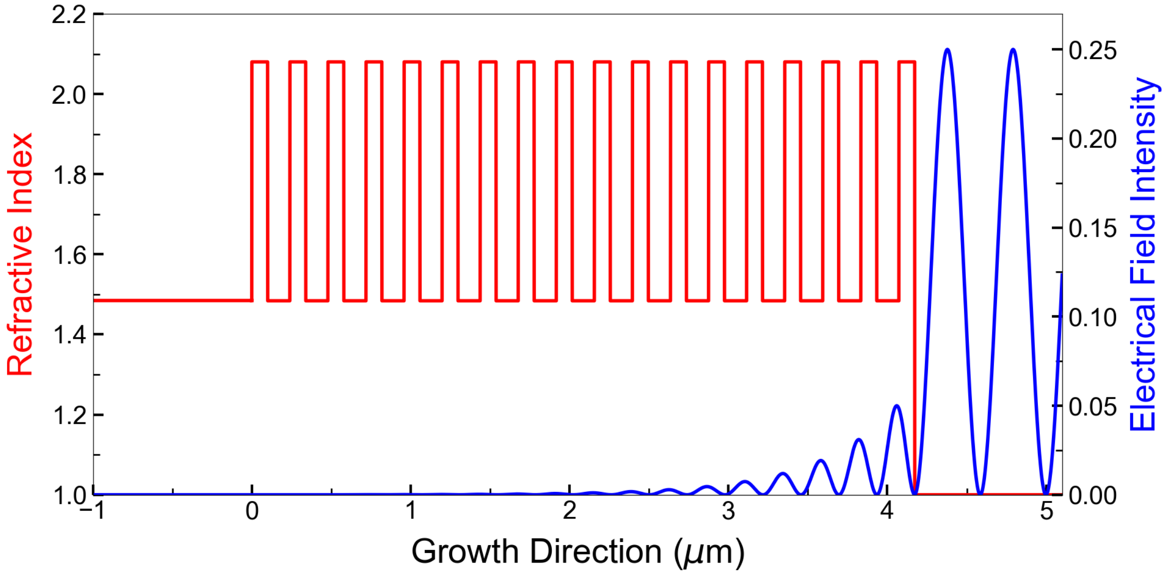

Figure 2.9: ***Electric field distribution for a dielectric DBR.*** *The electric field distribution for the DBR. The red line is the DBR profile while the blue is the electric field intensity.*

2.2.3 Microcavities for Polaritons

For conducting research into microcavity polaritons, the two-dimensional, fully-integrated, monolithic, semiconductor microcavity shown in Fig 2.10 is one of the highest quality and most widely used microcavity designs with Q-factors exceeding 10^5 while maintaining small mode volumes[1] [66]. The electric field distribution inside the cavity can be precisely engineered and fabricated using molecular beam epitaxy (MBE) to produce an anti-node or maximum of the electric field at the QW layer, ensuring the best possible coupling to the QW excitons (see Fig 2.10). The 2D planar microcavity design was later adapted using lithography etching to fabricate pillars with diameters on the μm-scale, the so-called *micropillar* cavity [67]. The micropillar cavity provides a physical, in-plane constraint of microcavity polaritons by constricting the exciton wavefunction, furnishing an excellent platform for the study of confined polariton systems [4]. However, this system typically suffers from enhanced losses and hence reduced coupling due to scattering losses of polaritons from surface states at the edges of the micropillar as the lateral dimensions of the cavity approach the μ-scale. In addition, the wedge like structure of the micropillar cavity critical to the tuning of the resonant cavity energy provides only a limited tunability the range, restricting the detuning parameters over which the system can be probed.

---

[1] In the case of a microcavity coupled to an ensemble of quantum emitters, the collective Rabi splitting is independent of spot size ω_0, but scales with $\Delta E \propto 1/\sqrt{L_{eff}}$.

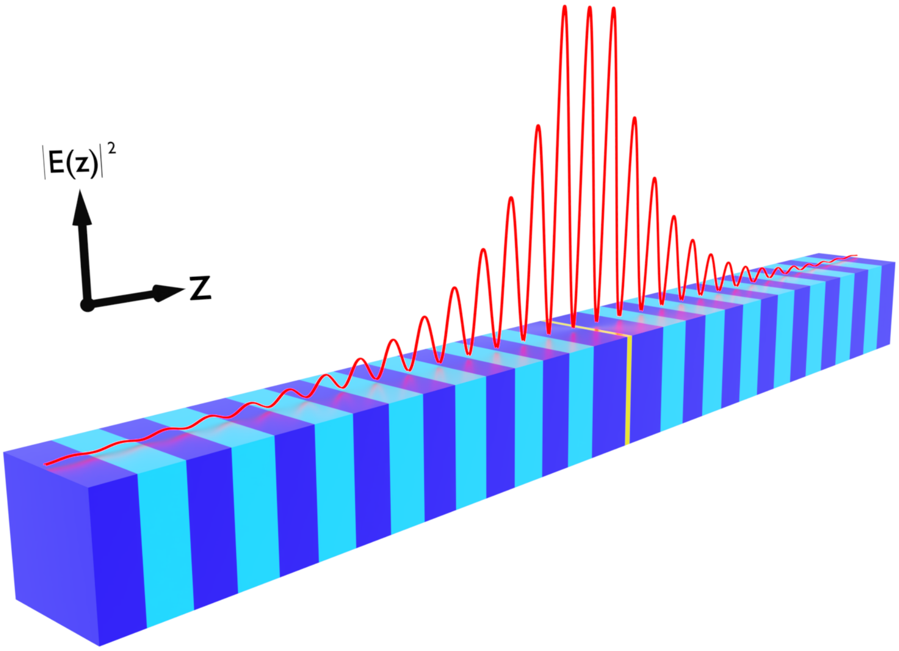

Figure 2.10: ***Planar microcavity with embedded QW.*** *The QW layer (yellow) is sandwiched between two DBR mirrors (alternating dark blue/light blue) which produces a maximum of the electric field at the QW layer (yellow), shown by the red solid line.*

In recent years, open-access, semi-integrated microcavity designs such as fibre-based [68] and silica plates [69], have been shown to offer the same, if not better capability than monolithic designs. These open-access designs replace one of integrated semiconductor DBR mirrors with a completely independent dielectric DBR mirror consisting of paired layers of Ta_2SO_5/SiO_2 which is applied to a concave indentation etched on the mirror surface. The hemispherical (or near hemispherical) geometry of the etch indentations provides a strong optical confinement of the cavity mode which is imprinted into the polariton wavefunction. With optical confinement rather than physical confinement like that of the micropillar, no etching of the planar QW is involved and so it does not suffer the same excitonic losses from cavity side-wall scattering. The open nature of the fibre cavity design also grants independent movement of the fibre mirror, usually controlled by piezo nanopositioners. This independent movement allows an *in-situ* tunability of the cavity resonance without the reduction of coupling experienced by their monolithic counter-parts and usually, over an extended spectral range. The small wedge in the layer design of monolithic microcavities used to change the cavity resonance leads to increased photonic losses and hence, reduction in coupling, as the photons escape laterally away from the cavity mode. In this thesis, we decided to use the fibre-based microcavity design which has the concave indentation etched on a cleaved fibre facet and is coated with a dielectric DBR coating.

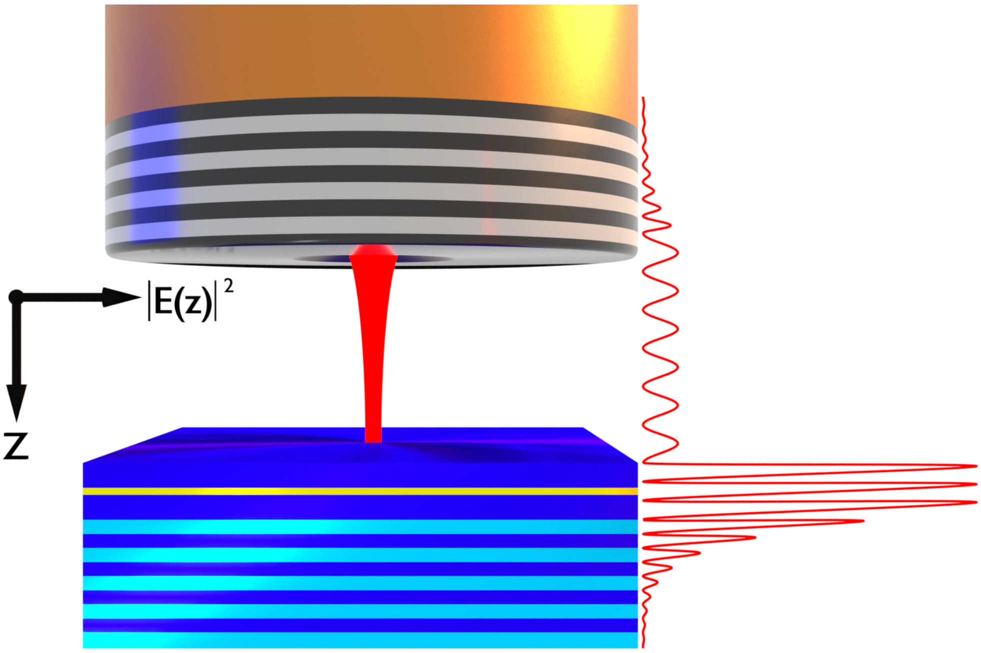

Figure 2.11: ***Fibre microcavity with embedded QW.*** *The fibre microcavity design replaces one of the integrated, semi-conductor DBR mirrors with a machined fibre tip with a DBR mirror coating. Since the electric field distribution is dependent on* $n^2(z)|E(z)|^2$*, the electric field (red solid line) reduces within the air gap.*

The open-accessibility of fibre-based microcavities, while offering greater versatility in terms of tunability, possess a different electric field distribution to the planar microcavity. This is a result of the different materials in the fibre DBR coating as well as the presence of an air gap between the fibre mirror and the QW sample. Unlike Eqn (2.19), one of the DBR penetration depths for the monolithic cavity must be replaced with an air gap, L, and the penetration depth for the fibre mirror coating $L^{DBR}_{Ta_2O_5/SiO_2}$ [68]:

$$L^{DBR}_{Ta_2O_5/SiO_2} = \frac{\lambda}{4}\frac{1}{n_{Ta_2O_5} - n_{SiO_2}} \tag{2.20}$$

where $n_{Ta_2O_5/SiO_2}$ is the refractive index of the respective materials and λ is the optical thickness of the GaAs spacer layer. $L^{DBR}_{Ta_2O_5/SiO_2}$ differs from L_{DBR} because the dielectric DBR starts with a high-index layer as it is surrounded by air (low refractive index), whereas the mirror attached to the bottom of the QW spacer layer starts with a low-index layer as it is surrounded by GaAs. This maintains the low refractive index material on either side of the QW so a phase mismatch will not occur at the air/fibre DBR interface. The effective length of the cavity now reads:

$$L_{eff} = n^2_{Spacer}\left(L_{DBR} + \frac{\lambda}{n_{Spacer}}\right) + L + L^{DBR}_{Ta_2O_5/SiO_2}. \tag{2.21}$$

Even though the fibre cavity has a longer physical length as compared to monolithic cavities, it has a comparable effective length, meaning similar coupling strengths can be achieved with fibre microcavities. With additional information about the fibre mirror and air gap in the cavity, the standard transfer matrix method can be used to determine the electric field distribution inside the fibre microcavity, shown in Fig 2.11. Unlike Fig 2.10, the electric field distribution in Fig 2.11 differs considerably, mainly due to the air gap. However, an anti-node of the electric field is present at the QW layer which validates the fibre microcavity as a viable and powerful alternative microcavity platform for studying confined polariton systems.

2.3 Photon Correlations

In quantum optics, the coherence properties of the state of the photon field are usually described using the $g^{(n)}(\delta n, \delta g, \tau)$ coherence functions, which are normalised correlations of the photon field. The first order coherence function, $g^{(1)}(\tau)$, expresses the phase coherence in time through the normalised, self-correlations of the field amplitude. The phase coherence can provide insight into interference effects, phase modulation and noise as well as round-trip phase accumulation within a system. The second order coherence function, $g^{(2)}(\tau)$, indicates the statistical distribution of photons within the field through the normalised, self-correlations of the field intensity. The statistical distribution of the photons can be categorised into three classes: Poissonian, super-Poissonian and sub-Poissonian, which refer to the fluctuations having equal, larger or smaller variation respectively than that of an uncorrelated, coherent photon state for which the probability of finding N photons in an interval τ is Poissonian. These photon number distributions are defined using the self or auto-correlation version of the second order coherence function, given by:

$$g^{(2)}_{phot}\left(t, t+\Delta t\right) = \frac{\left\langle \hat{a}^{\dagger}\left(t\right)\hat{a}^{\dagger}\left(t+\Delta t\right)\hat{a}\left(t+\Delta t\right)\hat{a}\left(t\right)\right\rangle}{\left\langle \hat{a}^{\dagger}\left(t\right)\hat{a}\left(t\right)\right\rangle\left\langle \hat{a}^{\dagger}\left(t+\Delta t\right)\hat{a}\left(t+\Delta t\right)\right\rangle} \tag{2.22}$$

where $\hat{a}^{\dagger}\left(t\right), \hat{a}\left(t\right)$ are the photon creation and annihilation operators respectively. What this function denotes is the probability of detecting a photon at time $t + \Delta t$ on the condition that a photon was detected at time t. In most steady state systems, t can be dropped as the absolute time is arbitrary, leaving just $g^{(2)}_{phot}\left(\Delta t\right)$. For a Poissonian photon distribution state, $g^{(2)}_{phot}\left(\Delta t\right) = 1$ for all values of Δt, as the fluctuations are random and therefore the probability of detecting two photons at any given time interval is equal. This value would occur for a completely coherent light source such as that of a laser. For a super-Poissonian state, the larger fluctuations than the Poissonian state means that as Δt approaches 0, the probability of detecting two photons becomes more likely. Therefore, we get a value of $g^{(2)}_{phot}\left(0\right) > 1$ and the photons are said to be 'bunched'. This value would occur for a completely incoherent light source such as a candle and is often referred to as 'thermal light'. For the sub-Poissonian photon number state, the reduced fluctuations compared to the Poissonian state means that as Δt approaches 0, the probability of detecting two photons becomes less likely. Therefore, we get a value of $g^{(2)}_{phot}\left(0\right) < 1$ and the photons are said to be 'antibunched'. This value less than 1 demonstrates a granular nature of the photon field as the field is now discretised and can only be interpreted using a quantum definition of light. This means that for values of $g^{(2)}_{phot}\left(0\right) \geq 1$, the photon field can be described using classical (semi-classical) definitions of light, while values $g^{(2)}_{phot}\left(0\right) < 1$ demonstrates the photon field is in a non-trivial, non-classical state which can be described as quantum in nature or, more commonly, as so-called *quantum light*.

2.4 Polariton-Polariton Interaction

When describing microcavity polariton systems, the Hamiltonian given in Eqn (2.4) of two coupled, linear harmonic oscillators has been used as the photons and excitons are both linear systems due to their bosonic natures. While this is true for well separated particles, this description is not complete as was the case for excitons. As the distance between polaritons approaches the exciton Bohr radius $a_X \sim 10$ nm, polaritons will begin to interact due to the exchange-driven Coulomb repulsion of the excitons as explained in Section 2.1.2. This means that interactions must be included in the linear exciton Hamiltonian, which reads as:

$$H_p = \hbar\omega_X \hat{b}^\dagger \hat{b} + \hbar\omega_C \hat{a}^\dagger \hat{a} + \hbar g \left(\hat{a}^\dagger \hat{b} + \hat{a}\hat{b}^\dagger \right) + U \hat{b}^\dagger \hat{b}^\dagger \hat{b}\hat{b} \tag{2.23}$$

$$U = \frac{\hbar\omega_{NL}}{2} \tag{2.24}$$

where $H_{XX} = U\hat{b}^\dagger\hat{b}^\dagger\hat{b}\hat{b}$ is the exciton-exciton interaction Hamiltonian, U is the exciton-exciton interaction strength and ω_{NL} is the nonlinear coefficient. A more appropriate definition of polariton-polariton interactions can be written in the polariton basis. For the lower polariton branch, the Hamiltonian can be written using the lower polariton operator $\hat{p}$ for $k = 0$ [70]:

$$H = \hbar\omega_{LP} \hat{p}^\dagger \hat{p} + H_{pp} \tag{2.25}$$

$$H_{pp} = \frac{1}{2}\frac{a_X^2}{A} V^{pp} \hat{p}^\dagger \hat{p}^\dagger \hat{p}\hat{p} \tag{2.26}$$

where H_{pp} is the polariton interaction term, $A = \pi w_0^2$ is the polariton mode area, and V^{pp} is the effective interaction potential due to exciton-exciton interactions. This interaction potential is described by:

$$V^{pp}_{k,k',q} = \frac{6e^2}{\epsilon a_X} X_{k+q} X_{k'} X_{k'-q} X_k + 2\frac{\hbar\Omega_R}{n_{sat} a_x^2} \left(\left|C_{k+q}\right| X_{k'} + \left|C_{k'}\right| X_{k-q} \right) X_{k'-q} X_k \tag{2.27}$$

where the X_k and C_k are the Hopfield co-efficients defined in Eqns 2.8 and 2.9, and n_{sat} is the polariton saturation co-efficient [70]. The interaction potential is repulsive in nature. In regards to the scope and experiments conducted in this thesis, only the first term which describes direct polariton-polariton interactions is considered and discussed, as the second saturation term is negligible and can be omitted in our case. The contact interaction potential has the structure of a Kerr-like, non-linearity of the polariton state [71]. This translates into a continuous blue-shift in the polariton resonance as the system nonlinearity increases, which can be accomplished by either increasing the polariton population or by increasing the lateral polariton confinement. If polariton nonlinearities could be achieved at the single photon level, sizeable quantum correlations could be induced, enabling microcavity polaritons to become ideal platforms for studying drive-dissipative quantum fluids of light [72], Hamiltonian simulations with light [15, 73, 74], and possible realisation of non-trivial, out-of-equilibrium phase transitions [75, 76].

It is also important to mention that even though the saturation term, n_{sat}, is negligible and can be omitted in our case, this may not always be so. Very recently, there has been both theoretical and experimental work exploring the potential extent and effect the exciton saturation correction of the polariton interaction potential has on the polariton interaction strength [77, 78]. Measured polariton-polariton interaction strengths of polariton condensates [77] has showed interaction strengths larger than predicted values using the contact polariton-polariton interaction constant. This discrepancy is postulated to result from the effect of saturation of the exciton oscillator strength which can become significant at large densities and Rabi splittings ($\Omega_R \approx$ polariton binding energy).

2.4.1 Polariton Blockade - Photonic Dot

The polariton interaction in Eqn (2.27) is proportional to the polariton population densities controlled by either the number of particles or the amount of spatial confinement. In microcavities at low excitation laser intensities corresponding to low polariton densities, polariton-polariton interactions are typically negligible. As a result, microcavity polariton systems, to a good approximation, display a linear energy structure making these systems of limited value to developing quantum fluids of light or integrated quantum devices. However, if polariton-polariton interactions could be enhanced such that substantial system non-linearities occur at the few particle level, the presence of a single polariton would inhibit the injection of another polariton due to the interaction-induced blue-shift of the polariton resonance. In this regime, the system is said to be in the so-called *quantum polariton blockade regime*, analogous to the photon blockade observed with atoms [21], quantum dots [22] and super-conducting devices [79].

In 2006, Verger *et.al.* [42] proposed the quantum polariton blockade for microcavity exciton polaritons with embedded QWs. Here we summarise their findings relevant for our work. In their paper, they theorised that if the lateral size of the polariton wavefunction could be confined sufficiently through its photonic component, polariton-polariton interactions, U, would blue-shift the polariton transition energies to the point where they exceed the polariton linewidth, γ_{LP}. In this event, the presence of one polariton will inhibit the injection of a second polariton as the two-polariton transition is blue-shifted to higher energies and out of resonance with the incoming laser-photon energy as illustrated in Fig 2.12. For $U >> \gamma_{LP}$, under a CW laser drive tuned at resonance with the LP states, only one polariton is present in the system at any given time. Therefore, the system could generate a train of single photons with a repetition interval close to the polariton lifetime. The photon correlations of the emitted light from the system, defined by the second-order autocorrelation function, $g^{(2)}(\Delta\tau)$, is expected to exhibit an anti-bunching dip with $g^{(2)}(0) < 1$. In their treatment of the microcavity system, Verger *et.al.* used the exciton Hamiltonian [80, 81] describing the coupling of QW excitons to planar microcavity photon modes. The Hamiltonian is simplified by considering only the fundamental 'photonic dot' mode due to the large spacing between confined photon modes. This simplification is completed by taking the exciton spatial wavefunction to be the same as the photonic dot, $\phi_C(\mathbf{x})$, as each photon mode only couples strongly to the exciton mode with the same spatial wavefunction. The simplified effective Hamiltonian reads as:

$$\begin{aligned}\hat{H}_{eff} =& \hbar \Big[\omega_X \hat{b}^\dagger \hat{b} + \omega_C \hat{a}^\dagger \hat{a} + \Omega_R \left(\hat{b}\hat{a}^\dagger + \hat{b}^\dagger \hat{a}\right) + \frac{\omega_{nl}}{2} \hat{b}^\dagger \hat{b}^\dagger \hat{b}\hat{b} \\ & - \alpha_{sat}\Omega_R \left(\hat{a}^\dagger \hat{b}^\dagger \hat{b} + \hat{b}^\dagger \hat{b}^\dagger \hat{a}\right) \hat{b} + \mathcal{F}_0(t) e^{-i\omega_p t} \hat{a}^\dagger + \mathcal{F}_0^*(t) e^{-\omega_p t} \hat{a}\Big]\end{aligned} \tag{2.28}$$

where $\hat{a}(\hat{a}^\dagger)$ and $\hat{b}(\hat{b}^\dagger)$ are the respective cavity and exciton annihilation (creation) operators and Ω_R is the vacuum Rabi frequency. The parameters of note here are $\mathcal{F}_0(t)$, which is the pump laser projection onto the photonic dot mode, $\alpha_{sat} = \frac{1}{n_{sat}} \int d\mathbf{x}\, |\phi_C(\mathbf{x})|^4$ and $\omega_{nl} =$

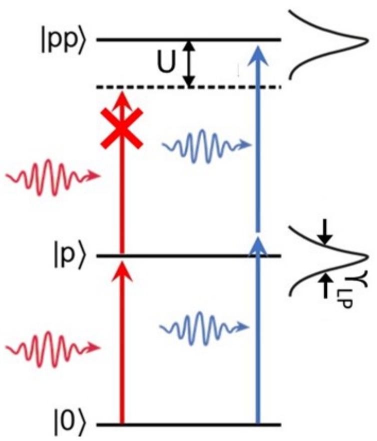

Figure 2.12: ***Polariton excitation ladder.*** *With significant polariton-polariton interactions, the two-polariton state is blue-shifted to higher energies by an amount, U. If this shift is larger than the polariton linewidth, γ_{LP}, the two-polariton state can no longer be populated as photons resonant (or slightly red detuned) to the single-polariton state are of insufficient energy (red lines). However, there is an increased probability for two photon processes to excite the two photon state with blue detuned photons.*

$\kappa \int d\mathbf{x}\, |\phi_C(\mathbf{x})|^4$ are the effective nonlinear coefficients, with n_{sat} the exciton oscillator strength saturation density and κ is the excitonic loss rate. The saturation coefficient α_{sat} is negligible in typical type III-V microcavity experiments and is ignored in further considerations. Thus, ω_{nl} is the dominating nonlinear term that is greatly dependent on the photonic dot confinement volume. Through study of simple geometries such as a square or cylinder for the photonic dot or photon cavity modes, the geometric overlap integrals are:

$$\int_{square} d^3\mathbf{x}\, |\phi_C(\mathbf{x})|^4 = \frac{2.25}{L^2} \tag{2.29}$$

$$\int_{cylinder} d^3\mathbf{x}\, |\phi_C(\mathbf{x})|^4 = \frac{2.67}{(2R)^2} \tag{2.30}$$

where L is the lateral size of the square and R is the radius of a cylinder. Clearly from integrals above, there is an inverse proportionality between ω_{nl} and the lateral area of cavity mode, A. In our case, the overlap integral uses a Gaussian geometry:

$$\int_{Gaussian} d^3\mathbf{x}\, |\phi_C(\mathbf{x})|^4 = \pi\omega_0^2. \tag{2.31}$$

To better study the quantum dynamics of the system and apply it to actual experimental parameters, the Hamiltonian given in Eqn (2.28) is moved into the interaction picture to remove the bare exciton and photon energies:

$$H_{\text{eff}} = \hbar\,\Delta\omega_X \hat{b}^\dagger\hat{b} + \hbar\,\Delta\omega_C \hat{a}^\dagger\hat{a} + \hbar\Omega_R\,(\hat{b}^\dagger\hat{a} + \hat{a}^\dagger\hat{b}) + U\hat{b}^\dagger\hat{b}^\dagger\hat{b}\hat{b} + \hbar\,\mathcal{F}(t)(\hat{a}^\dagger + \hat{a}) \tag{2.32}$$

where $\Delta\omega_C = \omega_C - \omega_p$, $\Delta\omega_X = \omega_X - \omega_p$, ω_C and ω_X are the cavity and exciton resonant frequencies respectively, and $\mathcal{F}(t)$ is the applied laser pump of frequency ω_p and $U = \frac{\hbar\omega_{nl}}{2}$. $\Delta\omega_C$ and $\Delta\omega_X$ can be related to actual experimental parameters such as cavity-exciton detuning, Δ, and laser pump-lower polariton detuning, Δ_{LP}, by using the following relations:

$$\Delta\omega_C = \Delta/2 - \Delta_{LP} + \sqrt{\Omega_R^2 + \Delta^2/4} \tag{2.33}$$

$$\Delta\omega_X = \Delta\omega_C - \Delta \tag{2.34}$$

$\mathcal{F}(t) = \sqrt{P(t)\gamma_C/\hbar\omega_p}$ is the dimensionless, time-dependent, photon–field drive with $P(t)$ as the input power to the cavity mode and γ_C is the cavity decay rate. To characterise the time evolution of this system in the presence of dissipation and loss, the master equation for this system is given using the density matrix of the system, $\rho(t)$, and the homogeneous linewidths of the photon and excitons respectively, γ_C and γ_X:

$$\begin{aligned}\frac{d\hat{\rho}}{dt} = \frac{i}{\hbar}\left[\hat{\rho}, \hat{H}_{\mathrm{eff}}\right] + \frac{\gamma_C}{2}\left(2\hat{a}\hat{\rho}\hat{a}^\dagger - \hat{a}^\dagger\hat{a}\hat{\rho} - \hat{\rho}\hat{a}^\dagger\hat{a}\right) \\ + \frac{\gamma_X}{2}\left(2\hat{b}\hat{\rho}\hat{b}^\dagger - \hat{b}^\dagger\hat{b}\hat{\rho} - \hat{\rho}\hat{b}^\dagger\hat{b}\right).\end{aligned} \tag{2.35}$$

This master equation can be solved by expanding the density matrix over a Fock basis of the photon and exciton fields.

Using the quantum regression theorem [82], the two-time, second-order coherence function, $G^{(2)}_{phot}(t,t')$ for the photon field can be found thus:

$$G^{(2)}_{phot}(t,t') = \mathrm{Tr}\left(\hat{a}\, U(t,t')\left[\hat{a}\,\rho(t')\hat{a}^\dagger\right]\hat{a}^\dagger\right), \tag{2.36}$$

with its normalised version given as:

$$g^{(2)}_{phot}(t,t') = \frac{\mathrm{Tr}\left(\hat{a}\, U(t,t')\left[\hat{a}\,\rho(t')\hat{a}^\dagger\right]\hat{a}^\dagger\right)}{\mathrm{Tr}\left(\hat{a}\,\rho(t)\hat{a}^\dagger\right)\mathrm{Tr}\left(\hat{a}\,\rho(t')\hat{a}^\dagger\right)} \tag{2.37}$$

where $U(t,t')$ is the evolution super-operator that acts on the density matrix as $\rho(t) = U(t,t')\,\rho(t')$. With the framework in place to determine the time evolution of the system along with the accompanying photon statistics, Fig 2.13 gives an example of the second-order coherence function, $g^{(2)}_{phot}(0)$, as a function of laser detuning from the lower polariton (LP) resonance for several values of Δ.

It should be noted that the results in Fig 2.13 are obtained numerically solving Eqn (2.35) for a system under CW laser excitation, in the steady state. However, it is interesting to note that an analytic solution has also been found for $g^{(2)}_{phot}(0)$ under weak CW, resonant excitation [83]. This analytic solution reads:

$$g^{(2)}_{phot}(0) = \frac{1 + 4\left(\Delta E_L/\hbar\kappa\right)^2}{1 + 4\left(\Delta E_L + U\right)^2/\hbar^2\kappa^2} \tag{2.38}$$

where $\Delta E_L = \hbar(\omega_{Laser} - \omega_{cavity})$ is the cavity-laser detuning and $\kappa = 1/\gamma$.

In Fig 2.13, the laser frequency is red detuned from the LP resonance, showing $g^{(2)}_{phot}(0) < 1$, meaning antibunched light. This occurs due to interactions shifting the two-polariton transition further out of resonance from the pump, reducing the likelihood of exciting of the higher polariton transition. The second-order correlation function decreases even further in the same region for increasingly positive Δ as shown by the three curves in Fig 2.13. This is due to the increased excitonic content of the polariton mode, leading to more interactions. However, for excitation frequencies blue-detuned from the polariton resonance, the nonlinearity now enhances the probability of exciting the higher polariton transitions, as the interaction induced blueshift brings the two-polariton transition into resonance with the pump. As a result $g^{(2)}_{phot}(0) > 1$ i.e photon bunching.

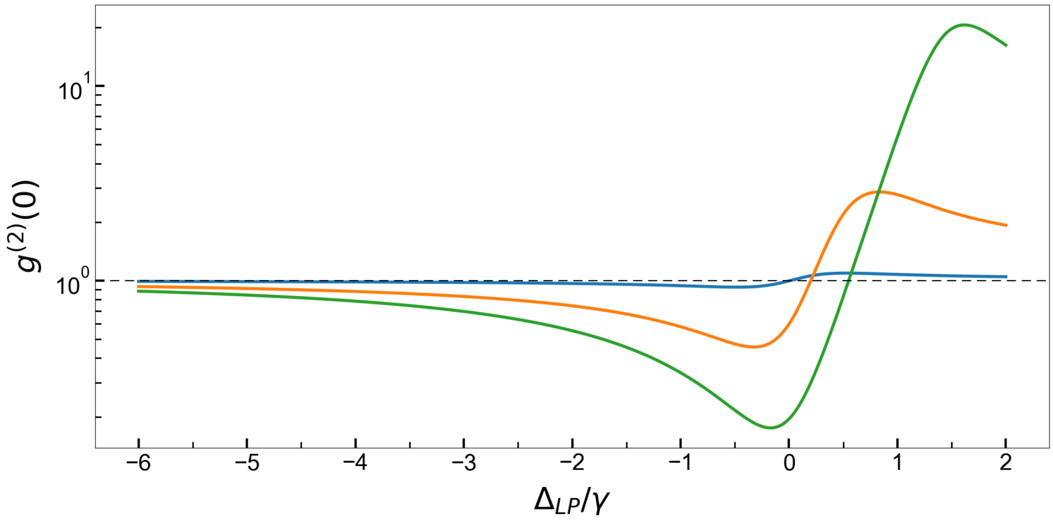

Figure 2.13: ***Second order coherence function as a function of laser-polariton detuning.*** *The three traces are for different cavity-exciton detunings (blue = −5 meV, orange = 0 meV and green = 5 meV) across the polariton avoided crossing. These traces were produced using the parameters:* $\hbar\gamma_X = \hbar\gamma_C = 0.1$ *meV,* $\hbar\Omega_R = 2.5$ *meV, polariton interaction strength* $\hbar\omega_{nl} = 0.4$ *meV, pump field* $\hbar F = 0.1$ *meV and* $\Delta_{LP} = 0$.

While the laser-polariton detuning is fundamental to the dynamics of the photon statistics, the minimum value that $g^{(2)}_{phot}(0)$ can attain for a given Δ depends crucially on the ratio $\frac{U}{\hbar\gamma_{LP}}$ where $U = \frac{\hbar\omega_{nl}}{2}$, which compares the strength of the polariton interactions, U, to the polariton linewidth, $\hbar\gamma_{LP}$. This value will give an indication of the energy shift required for the suppression of the two-polariton transition amplitude.

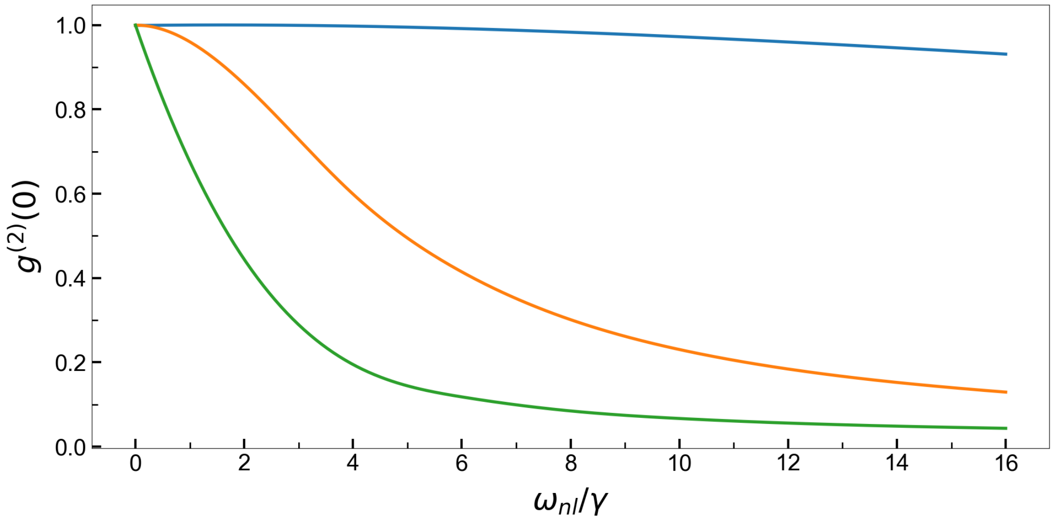

Figure 2.14: ***Second order coherence function as a function of normalised nonlinear coefficient.*** *The three traces are for different cavity-exciton detunings (blue = −5 meV, orange = 0 meV and green = 5 meV) across the polariton avoided crossing. These traces were produced using the parameters:* $\hbar\gamma_X = \hbar\gamma_C = 0.1$ *meV,* $\hbar\Omega_R = 2.5$ *meV,* $\hbar F = 0.1$ *meV and* $\Delta_{LP} = 0$.

In Fig 2.14, the dependence of $g^{(2)}_{phot}(0)$ as a function of $\frac{\omega_{nl}}{\gamma}$ is illustrated for three different Δ. The best antibunching, as was the case in Fig 2.13, is obtained for increasingly positive Δ, which is expected due to the larger excitonic content of the LP mode. The antibunching behaviour becomes significant for values of $\frac{\omega_{nl}}{\gamma} \approx 1$ which is a result of the reduced overlap between the two-polariton transition and the pump energy as the transition resonance is shifted to higher energies by polariton interactions.

Once these ratios are large enough, a value of $g^{(2)}_{phot}(0) < 0.5$ can be attained, indicating that the system is emitting single photons and has entered the strong quantum blockade regime. This would suggest a good system in which to see this effect would be one with a narrow linewidth LP mode, meaning a very high quality QW sample and also tight optical confinement as ω_{nl} is inversely proportional to the lateral area of the photonic mode (see Eqn (2.30)). The physics described in this section occurs at the few particle level such that the presence of a single particle in the system creates a large, nonlinear response of the system. This would suggest that the model is only valid for weak excitation of the system. In Fig 2.15, the value of $g^{(2)}_{phot}(0)$ is shown for normalised incident intensity F/γ. Clearly for low incident intensities, $g^{(2)}_{phot}(0)$ plateaus as N_{ph} is steadily decreasing. At high intensities, $g^{(2)}_{phot}(0)$ increases as N_{ph} grows with a linear behaviour which begins to flatten out as $g^{(2)}_{phot}(0) \rightarrow 1$. This supports the validity of this model in the weak excitation regime such that $F/\gamma \ll 1$.

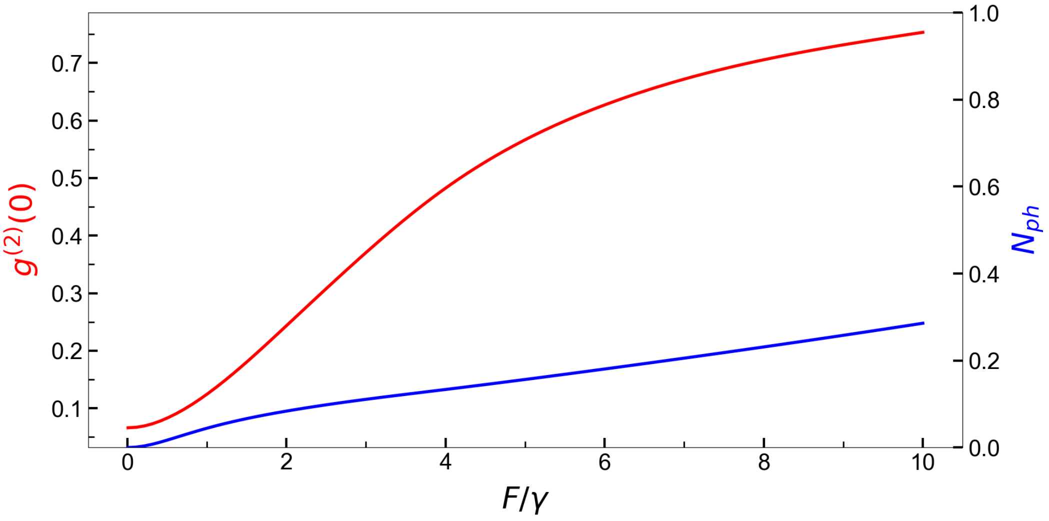

Figure 2.15: ***Second order coherence function at zero time delay*** $g^{(2)}(0)$ ***as a function of pump power.*** *The blue line shows the intra-cavity photon number and the red line shows the value of* $g^{(2)}(0)$. *These traces were produced using the parameters:* $\hbar\gamma_X = \hbar\gamma_C = 0.1$ *meV,* $\hbar\Omega_R = 2.5$ *meV,* $\hbar\omega_{nl} = 1.0$ *meV, and* $\Delta_{LP} = 0$.

2.4.2 Pulsed Excitation Regime

The Verger *et.al.* paper gives a detailed analysis of the polariton-polariton interactions in the steady state under CW excitation. In experiments conducted in this thesis, due to technical reasons (see section 3.5.3), pulsed excitation is used which necessitates that we understand the system dynamics under pulsed excitation very well.

In the pulsed regime, the driving photon field (the laser) is time-dependent, which invalidates the steady state solutions found in [42] and therefore the full master equation given in

Eqn (2.35) must be solved. We now solve the two-time correlation $g^{(2)}_{phot}(t, t')$ given in Eqn (2.37) over a range of t and t' values with actual experimental parameters. As the value of the nonlinear co-efficient is unknown, we use a value of 0.01 meV for the nonlinear coefficient as a sensible starting point based on the literature [3, 84].

The calculation of the two-time correlation function is performed by treating the Master equation as a time-dependent matrix differential equation. The Fock basis for the photon and exciton operators are truncated by limiting the number of excitations in the photon and exciton modes. Depending on laser power, a range of excitations was found to be an adequate range in each mode.

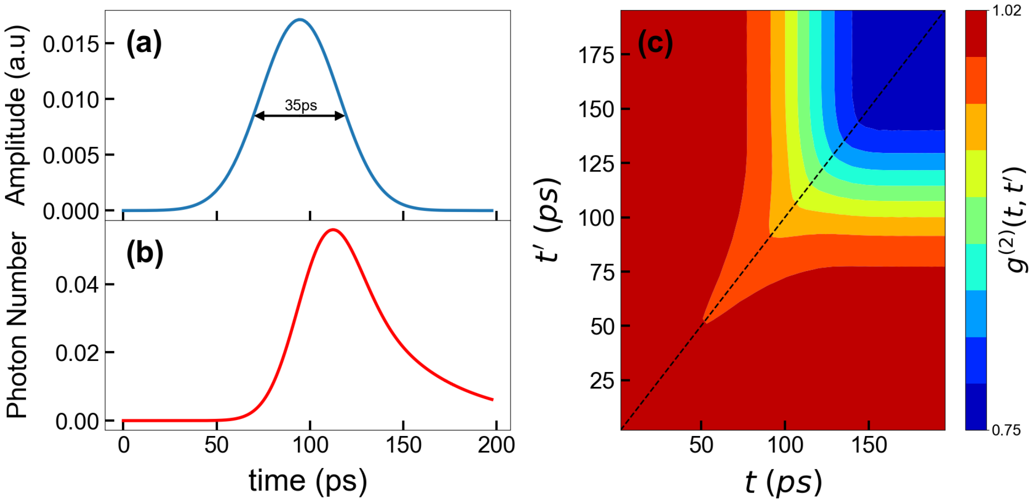

Figure 2.16: ***Two-time photon correlation map for pulsed excitation.*** *(a) 35ps laser pulse profile for time scale reference. (b) Intra-cavity photon number over the duration of the laser pulse. (c) the two-time photon correlation,* $g^{(2)}_{phot}(t, t')$*, map for all combinations of* t *and* t'*. The black dotted line indicates* $g^{(2)}_{phot}(t, t')$*. Parameters:* $\hbar\gamma_x = 0.0621 meV$*,* $\hbar\gamma_c = 0.0411 meV$*,* $\hbar\omega_{nl} = 0.01\, meV$*,* $\hbar\Omega_R = 1.4\, meV$*,* $\Delta = 1.1\, meV$*,* $\Delta_{LP}/\gamma = -0.875$ *and average incident power* $P = 15\, pW$*.*

In Fig 2.16, graphs (a) and (b) show the input laser pulse (a) and intra-cavity photon number (b) respectively. The photon number reaches it's maximum value ~30 ps (approximate cavity lifetime) after the peak of the pulse has occurred. This is due to the build up of photons inside the cavity which then 'leak out' at a rate given by the cavity lifetime, hence the exponentially decaying tail of the photon number. These two figures, Fig 2.16, graphs (a) and (b), give an indication of the picosecond timescales when photon correlations change (Fig 2.16 (c)) relative to the laser pulse profile. Fig 2.16 (c) shows the two-time photon correlation $g^{(2)}_{phot}(t, t')$ for the 35 ps pulse shown in graphs (a) and (b). To find a value of $g^{(2)}_{phot}(0)$, we follow a line where $t = t'$, indicated by the black dotted line. Clearly, the value of $g^{(2)}_{phot}(0)$ begins to drop as the photon population grows due to the creation of polaritons in the system. At the maximum photon population, polariton interactions will have attained their peak strength. Photon correlations, however, have not reached a minimum yet, although the value is significantly less than 1. As the pulse passes and the system decays, the minimum value for $g^{(2)}_{phot}(0)$ is achieved, approximately one lifetime after the peak photon number is reached. It must be stated that the value of $g^{(2)}_{phot}(0)$ in the dark blue region of graph (c) will remain at this value at longer times, even as photons in the system diminish. This is counter-intuitive to what might normally be expected where the value of $g^{(2)}_{phot}(0)$ should converge to 1 at longer timescales. This would be expected for CW excitation as the cavity is constantly replenished with photons, thus correlations on short time scales dominate over long time scale correlations. As such, this dark blue region could lead to the conclusion that this region is a numerical artifact in the simulation. However, we believe this simulation to be accurate and faithful representation of the system we are studying under pulsed excitation. This view can be taken as nearly all the photons that enter the cavity from the short laser pulses interact nonlinearly via polariton interactions, acquiring correlations, before leaking out of the cavity (see Fig 2.16 (a) and (b)). As the photons decay out of the cavity, the photons that left the cavity are still correlated with those that remain as they were initially correlated. Therefore, correlations will exist for arbitrarily long time periods, thus, $g^{(2)}_{phot}(t, t')$ will be sub-Poissonian for arbitrarily large $|t - t'|$. Importantly, however, the photon numbers used to calculate the correlation drops exponentially (see Eqn (2.22)) where both the numerator and denominator are dropping exponentially. This makes looking at correlations at ultra long timescales impractical as they are impossible to measure.

The simulations in Fig 2.16 show that non-trivial photon correlations can be achieved within the range of our experimental parameters. However, the simulations only show the pure system dynamics, not as actual measurements of the emitted photons. This is because measurements of the emitted photons do not truly find $g^{(2)}_{phot}(t, t')$ as defined in Eqn (2.37) within each laser pulse. This is due to the inadequate time-resolution of the detection electronics typically used to measure photon, in our case, the Hanbury-Brown and Twiss (HBT) interferometer (this point is explained in more detail in section 3.5.3). Briefly, the Hanbury-Brown and Twiss interferometer uses a 50/50 beamsplitter to split the emitted photons into two separate channels which are then detected using two avalanche photo-diodes (APD) and the detection events are correlated. Ideally, one APD would be used, however, the detection repetition rate is far too slow to properly sample the photon stream and would give erroneous results. Two detectors are therefore used to alleviate this problem. However, even with two detectors, the dynamics of some experimental systems occur at smaller timescales than the overall system can resolve. This is the case in our experiments where individual pulses cannot be resolved. This means that over many pulses, all possible coincidences between t and t' are recorded and binned together as there is no information about when the photons are emitted within the pulse. Therefore, to give a theoretical model which can be directly compared to the experiment, we integrate over all possible combinations of t and t' within the duration of each pulse which is then normalised to the total incident photon flux [85]:

$$g^{(2)}_{phot}(0) = \frac{2\int_{-T}^{T} dt_1 \int_{-T}^{T} dt_2\, G^{(2)}(t_1, t_2)}{\int_{-T}^{T} dt_1 \int_{-T}^{T} dt_2\, I(t_1)I(t_2)} \tag{2.39}$$

where the limits of the integral (-T, T) define the full duration of each pulse and $I(t) = \mathrm{Tr}\left[\rho(t)\,\hat{a}^{\dagger}\hat{a}\right]$ is the average photon flux from each detector at time t. This has the effect of averaging over the entirety of Fig 2.16 (c), leading to larger values of $g^{(2)}_{phot}(0)$ than is actually present.

Given the revised definition of $g^{(2)}_{phot}(0)$ of Eqn (2.39), realistic values of the photon statistics can be simulated. Fig 2.17, Fig 2.18 and Fig 2.19 show the value of $g^{(2)}_{phot}(0)$ as a function of laser detuning for various Δ's, $g^{(2)}_{phot}(0)$ as a function of interaction strength and $g^{(2)}_{phot}(0)$ as a function of incident pump power, respectively. Each graph also shows the equivalent steady state (CW) simulations (dotted lines) for the same experimental parameters. Clearly, the pulsed scenario produces values of $g^{(2)}_{phot}(0)$ closer to 1 than the CW scenario in all cases which would be at least partly due to the averaging over $g^{(2)}_{phot}(t,t')$ as a result of the time-resolution of the detectors. Other factors contributing to this outcome could be from the spectral overlap between the laser pulse and the polariton transition for the given parameters which could see an increased probability of exciting the two-polariton manifold.

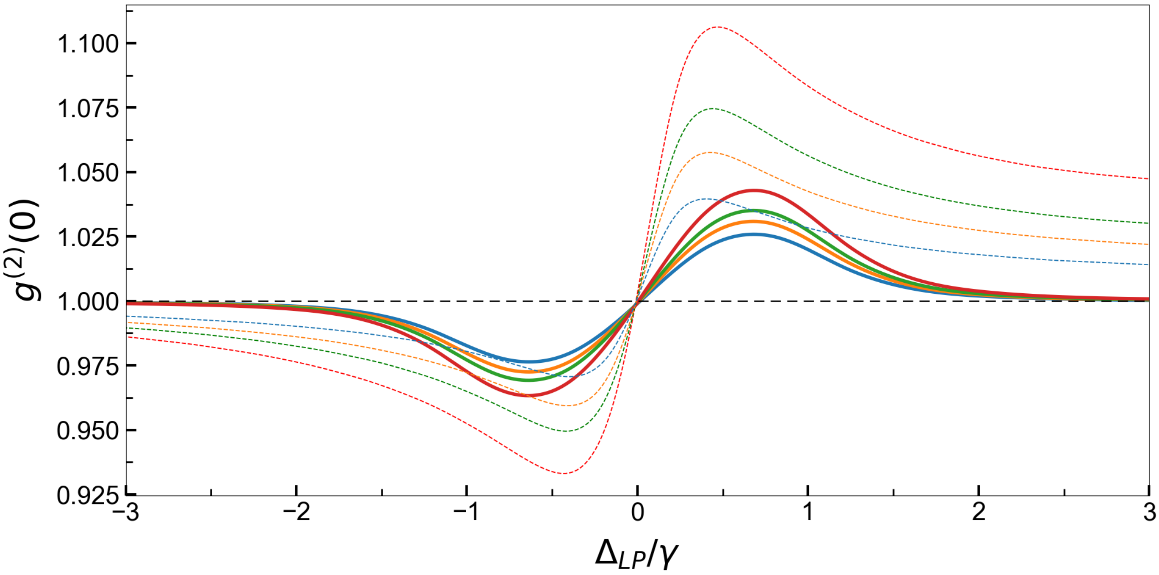

Figure 2.17: ***Second order autocorrelation at zero time delay*** $g^{(2)}(0)$ ***as a function of laser-polariton detuning for pulsed excitation.*** *The solid curves show the pulsed regime simulations while the dashed curves show the corresponding CW (steady state) regime simulations using the same experimental parameters for comparison for different cavity-exciton detunings* Δ *(blue* $= -0.5$ *meV, orange* $= 0$ *meV, green* $= 0.4$ *meV and red* $= 1.1$ *meV) moving across* $\Delta = 0$*. Parameters:* $\hbar\gamma_x = 0.062$ *meV,* $\hbar\gamma_c = 0.041$ *meV,* $\hbar\omega_{nl} = 0.01$ *meV,* $\hbar\Omega_R = 1.4$ *meV, pulse duration = 35 ps and average incident power* $P = 40$ *pW.*

In Fig 2.17, the pulsed simulations demonstrate that the best antibunching values of $g^{(2)}_{phot}(0)$ are obtained for increasingly positive Δ's, which is consistent with the increasing excitonic fraction of the LP mode and what is seen in Fig 2.13. When compared to the steady state simulations, the maximum and minimum values of the pulsed simulations are shifted further away from the LP mode resonance while the the value of $g^{(2)}_{phot}(0)$ returns to 1 much closer to the LP resonance. This a result of the spectral overlap of the laser pulse and the LP linewidth, which is explained in more detail later in section 3.5.3 of this thesis.

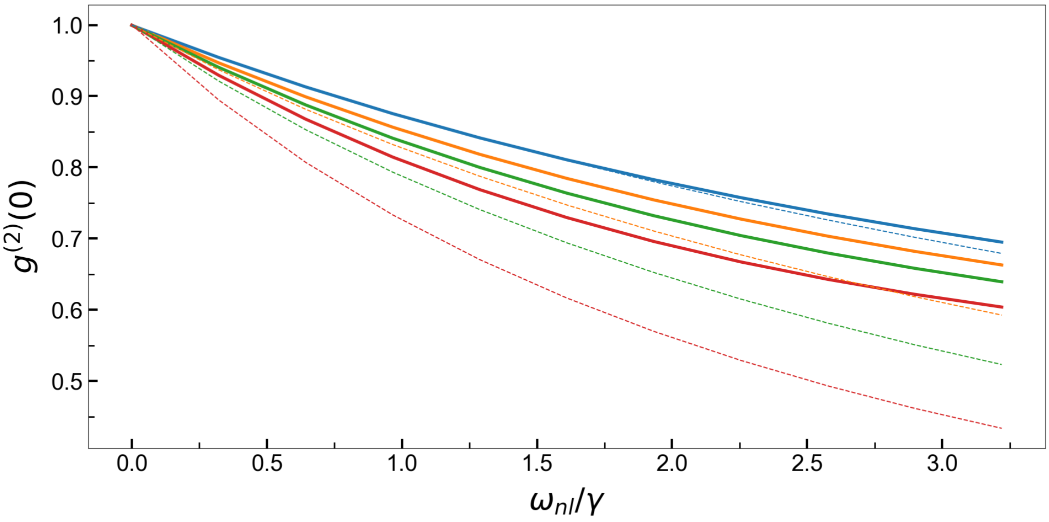

Figure 2.18: ***Second order autocorrelation at zero time delay*** $g^{(2)}(0)$ ***as a function of normalised nonlinear coefficient for pulsed excitation.*** *The solid curves show the pulsed regime simulations while the dashed curves show the corresponding CW (steady state) regime simulations using the same experimental parameters for comparison for different cavity-exciton detunings* Δ *(blue* $= -0.5$ *meV, orange* $= 0$ *meV, green* $= 0.4$ *meV and red* $= 1.1$ *meV) moving across* $\Delta = 0$. *Parameters:* $\hbar\gamma_x = 0.062$ *meV,* $\hbar\gamma_c = 0.041$ *meV,* $\hbar\Omega_R = 1.4$ *meV,* $\Delta_{LP}/\gamma = -0.875$, *pulse duration = 35 ps and average incident power* $P = 40$ *pW.*

As was established in Fig 2.14, antibunching values decrease in the pulse case for increasing system nonlinearity (see Fig 2.18). This is expected as the two-polariton transition is shifted to higher energies reducing the overlap of the excitation laser and the two-polariton transition, thus reducing the probability of exciting the higher state.

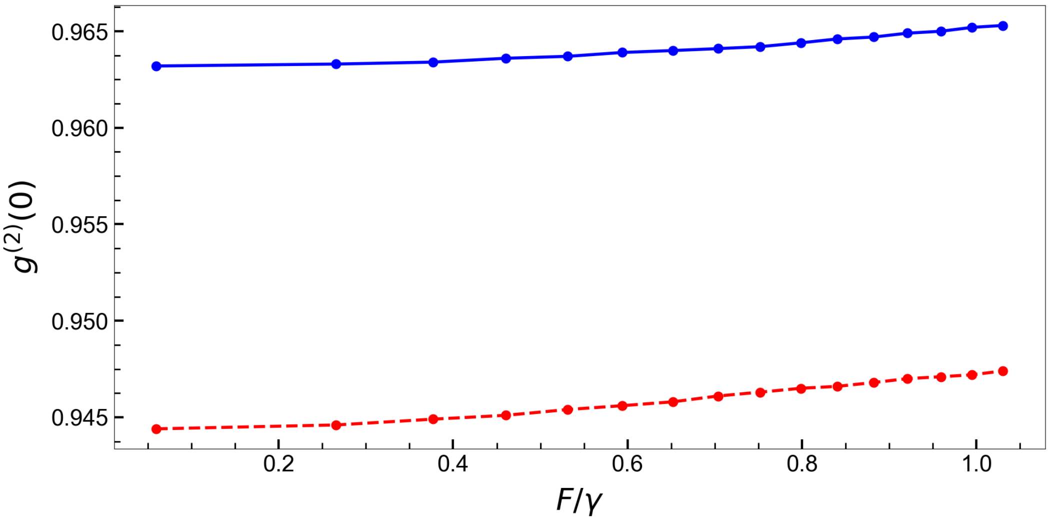

Figure 2.19: ***Second order autocorrelation at zero time delay*** $g^{(2)}(0)$ ***as a function of normalised average incident pump power for pulsed excitation.*** *Parameters:* $\hbar\gamma_x = 0.062$ *meV,* $\hbar\gamma_c = 0.041$ *meV,* $\hbar\Omega_R = 1.4$ *meV,* $\hbar\omega_{nl} = 0.01$ *meV,* $\Delta = 1.1$ *meV,* $\Delta_{LP}/\gamma = -0.875$ *and pulse duration = 35 ps.*

The steady state simulations show a substantial difference in antibunching behaviour, with this difference increasing for more positive Δ's. This is a result of the monochromatic excitation in the steady state scenario which will mean a small energy shift is required before the two-polariton transition is out of resonance with the excitation energy.

In Fig 2.19, the value of $g^{(2)}_{phot}(0)$, while still displaying antibunching, is very weakly dependent on the excitation power. This is even the case with the steady state simulations, albeit at lower values. This is in contrast to what is seen in Fig 2.15 in the same region, although the dependence is still relatively small. However, this power dependence in Fig 2.15 dramatically increases at high excitation powers. To show the comparison between the CW and pulsed cases in Fig 2.19, the normalised average incident power F is used which in the pulsed case is defined as,

$$F = \sqrt{\kappa}\sqrt{N_{avg}} \tag{2.40}$$

where κ is the cavity decay rate and N_{avg} is the average number of photons arriving at the cavity per second.

3

Experimental Methods

This chapter describes the experimental and technical requirements for the results presented in chapter 4. An overview of the entire experimental setup is given in section 3.1 with a detailed description of the fibre cavity microscope. Section 3.2 outlines the fabrication process and analysis of the fibre microcavity mirrors used in the main experiment. This is followed with a cavity mode simulation of the electric field distribution of the microcavity system in Section 3.3. To characterise the polariton system, sections 3.4 and 3.5 present the Photoluminescence spectroscopy and resonant spectroscopy of the microcavity polaritons respectively, and their respective implications. To conclude, section 3.6 discusses a technique developed to improve the zero delay time calibration of a Hanbury-Brown and Twiss interferometer which has been published in [86]. Other parts of this section have been publish in Nature Materials [87] as part of the supplementary information.

To achieve the polariton blockade regime with microcavity polaritons, strong photonic lateral confinement of the polariton wavefunction is prescribed. This requirement necessitates careful engineering of the microcavity design to deliver cavity qualities such as small mode volumes while retaining high cavity Q-factors. In our experiments, we implement a Fabry-Pérot fibre microcavity, to introduce tight, optical confinement of polaritons to study strong polariton-polariton interactions.

A fibre-based microcavity is a semi-integrated cavity which replaces one of the semiconductor mirrors of a planar, QW microcavity with a concave, dielectric mirror recessed into a cleaved fibre tip as illustrated in Fig 3.1. In this thesis, we chose a fibre-based microcavity as the fibre component of the cavity allows lateral confinement of the polariton mode through the geometry of the machined concave indentation. This is accomplished while retaining excellent optical qualities such as high Finesse and Q-factors [50], without incurring significant polariton losses as is generally found in other designs such as micropillars [4] and mesa structures [5]. As the fibre components are independent of the QW substrate, the cavity length, which determines the polariton energy and lifetime, can be tuned over an extended range without largely changing the cavity spot size on the QW sample. Moreover, the concave mirror recess on the fibre tip can be custom machined using CO_2 laser ablation techniques to produce small radius of curvature (RoC) structures necessary to provide small cavity spot

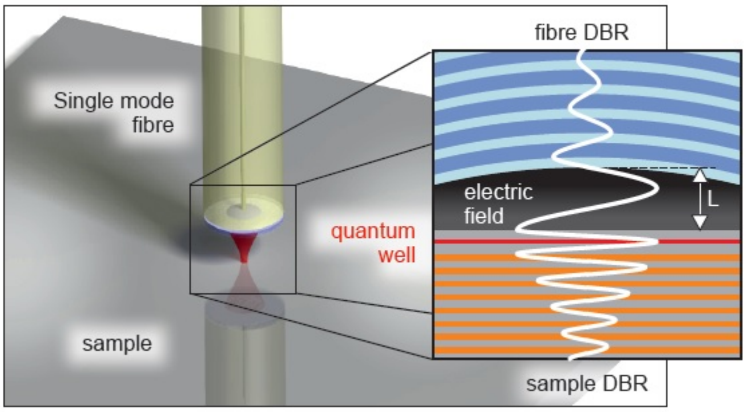

Figure 3.1: ***Fibre-based microcavity system schematic.*** *The SM fibre with mirror (yellow cylinder with mirror on end facet) is brought close to the planar sample to form a microscale optical cavity. The inset image is a cross section of the cavity where the blue layers form the fibre DBR mirror and conforms to the machined concave indentation on the fibre facet. The red layer between the two grey layers is the QW sample which is followed by the alternating grey/orange layers which constitute the other mirror which is grown directly onto the sample. The white curved line is the electric field of the cavity mode. From [8].*

sizes.

In the past, the Fabry-Pérot fibre microcavity was employed to study confined polariton structures [8], however, the optical confinement proved insufficient to reach the regime of polariton blockade. In our setup, we improve upon the work performed in [8] to realise strongly interaction polaritons at the single particle level.

3.1 Experimental Setup - Overview

To perform measurements of the second order correlation function of the light emitted from the microcavity polariton system for signs of antibunched light, we adopted an experimental setup as illustrated in Fig 3.2. To excite the polariton system, we used a MIRA 900D laser from Coherent Inc. (Fig 3.2 (1)) in picosecond pulse mode to create laser pulses resonant to the LP mode with ~6 ps width at a repetition rate of 76.3 MHz. However, due to the slow photon detector response as compared to the polariton lifetime, the ability to collect accurate statistics becomes a significant problem. To improve this situation, a modified resonant laser pulse was used to increase the pulse width approximately to the polariton lifetime (~35 ps) to better match the detector response. To alter the laser pulse width, we used a laser pulse-shaping system (Fig 3.2 (2)) which included an Acton SP2750 spectrometer from Princeton Instruments. A more detailed explanation of the modified laser pulse and its role in this experiment is discussed later in (see section 3.5.3 of this thesis.

To be able to characterise the resonant laser pulse widths and centre wavelength in real-time, an Optronis SC-10 streak camera (Fig 3.2 (3)) and a HighFinesse GmbH WS8-10 wavelength meter (Fig 3.2 (4)) were used respectively.

The fibre cavity microscope with the QW sample (Fig 3.2 (5), see section 3.1.1) was placed in a liquid Helium bath and the sample illuminated with the modified laser pulses, near-resonant to the LP mode.

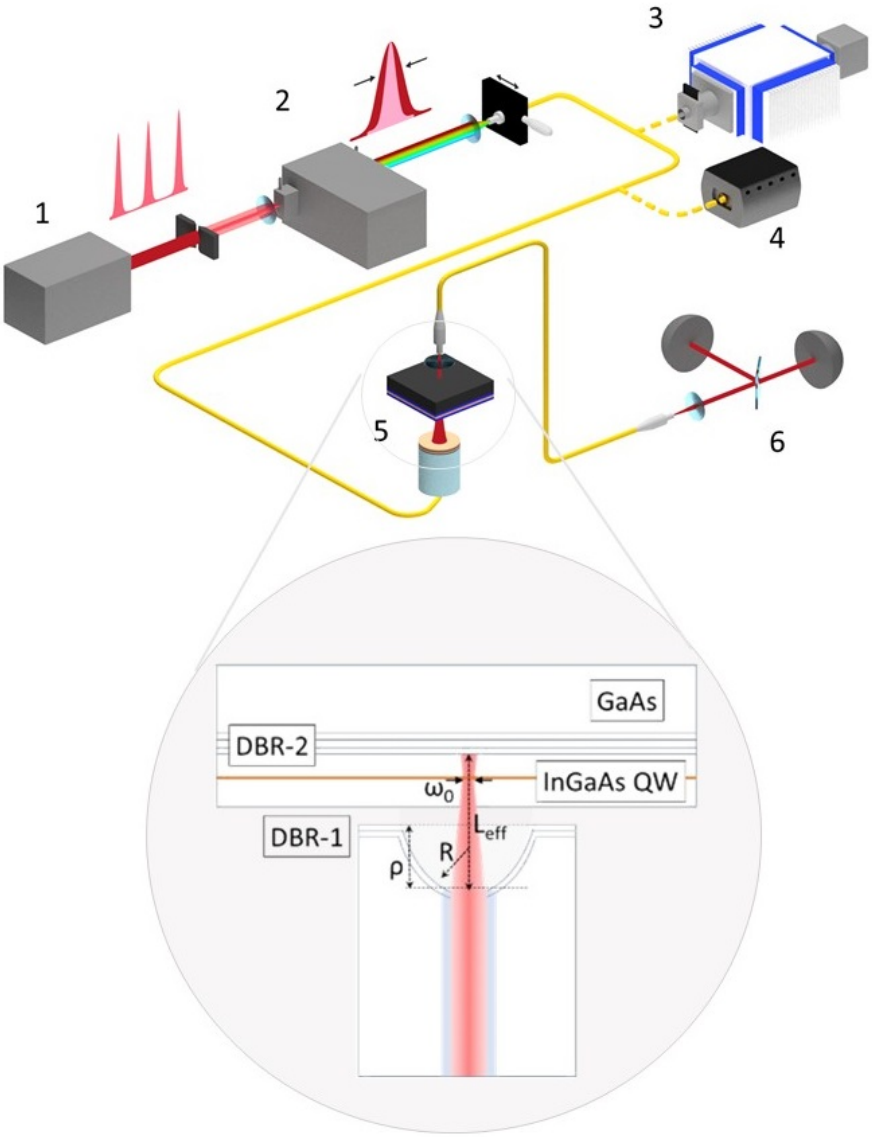

Figure 3.2: ***Microcavity experimental setup.*** *(1) MIRA 900D laser operating in picosecond pulse mode with pulse width duration of 5-6ps at 76.3MHz repetition. (2) Acton SP2750 spectrometer for pulse modification. (3) Optronis SC-10 streak camera for measuring modified pulse widths. (4) High Finesse WS8-10 wavemeter for measuring pulse wavelength. (5) Fibre microcavity inside Liquid Helium dewar (inset) cross-section of fibre microcavity showing sample and fibre mirror structure. (6) Hanbury Brown and Twiss interferometer to measure emitted photon statistics of microcavity polaritons.*

Finally, the transmitted light from the fibre cavity microscope is collected and the photon statistics are measured using a standard Hanbury-Brown and Twiss interferometer (Fig 3.2 (6)). The Avalanche Photo-Diodes (APDs) used are the SPCM-AQR-14 from PerkinElmer Inc. with ≈100 cps dark count rate and ≃40% quantum efficiency at 830 nm. The PicoQuant PicoHarp 300 TCSPC module was used to provide electronic correlation analysis of the APD signals to build a raw histogram of the total photon coincidences.

3.1.1 Fibre Cavity Microscope

At the core of the our system, there are two critical components; the fibre mirror and QW sample substrate (Fig 3.2 (5) inset). The optical fibre we chose for the fibre mirrors are single mode (SM), copper jacketed fibres with an operating range of 800-900 nm with a mode field diameter of 6 μm ± 0.5 μm. These fibres were sourced from IVG Fiber Ltd, Canada. The concave impressions on the fibre facet were machined using CO_2 laser ablation performed with our home-built Fibre Imaging and Machining System (FIMS). The details of this machining process and setup as well as the analysis of the geometries is explained in section 3.2. The RoC at the centre of the concave impression of the fibre mirror used in these experiments was $R = 13\ \mu$m with a depth of 1.3 μm which gave a calculated cavity mode waist of $\omega_0 = 1.16\ \mu$m. The machined fibre is coated with a dielectric DBR consisting of 33 paired layers of Tantalite (Ta_2O_5) and Silicon dioxide (SiO_2) with the centre wavelength of the stopband at 830 nm.

The second crucial component, the QW sample substrate, consists of a molecular beam epitaxy (MBE) grown $Al_{0.95}Ga_{0.05}As$-$Al_{0.1}Ga_{0.9}As$ DBR of 45 paired layers with a single $In_{0.04}Ga_{0.96}As$ QW layer sandwiched by two GaAs layers on top. The exciton wavelength is $\lambda_X \approx 838$ nm.

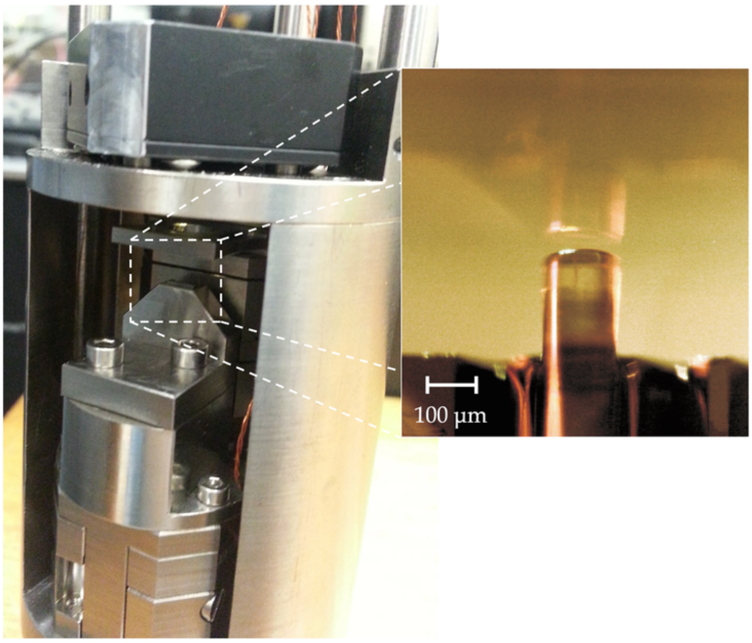

Figure 3.3: ***Fibre microscope configuration.*** *The fibre mirror is glued vertically into a Titanium mounting block (trapezoidal piece) using a Silicon V-groove. This mounting block is situated upon a vertically moving Attocube nanopositioning piezo stage. The sample is glued onto a Titanium holder which can move in the XY plane via two horizontally moving Attocube nanopositioning piezo stages. The inset shows a magnified view of the fibre mirror as it approaches the sample. This mounting setup is placed at the end of an approx. 1.5 m long dipstick which is inserted into an airtight sleeve, establishing a vacuum inside the sleeve, and is then placed into a liquid Helium dewar. Light is collected at the top of the dipstick via a collimating lens (inside black square holder) situated just above the sample.*

Moving out from the fibre mirror and QW sample, these components are mounted on linear, slip-stick, piezo actuated nano-positioning stages with resistive position readout from

Attocube systems AG. These nano-positioning stages from Attocube were chosen as they can be operated at cryogenic temperatures as well as offer position adjustment with sub-nm resolution using the Attocube ANC-300 controller hardware. This fine position adjustment is crucial for precisely controlling the microcavity length, allowing detailed probing of the polariton modes. The sub-nm adjustments can be easily controlled by applying a voltage between 0 - 150 V with a resolution of 0.001 V to give a total travel range of 1.5 μm. For coarse positioning, the slip-stick stepping feature provided a travel range of 5 mm. In the case of our experiment, the fibre mirror tip was mounted facing upwards on a single Attocube ANPz-101 vertical positioning stage via a specially designed, two-piece Titanium mounting block as shown in Fig 3.3.

The fibre is glued to the top block which has a trapezoidal/L-bar shape by way of a silicon V-groove from OzOptics Ltd. The fibre is allowed to protrude approximately the diameter of the fibre ($\sim$125 μm) out from the v-groove and Titanium holder which shown in Fig 3.3 (inset). This has the main benefit of keeping the fibre tip clear of the holder so that it can be brought as close as possible, if not in contact, with the QW sample without interference, thus allowing the shortest cavity possible. This is evident in Fig 3.3 (inset) by mirror image of the fibre tip on the QW sample showing their very close proximity to each other. Clearly, the fibre could be moved even closer to the sample without impedance. Also, by keeping the protrusion length of the fibre tip to this length, the fibre tip remains rigid and does not act like a pendulum, significantly reducing the effects of vibrations on the cavity mode.

The QW sample is glued to a Titanium sample holder so that the sample is facing downwards to the upward facing fibre mirror. The sample holder is directly mounted to two, stacked Attocube ANPx101/RES horizontal positioning stages with travel directions orthogonal to each other. The orthogonal directions of the two stages allow x and y movement of the QW sample relative to the fibre mirror. The fibre mirror and QW sample on their respective nano-positioning stages are housed in a small Titanium cylinder, suspended at the end of a long cryogenic dipstick.

The dipstick is inserted into a sleeve, vacuum pumped to remove air and moisture from the system and then filled with Helium gas to a pressure of 27 mbar for efficient heat exchange with the liquid Helium bath. The dipstick is then placed into a stand-alone, 90 litre liquid Helium dewar which will keep the system at T$\approx$4K for 3-4 weeks. A home-built, sound-proof box along with a vibration-absorbing platform is used to insulate the dewar from the lab environment and to eliminate mechanical and acoustic vibrations, which effect the cavity length stability.

To provide a laser pump input to the cavity, a P3-830A-FC-5 SM fibre from Thorlabs was guided through the top of the dipstick through a Teflon pressure feedthrough and spliced to the free end of the cavity fibre. After the laser light has passed through the microcavity system, the transmitted light from the cavity is then collected through a small, wedge-shaped (to eliminate secondary reflections) window and coupled into a SM optical fibre via a breadboard mounted directly to the top of the dipstick.

3.2 Fabry Pérot Fibre Microcavity Fabrication

The fibre mirror structures used in our experiment were manufactured with a system we developed to machine large numbers of fibres with RoCs as small as 10 μm. At the heart of this system, we use a 10.6 μm, CO_2 laser ablation system equipped with an *in-situ* laser interferometry characterisation capability, ideal for increasing productivity as well as reducing the handling of fibres.

A CO_2 laser system is used in this machining process as 10.6 μm light is readily absorbed within the first few micron of fused silica due to side band absorption from the asymmetrical stretching of the Si-O-Si mode at 9.3 μm. Laser parameters such as beam waist, power and pulse duration, must be carefully chosen and very well controlled to ensure that evaporation of material takes place to create uniform structures. With evaporation of material also comes a smoothing effect due to surface tension which aids in reducing surface roughness, crucial for high finesse mirror surfaces, with achievable root-mean-square (rms) surface roughness reduced down to 0.2 nm [88].

3.2.1 Fibre Imaging and Machining System - FIMS

The layout of the FIMS system is illustrated in Fig 3.4. The FIMS setup is split into two distinct systems which converge on the fibre facet via a miniaturised Michaelson interferometer on a movable nanopositioning stage as shown in Fig 3.5. The first system is the CO_2 laser ablation system used to remove material from the fibre facet to create the concave impressions, while the second system is a laser interferometry imaging system for characterising the concave impressions (see section 3.2.2). The laser ablation system uses the Synrad Firestar v30, water-cooled CO2 laser producing 30 W, horizontally polarised, 10.6 μm laser radiation. As mentioned above, to control the ablation process to create indentations of the desired RoC with low surface roughness, the laser parameter such as power, beam waist and pulse duration must be characterised and finely controlled.

Laser power, is controlled by two coupled, water-cooled, ZnSe coated, Brewster window attenuators supplied by ULO Optics which operate using the Brewster angle principle whereby the transmission of the beam is dependent on the incident polarisation. While the Brewster attenuators perform the role of controlling laser power, they also control the laser polarisation. This is crucial for converting the linear polarisation of the laser beam into circularly polarised light using a $\lambda/4$ reflecting phase retarder plate. Circularly polarised light produces better results, as there is higher absorption and less reflection by the material than linearly polarised light. The two Brewster attenuators thus enable the polarisation of the laser to be rotated to the correct orientation needed for the phase retarder.

The beam waist is controlled through the use of a CO_2 beam expander attached to the end of the Brewster attenuators along with an aberration corrected, aspheric double focusing lens assembly with a short, 24 mm working distance to focus the beam after the expander. The beam expander increases the beam diameter to nearly fill the focusing lens to maximise the benefit of the lens to produce the smallest possible beam waist on the order of the diffraction limit. The aberration free lens also ensures a distortion free laser profile for uniform impressions on the fibre.

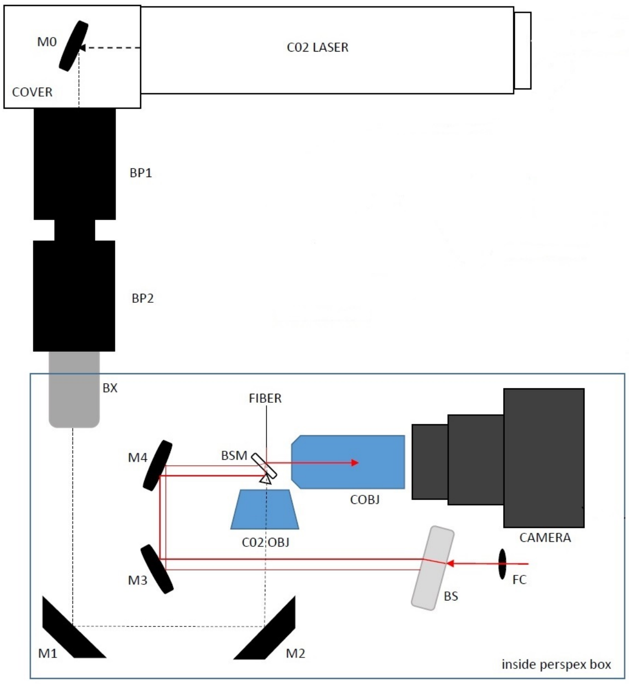

Figure 3.4: ***FIMS experimental setup***. *This system comprises of two subsystems, the* CO_2 *laser ablation system and laser interferometry imaging system. The* CO_2 *laser ablation system starts in the top right corner with the water-cooled Synrad Firestar v30* CO_2 *laser. Following the path of the beam left out of the laser is M0 which is a silicon coated mirror to guide the beam into the Brewster attenuators. The beam passes through BP1 and BP2 which are the Brewster attenuators which control beam power and polarisation. The beam exits BP2 into the beam expander BX which alters the size and position of the beam waist. The beam then reflects from M1 which is a silicon coated mirror onto M2 which is a* $\lambda/4$ *reflecting phase retarder for conversion of linearly polarised light into circularly polarised light. The* CO_2 *beam then passes through* CO_2 *OBJ which is the aberration free focusing double lens for beam focusing onto the fibre, with a working distance of 20.5mm. The laser interferometry imaging system starts in the lower right corner with a HeNe laser (632.8 nm) coupled into the system with the fibre coupler, FC, which incorporates a focal screw and polariser for maximum interference contrast. The beam then impinges on the large fused silica beamsplitter, BS, used to create the two arms of the interferometer. The split beams are reflected onto the silver mirrors M3 then M4. The beams travel towards the beamsplitter/mirror combination. The beams are collected by COBJ which is a Mitotuyo microscope objective with a 50x magnification. Finally, the camera is a DSLR Cannon CCD camera for image capture of the fibre facet.*

Finally, the pulse duration is controlled by the application of voltage to the laser RF controller which directly stimulates the CO2 gases. A digital signal generator generates a single square wave pulse of set duration to the laser via the RF controller. Pulse durations as small as 100 μs could be measured. With pulse duration, power, and beam waist control, indentation characteristics such as ROC and depth can be altered to meet desired applications; in our case, the smallest possible RoC.

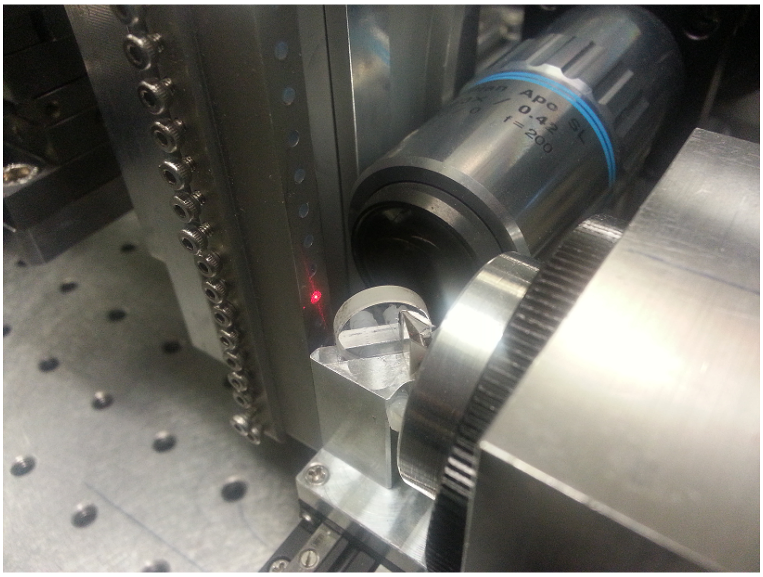

Figure 3.5: ***Movable Michaelson interferometer for fibre characterisation.*** *The beamsplitter along with a mirror is placed on a linear nanopositioning stage to allow the interferometer to be moved out of the CO_2 laser beam path for ablation. The stage can then be precisely returned to its original position infront of the fibre to image the fibre indentations for characterisation.*

3.2.2 Fibre Indentation Analysis

As an integral part of the FIMS, a laser interferometry imaging system provided an *in-situ* ability to characterise the fibre impressions. This imaging system was integrated by miniaturising a Michaelson inteferometer by placing a beamsplitter and mirror on a nanopositioning stage (see Fig 3.5), which could be moved out the incident CO_2 beam path when laser ablation was taking place. After the laser ablation, the nanopositioning stage could be precisely returned to its initial position from which an interferometric image of the fibre facet could be taken, an example of which is shown in Fig 3.6. With this image of the fibre facet, a pixel analysis could be performed to extract the laser ablated impression dimensions, such as radius of curvature (RoC) and depth.

The pixel analysis of the interfermetric image was carried out using a custom Python programme using the Python Imaging Library know as pillow or PIL module for image importation, Pyqtgraph module for the GUI and ROI selection of the image, PeakUtils module for finding local maxima and minima values of the pixel intensity in the ROI selection, and finally, the Lmfit module for the Gaussian laser profile fitting of the impression profile.

With the interferometric image of the fibre facet loaded into the Python program, a pixel scale conversion was performed by placing and adjusting a large circular ROI selection area that corresponded to the circumference of the fibre tip. The diameter of the fibre (125 μm) could be divided by the diameter of the circular ROI given in number of pixels to give a pixel scale which is applied to the fitted Gaussian laser profile. Next a rectangular ROI box can be placed over the indentation site as shown in Fig 3.6.

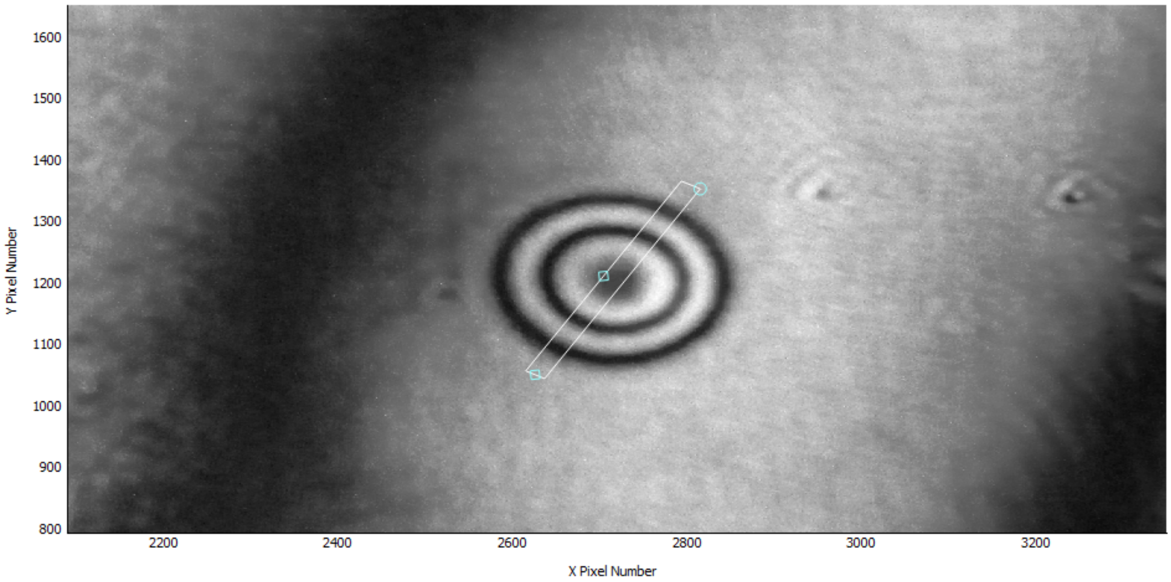

Figure 3.6: ***Interferometric fibre image with ROI selection box.*** *A thin rectangular ROI box is placed over the fringes produced by the indentation. Note the how the ROI box is parallel to the large fringes on the flat part of the fibre facet.*

It was found that rotating the ROI box to approximately parallel the large fringes on the flat parts of the fibre removed unwanted fringes from consideration by the programme. While the position and the sizing of the ROI box is taking place, a real-time graph of the pixel intensity is displayed (see Fig 3.7) showing the maxima and minima values of the pixel intensity, which greatly assists in ensuring the entire profile is captured.

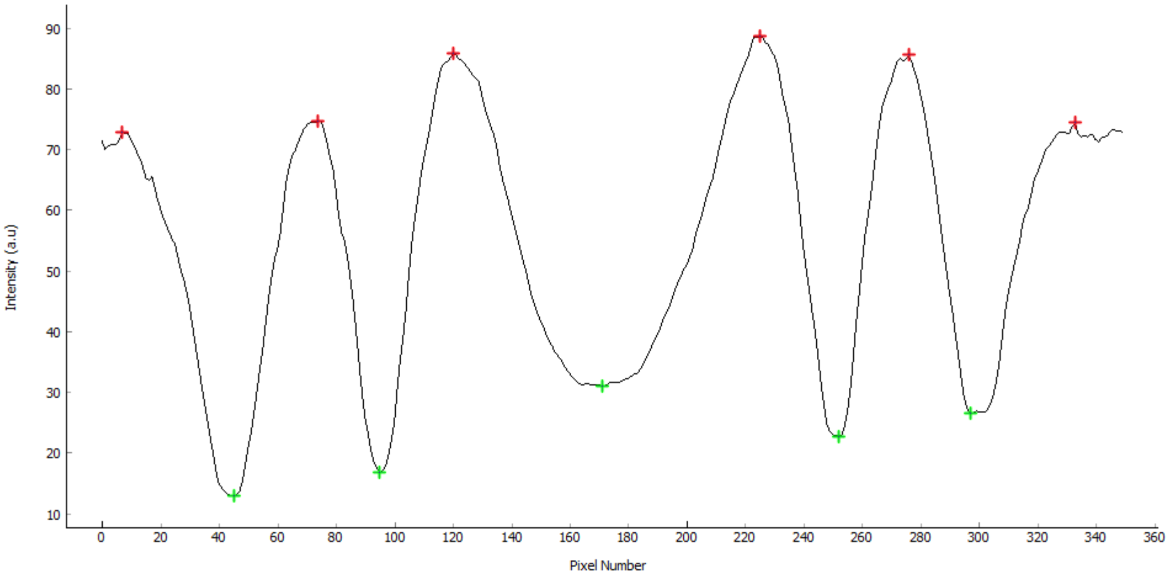

Figure 3.7: ***Pixel intensity graph of the interference fringes.*** *The maxima and minima of the pixel intensity values correspond directly to the respective interference fringes. The red and green crosses indicate to the user where the programme has found the position of bright (red) and dark (green) fringes to be.*

Using this pixel intensity graph, the user can visually determine if the programme has detected the fringes correctly. If this is not the case, the user can increase the width of the ROI to increase the number of pixel rows over which it can average to attain a smoother profile, thus making it easier for the programme to detect the peaks. A smoothing algorithm is also built into the programme and can be increased in strength to again smooth the profile. For the most accurate simulation of the profile, the ROI width and smoothing algorithm use should be kept to a minimum, however, image quality sometimes necessitates that these methods be used.

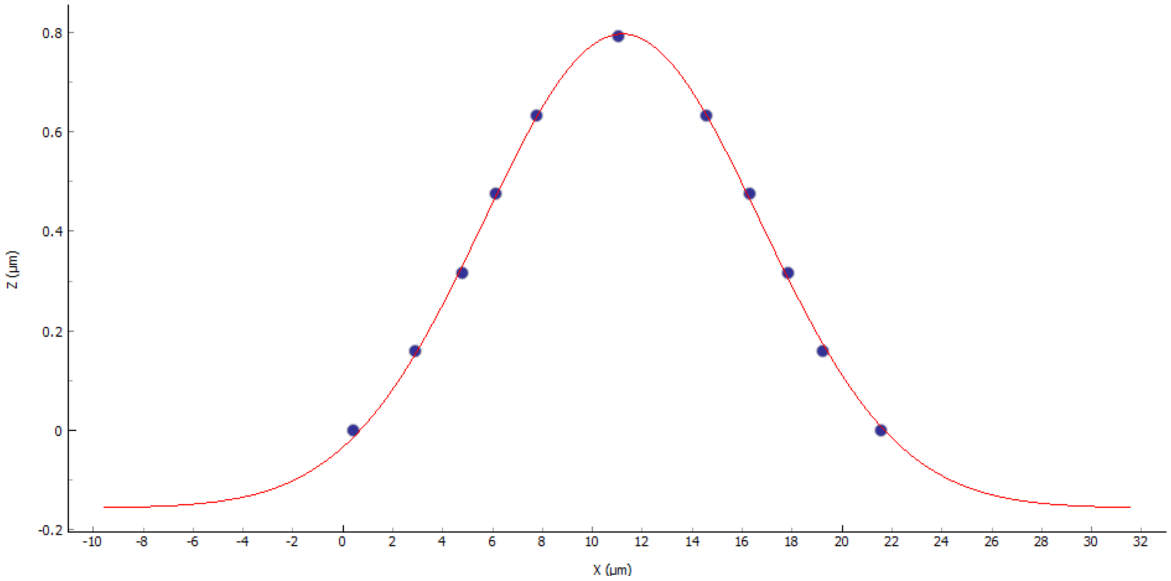

Figure 3.8: ***Fitted indentation profile.*** *The extracted indentation profile (blue circles) is fitted with a Gaussian function (red curve). At the centre of the Gaussian, RoC variation is small and can be approximated to be spherical in this region, allowing an RoC value to be given to this structure.*

With the correct positioning and sizing of the ROI box, and the correct selection of the maxima and minima fringes, the programme now has an array of pixel positions spanning the width of the concave indentation. The programme then produces a second array of the depth of each of the points based on the $\lambda/4$ (λ = wavelength of light) spacing between successive maxima and minima fringes. It should be noted a spacing $\lambda/4$ is used rather than a $\lambda/2$ spacing because the total optical path length is twice the distance between the fibre facet and the beamsplitter in our setup. The data is then fitted with a Gaussian function as shown by the red curve in Fig 3.8 as the ablated structures, to a good approximation, are near Gaussian in shape due to the laser mode profile [89]. The user can then determine the validity of the fitting and if needed, restart the entire process over. From the fitted Gaussian function and since the RoC variation at the centre of the Gaussian profile is small, a spherical approximation can be used to give an RoC for the mirror given by:

$$R = \frac{\sigma}{A} \tag{3.1}$$

where σ is the standard deviation and A is the depth of the structure. The results of the RoC and the depth fitting values are given in pixels as we have only worked in these units. These values can now be multiplied by the pixel scale found at the outset to give values in μm.

With this analysis programme, the RoC of the fibre mirrors can be ascertained within an error of ±2 μm and the depth within ±0.2 μm. However, the image quality could, in some cases, interfere with making reliable estimations.

3.3 Cavity Mode Simulation with InGaAs Quantum Well Sample

The cavity mode simulations in this section were performed by Gilles Nogues of the University of Grenoble Alpes, CNRS, Grenoble INP and Institut Néel, Grenoble, France in collaboration for the Nature Materials paper [87] published on this research.

The cavity mode is of great importance in these experiments as its shape directly affects the dynamics of the polariton system. The goal with the fibre mirror used in the experiments presented in this thesis was to have the smallest possible RoC impression to produce the smallest cavity mode waist, and hence mode volume, to maximise polariton interactions. Since we could not directly measure the mode waist and directly calculate the lowest transverse cavity and hence polariton mode shape, we used the physical parameters of the fibre mirror, mirror coatings and QW sample to perform numerical simulations of Maxwell's equations, using the finite element software COM-SOL.

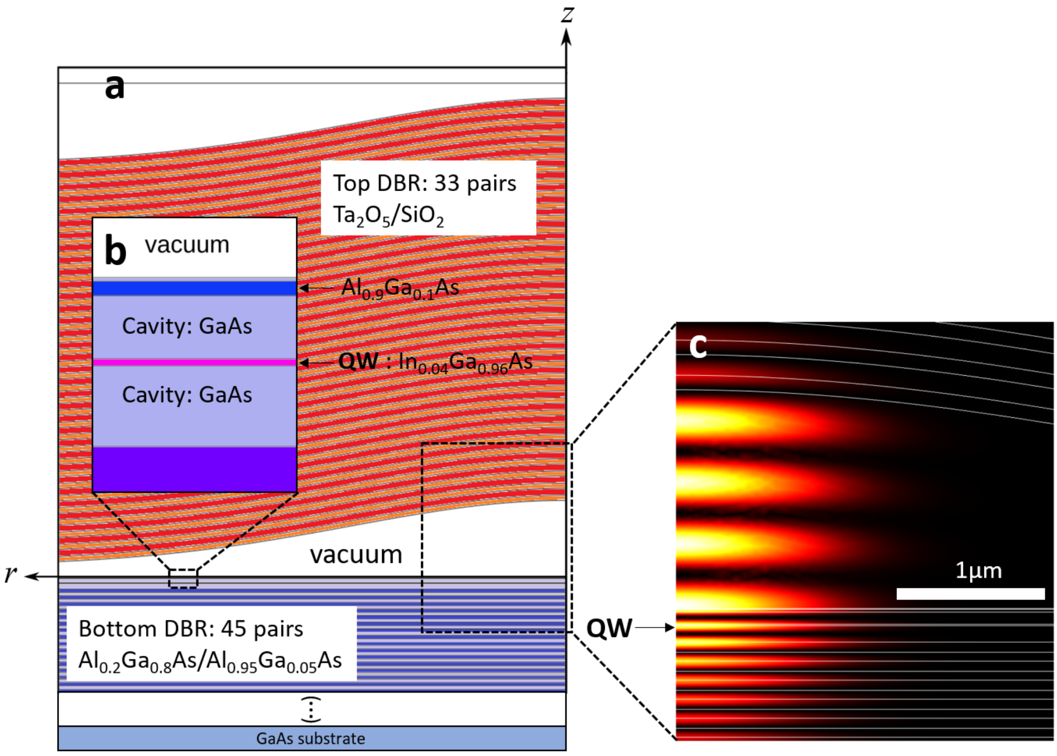

Figure 3.9: ***Cavity mode simulation.*** ***(a)*** *Schematic cross-section of microcavity with experimental parameters and sample.* ***(b)*** *Exploded view of the QW sample layer composition.* ***(c)*** *Simulation of the electric field of the cavity mode. The bright parts are places of large electric field intensity.*

To begin, we assumed a circular symmetry around the axis z of the optical fiber. Taking into account the expected symmetries of the mode, the calculation is carried out in the r, z

plane, with $r \geq 0$, and only for the in-plane components of the electric field $\mathbf{E} = (E_r, E_z)$. The simulation's geometry is shown in Fig 3.9 (a). The origin of the r, z space is taken at the interface between the MBE grown sample and the vacuum. Calculations are limited to the space defined by $0 \leq r \leq r_{\max}$ and $-z_{\min} \leq z \leq z_{\max}$, with $r_{\max}$ =10 μm and $z_{\min}$ and $z_{\max}$ large enough so as to fully encompass the bottom and top DBR reflectors and a small portion of GaAs substrate and SiO_2 fiber. Before the top and bottom boundaries, a 300 nm-thick, perfectly matched layer is used in order to absorb any outgoing wave without reflection. As a consequence, one assumes a boundary condition $E = 0$ for $r = r_{\max}$, $z = z_{\max}$ and $z = -z_{\min}$. On the z axis, one assumes $E_z = 0$ (perfect electric conductor).

For the fiber DBR, we assumed that the coating is made of successive layers deposited by a directional method. As a consequence, each interface is a replica of the initial profile etched on the fiber. The etched profile is measured to be of Gaussian form, which is what we use in the simulation; the interface between the final dielectric layer and the vacuum is taken as:

$$h(r) = h_{\text{fiber}} + \rho \times e^{-\dfrac{r^2}{2w_m^2}}.$$

Interferometric measurements of the fiber profile yield $\rho = 1.3\,\mu$m and a radius of curvature $R \simeq 13\,\mu$m at $r = 0$. Thus one has $w_m = \sqrt{\rho \times R} = 4.11\,\mu$m. The low temperature refraction indices for $Al_xGa_{1-x}As$, Ta_2O_5 and SiO_2 are taken from Refs. [90, 91] and [92] respectively. The QW background index of refraction is assumed to be that of GaAs. This assumption has a negligible influence on the mode shape in real space.

The software searches for field eigenmodes of the form $\mathbf{E} = \hat{\mathbf{E}}\,(\mathbf{r}, \mathbf{z})\mathbf{e}^{-\mathbf{i}\omega_c \mathbf{t}}$ for the above described structure where ω_c is in the vicinity of $\omega_X = E_X/\hbar$. The calculated eigenfrequencies ω_c are complex numbers whose imaginary part reflects the losses of the corresponding mode. A fundamental transverse mode is found with $\omega_c \simeq \omega_X$ for $h_{\text{fiber}} = 205$ nm in good agreement with the experiments. Its Q factor ~ 30000, which is limited by the absorption in the Ta_2O_5 layers and its value, would be closer to the experimental value if one considers the absorption in the GaAs layers. Fig 3.9 (c) shows a 2D-map of its intensity distribution $I(r, z)$ in the region of interest. As expected, it presents an antinode at the QW layer (arrow). The intensity $I(z = z_{\text{QW}}, r)$ agrees with a Gaussian function $I_0 e^{-2r^2/\omega_0^2}$ over several orders of magnitude, with $\omega_0 = 1.17\,\mu$m.

3.4 Photoluminescence Spectroscopy

3.4.1 Photoluminescence of Microcavity Polaritons

Characterisation of the polariton modes is performed by recording the photoluminescence (PL) spectra of the microcavity emissions while changing the cavity length, hence, cavity-exciton detuning under non-resonant, CW laser excitation. In the experiment, the cavity length was precisely controlled by moving the fibre mirror closer to/further away from the QW sample by way of an Attocube ANPz-101 piezo nanopositioning stage. The sub-nm movement of the fibre mirror and hence cavity length allows a high resolution 'scan' of the microcavity system as the energy of the fundamental mode of the cavity is swept across the excitonic transition. The spectra are capture using a Princeton Instruments, Acton SP2750 spectrometer with a 1500 grooves/mm reflective holographic grating and PIXIS 100F, 1340x100 pixel CCD camera.

In Fig 3.10, the PL map for the polariton states is shown where the system is excited with a 798 nm CW laser (E_L = 1.55 eV) at approximately 1 mW incident power. The polariton modes are manually fitted using a coupled harmonic oscillator model with a characteristic anti-crossing observed at resonance between the cavity and exciton and a vacuum Rabi splitting of $2\hbar\Omega_R = 2.8$ meV. The bare exciton transition (X^0) is at 1480 meV.

The pump laser was also tuned to 825 nm (E_L = 1.50 eV) to move the pump laser away from the GaAs absorption edge (see section 3.4.2). Fig 3.11 shows the PL map for this laser pump wavelength.

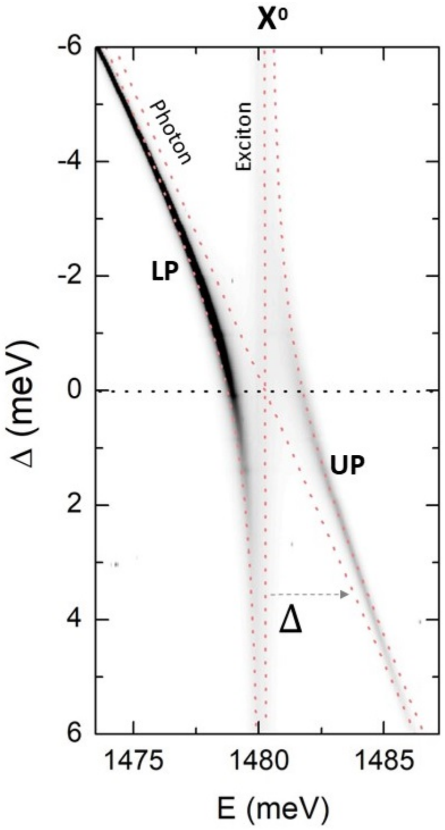

Figure 3.10: ***Photoluminescence (PL) under non-resonant excitation at 798 nm.*** *The signature of the strong coupling regime, the classic avoided crossing with the two polariton mode branches. Vacuum Rabi splitting* $2\hbar\Omega_R = 2.8$ *meV. The red dotted lines show the manual fitting of the polariton modes with the respective exciton transition and photon/cavity mode.* Δ *is the detuning between the photon and exciton resonant frequencies such that* $\Delta = \omega_C - \omega_X$.

While the bare exciton transition at 1480 meV is evident, there is second emission peak 1.2 meV red-detuned from the bare exciton which is weakly coupled to the cavity mode. A similar feature has been reported before in fibre based cavity experiments [93], and owing to its spectral characteristics, we attribute this feature with the negative trion state (X^{-1}) [94]. This statement is consistent with the fact that optical excitation of ionized carbon acceptors in GaAs occurs around 1.496 eV (828.7nm), providing free electrons to the QW that enable the direct excitation of the trion state [95]. Therefore, if the system is pumped at energies approaching 1.496 eV, more free electrons from the ionized carbon acceptors are created, leading to greater emission from the trion state. The presence of this trion state will be crucial for understanding any results of our correlation measurements, as this state is an energy-dependent source of loss and decoherence for polaritons, which is explained in chapter 4.

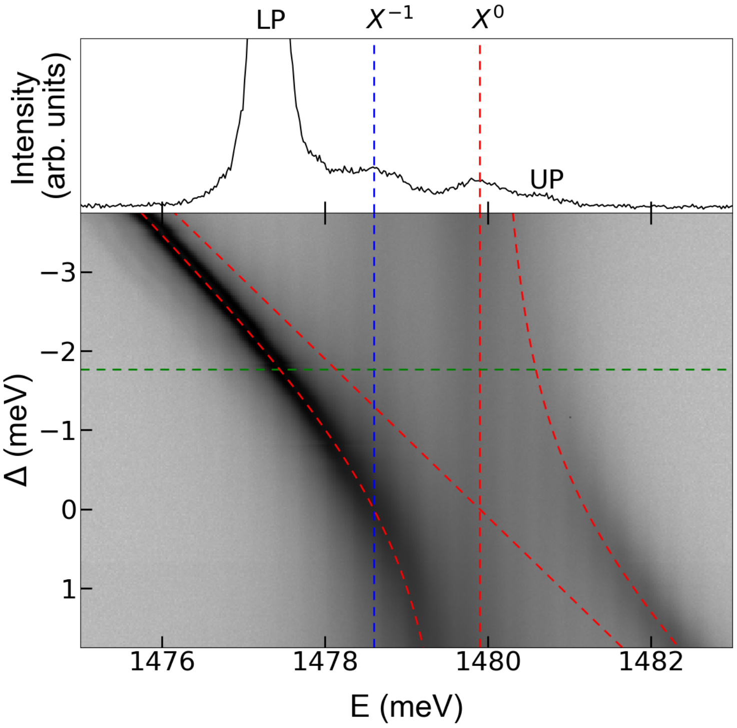

Figure 3.11: ***Photoluminescence (PL) under non-resonant excitation at 825 nm.*** *The black anti-crossing lines are the upper and lower polariton modes. The red and blue vertical dotted lines show the neutral exciton (X^0) and negative trion (X^{-1}) states. The top spectrum is a slice in this map, taken for a slightly negative detuning, shown by the red solid line. The X^{-1} state is found ~1.2 meV red detuned from the neutral exciton state.*

3.4.2 Photoluminescence through Excitation

Preliminary PL mapping of the polariton system was taken under CW laser excitation at 825 nm to avoid absorption in the GaAs while maintaining distance from the bare exciton transition. However, at this excitation wavelength, the X^{-1} trion state is populated due to the availability of free electrons in the QW. While the presence of the trion state is interesting to observe (as the presence of this state in this system is unexpected), this would have serious repercussions for non-resonant measurements of the system as the trion state is a source for losses and thus affects system dynamics. Therefore, photoluminescence spectroscopy through excitation (PLE) measurements were performed to observe the lower polariton emission dependence on the excitation wavelength in an effort to identify the internal sample carrier dynamics and search for an excitation condition which does not populate the trion state.

The PLE measurements were conducted using a computer-controlled, SolsTiS 3000 SRX, Ti:Sapph, CW laser with wavemeter connectivity and tuned in 0.5 nm increments, over a wavelength range of 780-830 nm. Ideally for this measurement, power stabilisation would be used to normalise the measured spectra. However, the power drop without stabilisation is smooth and constant within this region with only a few percent difference between maximum and minimum power values. Therefore, a constant drop can be applied locally to this wavelength range and so no power stabilisation is used for this measurement. The cavity was kept at a constant length at a near resonance with the bare exciton transition. The spectra at each wavelength was recorded on a Princeton instruments Acton SP2750 spectrometer. The PLE results are displayed in Fig 3.12.

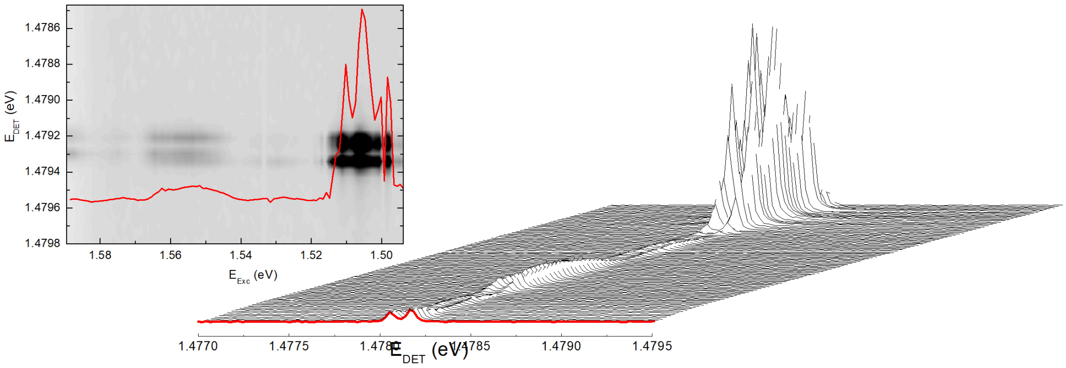

Figure 3.12: ***Photoluminescence through Excitation (PLE) of the LP mode.*** *The main graph shows individual spectra taken at increasing laser excitation wavelengths (front to back). The inset graph shows the same graph as a 2D intensity graph. The two 'windows' of emission at 1.557 eV and 1.506 eV are evident with a considerable difference in emitted intensity due to the GaAs absorption edge at 1.589 eV. Note the two peaks present are most likely due to birefringence in the GaAs.*

Clearly from Fig 3.12, there are two distinct 'windows' of emission from the lower polariton, one centred around 1.557 eV and the other around 1.506 eV. There is also a considerable difference in intensity of emission, mostly likely due to the 1.557 eV window being located close to the GaAs absorption edge. Due to a breaking of the circular symmetry of the system which can be mainly attributed to the birefringence of GaAs, the fundamental transverse mode of the cavity is split into two linearly cross-polarised modes, which is why two peaks are present in the polariton transmission. Note the slight blueshift in the lower polariton resonance is most likely due to the small laser power increase as the laser nears its peak wavelength emission.

With a second excitation window available, PL mapping at 1.553 eV yielded classic polariton modes without the presence of the trion state and so this wavelength was used for all subsequent PL mapping measurements. While it is beneficial to remove the trion presence for these PL measurements, the low signal intensity creates problems with low power, non-resonant excitation of the system for photon correlation measurements. This is due to the low excitation regime the system as to not saturate the polariton transition to achieve nonlinear behaviour at the few particle level, as well as the ability of the APD detectors to register such a low photon flux emitted from the cavity.

3.5 Resonant Transmission of Microcavity Polaritons

In the PL and PLE measurements of the polariton transition, the presence of the X^{-1} trion state as well as polarisation splitting of the polariton modes is shown. These features raise questions as to their impact to the system dynamics which could introduce additional sources for losses as well as add an uncorrelated optical signals to the photon correlation measurement. In order to characterise these features, resonant transmission measurements of the LP lineshape and lifetimes are taken. The resonant nature of these measurement excludes the influence of any carrier relaxation processes, leaving the bare LP mode unperturbed. These measurements are also necessary for experimental considerations as they will enable an accurate map of the laser parameters needed for photon correlations.

3.5.1 Resonant Laser Spectroscopy - Polariton Lineshape

Having chosen the detunings to best probe the LP mode for signatures of quantum correlations, resonant laser spectroscopy of the LP polariton resonance was performed at each detuning. This measurement was carried out by sweeping the wavelength of a CW, wavelength stabilised, M-Squared SolsTIS 3000 SRX laser across the LP resonance at a fixed cavity length and the average transmission recorded on a SPCM-AQRH-14 APD from Excelitas. The transmission intensity is normalised to the input power. With the ability to lock the wavelength of the laser reliably to ±1 pm, a higher resolution spectra of the LP resonance can be observed more than can be afforded by using the spectrometer on hand which has a resolution of 25 pm. Fig 3.13 displays the resonant spectra for $\Delta = 0.07, 0.52, 0.83, 1.05$ meV.

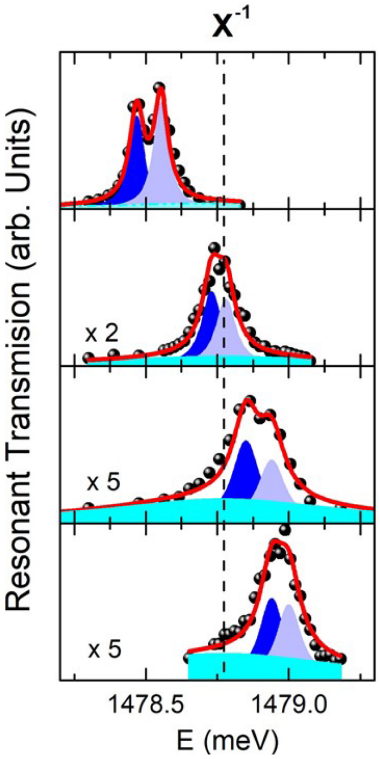

Figure 3.13: ***Resonant laser scans of the LP mode.*** *Each graph shows the LP lineshape as the detuning is swept across from negative to positive (top to bottom). Due to birefringence, the LP mode is polarisation split which is indicated by the double Lorentzian fit (dark blue and grey). The third broad Lorentzian fit (light blue) is added to demonstrate the contribution from the* X^{-1} *trion state. The red line shows the total fit of all these contributions to the the data (black dots). Since the LP intensity decreases for more positive detunings, some of the graphs have been magnified to show the relevant detail denoted by the x2 and x5.*

In all four traces, the LP resonance exhibits a double-peak structure which correspond to the two polarization-split polariton modes π_X and π_Y shown by the double Lorentzian fitting. The splitting of these polarisation modes is of the order of 0.09 meV and decreases for increasing Δ as it is of photonic origin. Note that in this energy range, the linewidth of both LP modes increases from $\simeq$ 0.06 meV to $\simeq$ 0.11 meV as the detuning gets more positive and the low energy tail of the neutral exciton density of states starts to perturb these modes. A third broad and shallow Lorentzian peak (light blue) is added to the fit which reflects the presence of the X^{-1} trion state and shows the increasing contribution of this state as the detuning increases. The increasing trion contribution strongly increases the loss in photon number which makes the choice of experimental parameters crucial for reliable correlation measurements.

3.5.2 Resonant Polariton Lifetime

To complete the characterisation of the system and quantify the trion state impact on the system, lifetime measurements of the LP mode are taken at several cavity-exciton detunings. These measurements use the ring-down spectroscopy technique whereby a pulsed laser source resonantly excites the system. During the periods of no excitation, the polaritons eventually recombines (decays), leaking light out of the system which is exponential in time. This light is collected by an APD which bins the arrival time of the photons. For this type of measurement to work properly, laser excitation parameters must be chosen in advance such that the pulse width is shorter than the expected system lifetime and the period between pulses (repetition rate) is significantly longer than the expected system lifetime. This ensures that the laser illumination diminishes rapidly leaving the system to decay naturally as well as giving enough time for the system to completely decay. In our measurements, we use a MIRA 900 pulsed laser with a pulse width of 3-5 ps and a 76.3 MHz repetition rate which corresponds to a ~13 ns gap between pulses. The emitted photons are recorded on a streak camera from OptoScope from Optronis GmbH with 2 ps time resolution.

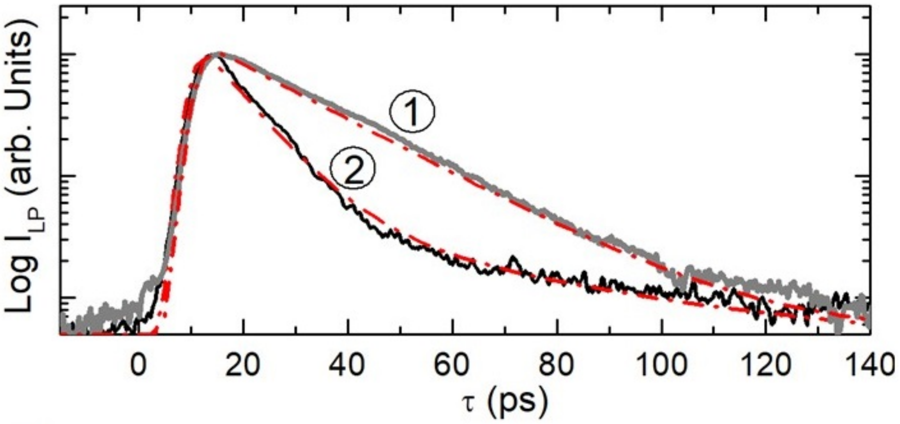

Figure 3.14: ***Trion contribution to LP lifetime.*** *Resonant lifetime traces of the LP mode at two different detunings. Trace ① shows a monoexponential decay for detunings far red detuned from the trion resonance. Trace ② shows a biexponential decay near the trion resonance, where a second fast decay is introduced by the loss mechanism mediated by the trion state.*

When the LP mode is far red detuned with respect to the trion resonance, the polariton decay is monoexponential in time, which is shown in trace ① of Fig 3.14. This behaviour is consistent with the bare cavity lifetime and excitonic fraction at this detuning. To remain consistent, it is expected that the LP lifetime will increase as the detuning is swept across $\Delta = 0$, as is shown by the dotted black line in Fig 3.15. However, this behaviour is only observed to $\Delta \approx 1$ where the lifetime starts to decrease rapidly as the detuning approaches the trion resonance at $\Delta \approx 0.6$ meV, as shown in Fig 3.15. This early departure from the expected trend is attributed to an additional loss channel to the system brought on by the trion state, exceeding the cavity loss channel by nearly a factor of 2 at the trion resonance [96]. This additional trion loss channel modifies the LP decay, becoming biexponential in nature, which can be seen in trace ② of Fig 3.14. This differs from that observed Fig 3.11 where the trion state and the nearby carbon acceptors are both excited directly from the resonant laser rather than indirectly by way of free electrons from ionized carbon acceptors under non-resonant excitation.

The fast part of the biexponential decay curve corresponds to the LP effective decay with $\tau_{LP} = 8$ ps which includes both the cavity decay and irreversible loss into the large trionic density of states. The slowly decaying exponential tail of the LP mode arises from re-emission of the trion state into the polariton mode with a characteristic time of $\tau_X \approx 65$ ps.

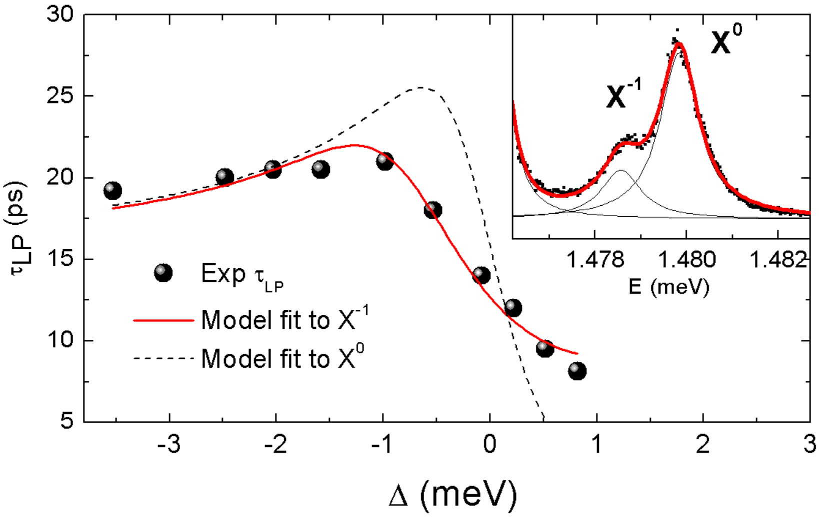

Figure 3.15: ***Resonant LP lifetimes as a function of detuning.*** *The lifetimes are fitted to the neutral exciton X^0 (black dotted line) and trion X^{-1} (red solid line) decay rates, indicating a large contribution from the trion state. Inset: Spectra of the LP mode showing the presence of the X^{-1} state red detuned from the neutral exciton.*

To support this claim of a large, trion mediated loss channel, we model the LP decay time, τ_{LP}, as the sum of two energy dependent contributions, thus:

$$\frac{1}{\tau_{LP}\left(E_{LP}\right)} = \frac{1 - \left|C_X\left(E_{LP}\right)\right|^2}{\tau_C} + \left|C_X\left(E_{LP}\right)\right|^2 \gamma_T\left(E_{LP}\right) \tag{3.2}$$

where $C_X\left(E_{LP}\right)$ is the excitonic Hopfield coefficient and τ_C is the bare cavity lifetime. While the first term describes the polariton loss through the cavity mirrors, the second term, $\gamma_T\left(E_{LP}\right)$, describes the irreversible polariton loss from elastic scattering into the trion density of states at the polariton energy E_{LP}. For simplicity, we assume a Gaussian shape for γ_T such that:

$$\gamma_T = S \exp\left(-\frac{(E_{LP} - E_X - E_B)^2}{2\sigma_T^2}\right) \tag{3.3}$$

where S is the scattering rate, $E_X - E_B$ is the trion transition energy defined as the neutral exciton minus the binding energy and σ_T is the trion linewidth. Substituting the relevant system parameters into Eqn (3.3) and leaving S as a free parameter, we see good agreement with this model given by the solid red line in Fig 3.15 with $S = 0.134$ ps^{-1}.

The identification and modeling of this additional trion loss channel in the system compels the creation of an effective excitonic lifetime given as:

$$\frac{1}{\tau_X^{eff}} = \tau_T. \tag{3.4}$$

Here we identify $\gamma_X = \gamma_T$ which encapsulates all excitonic sources of loss which can be implemented as part of the master equation model described in chapter 3, to fit to experimental data.

3.5.3 Modified Resonant Laser Pulses for Photon Correlations

In order to measure photon statistics of the emitted photon stream from our microcavity system, we used the widely accepted Hanbury-Brown and Twiss (HBT) interferometry technique [97] (see section 3.6). This technique relies on two avalanche photo-diode (APD) detectors to sample the emitted photon stream, creating a correlated signal between the two detectors. While this HBT technique is highly accurate and robust due to the excellent time resolution of current APDs, if the dynamics of the experimental system occur at a timescale comparable or faster than the detector response time, the ‘physics’ is occurring faster than our detectors can observe. This poses a significant issue for collecting accurate correlation information. In the case of a microcavity polariton system, polariton lifetimes range up to only a few 10’s of picoseconds which presents a problem even for the best APD based HBT systems with overall time resolution of $\sim$ 65ps. In an effort to overcome this technical limitation in our system, we elected to use pulsed laser excitation with a modified pulse width which approximately matches or is longer than the polariton lifetime.

Modification of the pulse width has a two-fold benefit; firstly, the larger pulse width more closely matches the HBT system time response, improving the quality of the measurement. Secondly, the effectiveness of the blockade effect is increased as the spectral bandwidth of the pulse now shrinks below the nonlinear energy shift imparted by polariton interactions, reducing the possibility of exciting the two-polariton state. In fact, a larger pulse duration than the lifetime is of even greater benefit, as shown in Fig 3.16, as the larger pulse width moves the peak $g^{(2)}(0)$ antibunching into the region where there is better signal (i.e. more counts due to being near resonance), enhancing the signal to noise ratio of the measurement. The first benefit, however, became irrelevant for our measurements as the low quantum efficiency of the APDs we hoped to use did not provide sufficient count rates at very low pump powers (<100 pw), which necessitated using higher QE APDs at the cost of a considerably lower time resolution.

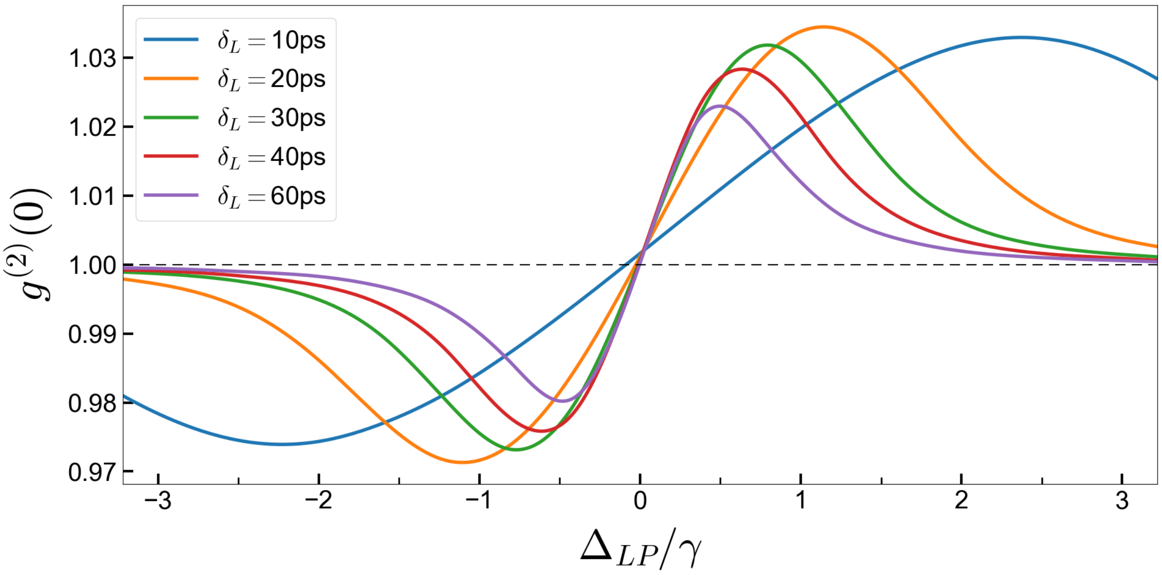

Figure 3.16: ***Effect of excitation pulse width on*** $g^{(2)}(0)$**.** *Simulations of* $g^{(2)}(0)$ *as a function of* Δ_{LP} *for different pulse widths. Simulation parameters:* Δ *=1.1 meV,* τ_{LP} *=7.8 ps,* ω_{nl} *=0.01 meV.*

The modified laser pulses are initially produced from a MIRA 900, Ti:sapphire laser source with the centre wavelength matched to the wavelength under investigation. In Fig 3.17, the unmodified pulsed laser beam is passed through a Acton SP2750 grating spectrometer from Princeton Instruments with the entrance slit fully open, spatially expanding the spectral

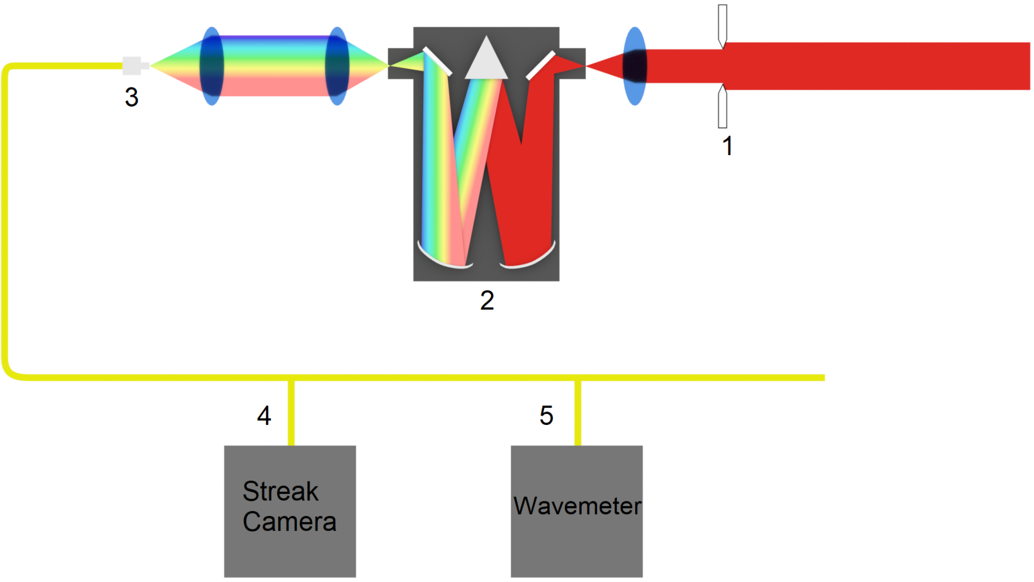

Figure 3.17: ***Pulse modification setup.*** *A variable diameter iris alters the effective NA of incoming pulsed laser beam (1) which enters a grating spectrometer (2), spatially expanding the frequency components of the pulse. The output from the spectrometer is coupled into a fibre (4) which acts as pinhole for spectral filtering. The modified pulse is measured for both pulse duration and centre wavelength using a streak camera (5) and a wavemeter (6).*

components of the laser pulses. The grating is positioned to be centre on the centre wavelength of the input beam. The spatially expanded pulse exits the spectrometer, again with the exit slit fully open, where the beam is guided and coupled into a single mode optical fibre (Thorlabs P3-830A-FC-5). The optical fibre acts as a pinhole, spectrally filtering the pulse. To gain the ability to vary the pulse width of the beam, we place a variable iris just before the entrance to the spectrometer. Placing an iris here allows us to change the effective numerical aperture (NA) of the beam entering the spectrometer. This will change the effectiveness of the grating inside the spectrometer as the beam covers different amounts of the grating, translating into a beam which has different spatial sizes.

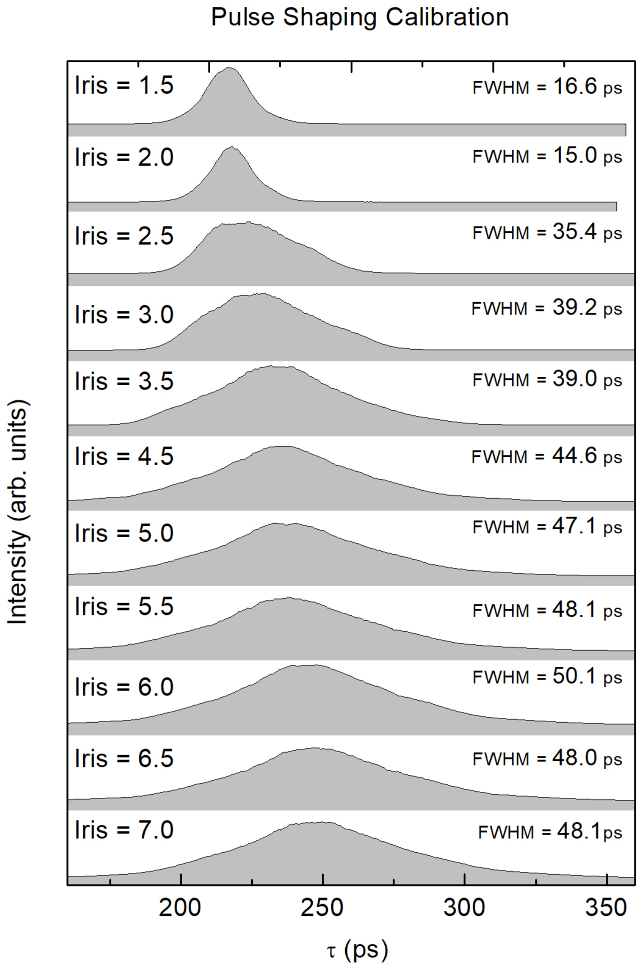

Figure 3.18: ***Pulse width characterisation.*** *Temporal profiles of the modified laser pulses. There is some slight distortion of the pulse profile in the 30-40ps range, however this can be corrected in real time by using the continuous run function on the streak camera and fine tuning the fibre coupling.*

This means that at the optical fibre, different spectral bandwidths will be coupled into the fibre. After the pulse is coupled into the fibre, the modified pulse is sent to an Optronis SC-10 streak camera to verify the pulse width in real time, and a HighFinesse GmbH WS8-10 wavelength meter to verify the wavelength. Fig 3.18 shows the streak camera temporal profiles of pulses achieved using this technique with pulse durations (using FWHM of pulse profiles) of ≈16-50 ps. Comparing this range of pulse widths with the polariton lifetimes in Fig 3.15, this technique can reach pulse durations at least double the duration of the longest polariton lifetime.

3.6 Photon Correlation Measurement Calibration

To observe microcavity polaritons dynamics, we look to the photons that leak out of the cavity since the polariton mode is imprinted onto the photonic mode. This means that the emitted light stream will experience photon number fluctuations which can be directly traced back to the dynamics happening inside the microcavity polariton system. To characterise these fluctuations and determine the photon state leaking out of the cavity, the statistics of the photon stream are measured and analysed. In most cases, there are three different categories of photon statistics which compare the variation of the states photon number distribution to a Poissonian photon number distribution. These states are called Poissonian, super-Poissonian and sub-Poissonian, which refer to the fluctuations having equal, larger or smaller variation than that of an uncorrelated, coherent photon state.

To experimentally observe the photon statistics, we must have some way of recording the arrival times of the emitted photons. We accomplished this by using the celebrated Hanbury Brown and Twiss interferometry technique [97] which has become the standard method for measuring photon statistics. This technique employs a 50/50 beamsplitter to split the photon stream into two branches which are guided onto two separate APD detectors operating in the photon counting mode. Specialist electronics are used to measure the time between detection events so that one APD starts the timer and the other APD stops the timer. The time period or delay of the coincidences of detection are binned accordingly in values of absolute time delay, with only the APD time resolution and electronic jitter limiting the minimum detection window and hence, precision.

3.6.1 Optical Cross-talk Calibration

The HBT interferometry technique is a straight forward and robust technique for measuring photon statistics by photon correlation. In order to extract useful information from this measurement by means of the second order correlation function at $\Delta t = 0$ or $g^{(2)}(0)$, the coincidence counts at or near $\Delta t = 0$ is compared to coincidence counts for $\Delta t \to \pm\infty$. To ensure that this can occur within the limitations of the equipment, an electronic delay by means of a long co-axial cable leading from the APD to the correlation electronics is used in the ‘stop’ channel of the setup. This delay provides an ‘offset’ in absolute time delay to $\Delta t = 0$ such that $\Delta t < 0$ coincident values can be recorded. If this was not the case, $\Delta t = 0$ and the first time bin of the correlation histogram would coincide which would mean the loss information about $\Delta t < 0$ as the electronics only measure positive absolute time delays. Therefore, in order to make a definite statement about the photon statistics and analyse the coincidence histogram measurements, this offset or zero delay time (ZDT) must be accurately calibrated. While it is possible to use a calibrated light source that exhibits strong photon correlations i.e. bunched or antibunched light, these items would not be readily available in most labs at the wavelengths of interest. Lasers are unsuitable for this calibration due to their coherent nature and flat correlation function. However, we develop an alternate means of calibrating the ZDT using optical crosstalk between the APD devices used in our HBT setup.

In APD devices, following the initial absorption of a photon in the active area of the APD, photon re-emission from the APD can occur due to an effect known as afterglow or breakdown flash in the APD [98]. These re-emitted photons can lead to false detection events commonly known as optical cross-talk, which can lead to an inaccurate statistics of the photon stream which is clearly an undesirable situation. In recent years, the problem of optical cross-talk has been studied in detail to develop a complete understanding of the origins and propagation of this phenomenon in APD arrays [99]. Based on these studies, several new APD chip designs were developed to reduce optical cross-talk such as trenches [100], absorbing filter layers [101] and back illumination [102], with varying degrees of success. However, for the most part, a typical quantum optics lab will be equipped with off-the-shelf silicon APDs that have little or no in-built cross-talk reduction which means active steps have to be taken on the experimental side to calibrate [103] and suppress this unwanted side-effect. However, we show that with careful engineering of the optical cross-talk, this effect can be made into a useful tool for determining the ZDT in HBT interferometers by placing a mirror on the fourth, unused port of the 50/50 beamsplitter in the HBT setup, the so-called 'vacuum port'. Inserting a mirror in the 'vacuum' port significantly enhances the optical cross-talk, allowing for straight forward identification of the ZDT. This mirror can then be blocked, leaving the setup ready to measure, providing an *in-situ* and non-invasive means of calibrating the zero delay time.

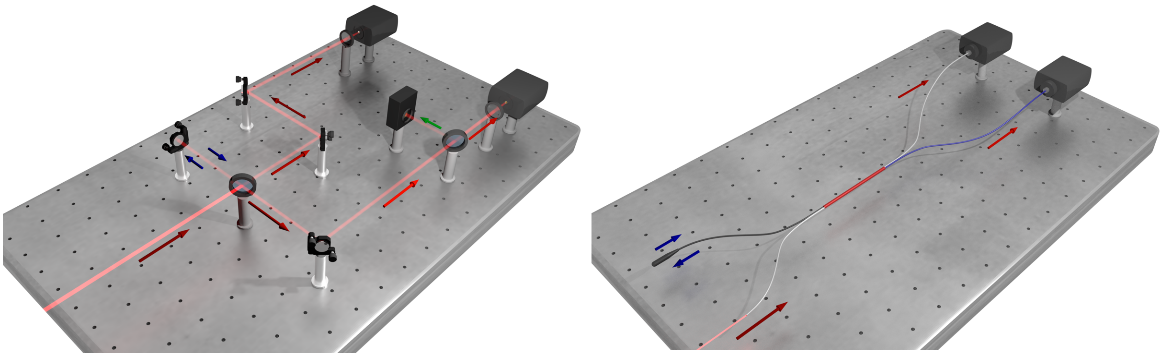

Figure 3.19: ***Optical cross-talk calibration of the ZDT experimental setup.*** *Free-space optics* **(a)** *and fiber-based* **(b)** *HBT interferometers. A retro-reflecting extra mirror is placed in the free 'vacuum' port in both of the interferometric setups. The mirrors reflect any secondary emission from the APDs (blue arrows) back into the detection arms. The extra pellicle beamsplitter and CCD camera (near green arrow) in the right hand detection arm of* **(a)** *is used for alignment purposes only.*

To demonstrate the versatility of this new method, the HBT interferometer was operated in the two most common ways: as a free space optics setup and as a fibre configuration as shown in Fig 3.19. The mirror placed in the 'vacuum' port of the beamsplitter directs otherwise lost photons from secondary emission events within the APDs back into the detection arms of the interferometer where they can be re-detected. This leads to 'fake' coincidences which are displaced from the ZDT by the travel time required to go from one APD to the other. Due to the symmetry of the system, two cross-correlation peaks appear symmetrically around the ZDT, making it straight forward to identify the ZDT. In the case of free-space optics, alignment of the mirror in the 'vacuum' port was achieved using a low power laser, an extra beamsplitter and a CCD, as shown in Fig 3.19 (a). The CCD is used to overlap the reflections from the APD front and the extra mirror. Once the ZDT is found, the extra mirror in the beamsplitter 'vacuum' port can simply be blocked (or removed) without disturbing the calibration of the system.

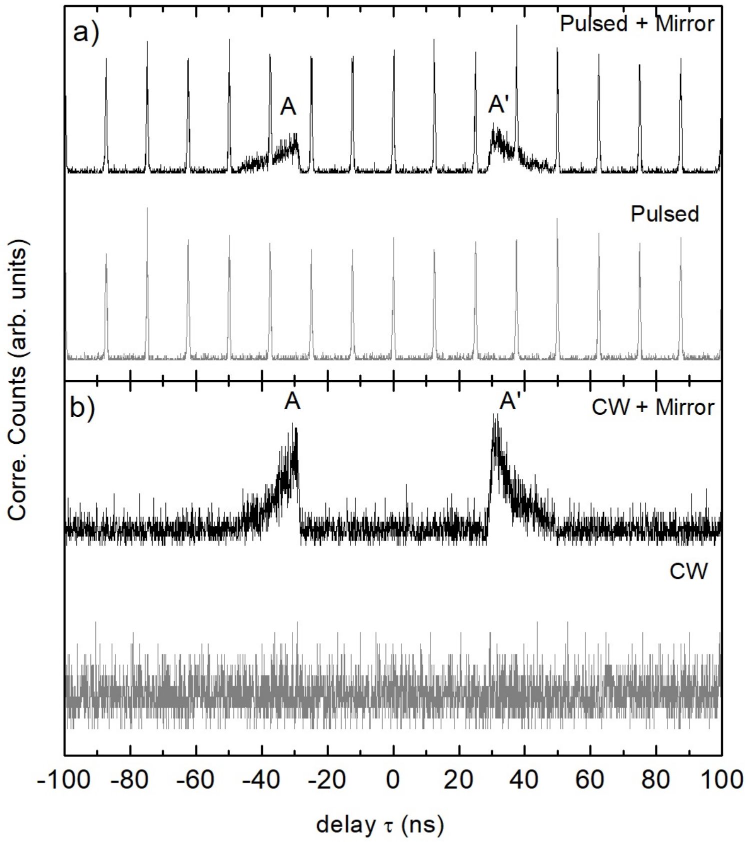

Figure 3.20: ***Free optics HBT photon correlations with optical cross-talk.*** *Raw photon correlation data in the free optics HBT configuration in both pulsed* **(a)** *and CW* **(b)** *laser operation. The upper traces of both* **(a)** *and* **(b)** *correspond to having the extra 'vacuum' port mirror while the bottom traces do not. In the upper traces of both* **(a)** *and* **(b)** *two sets of additional cross-talk peaks appear at ~3 ns (A, A') and ~6 ns (B, B') delay (positive and negative) from the main peak. They correspond to the time of flight of approximately 1 m between the two detectors. These peaks vanish in the bottom plots of* **(a)** *and* **(b)** *when the extra mirror is removed.*

In the experiments, we used two types of silicon APDs: one pair from ID Quantique (ID-100) with a detection efficiency of 18% at 700 nm, a time resolution of 40 ps and a dark count rate of less than 5 Hz, and the other pair from Perkin Elmer (SPCM-AQ4C) with a detection efficiency of 49% at 805 nm, a time resolution of 350 ps and an average dark count rate of 500 Hz. In the fibre-based set-up, we used a 50/50 fibre coupler as beamsplitter and a fiber-based mirror plugged to the fourth port of the fibre coupler (Figure 3.19 (b)). Four different lasers provided the light for the experiment: a pulsed Ti^{3+}:Sapphire laser (Coherent MIRA, laser 1) with pulse width < 3 ps at a repetition rate of 76 MHz, a CW Ti^{3+}:Sapphire laser (MSquared SOLSTIS, laser 2) at 750 nm, a pulsed Ti^{3+}:Sapphire laser (Coherent Chameleon,laser 3) with pulse width 140 fs at a repetition rate of 80 MHz, and finally a CW diode laser (Toptica DL 100 Pro design, laser 4) at 805 nm. The correlator box (time-to-amplitude converter) is from PicoQuant (PicoHarp 300) and has a nominal time resolution of 25 ps.

Fig 3.20 (a) shows the raw histogram data taken with the ID Quantique ID-100 APDs, Laser 1 as the light source and in free-space optics configuration. The upper trace (pulsed plus mirror) corresponds to the photon correlation data with enhanced cross talk due to the extra mirror in the fourth port of the beamsplitter. For reference, the lower trace (pulsed) was taken without the extra mirror. In both cases, the widths of the coincidence peaks is limited by the time resolution of the APDs and can be fit by a Gaussian peak with approximately 70 ps width, corresponding to $\sqrt{2}$ of the individual APD time resolution. Besides the dominant Gaussian peak, a secondary exponential tail due to APD bias switching [104] is visible. The secondary tail is caused by photons, which penetrate the depletion layer in the semiconductor diode and generate photons in the neutral regions nearby [105].

Both plots of Fig 3.20 (a) are almost identical, except for the appearance of four small additional peaks around the ZDT peak in the case of the extra mirror. The first pair of peaks, labeled as A and A', are ~3 ns away from the main peak. The time delay difference depends on the time of flight between the two detectors, and nicely coincides with the approximately 1 m traveling distance between both APDs. The second pair of peaks, labeled as B and B', correspond to double the delay time and are associated with multi-emission/reflection of secondary photons. The presence of these four small peaks indicates efficient enhancement of cross-talk between the APDs due to the presence of the additional mirror. The appearance of the cross-talk therefore allows for the clear identification of the main peak representing the zero delay time of our specific HBT setup.

The histogram in Fig 3.20 (b) was recorded using the CW laser 2 in free-space optics configuration. As before, the lower trace shows the coincidences with the conventional HBT setup, while the extra mirror is present in the top trace. As before, the extra mirror causes four additional small peaks to appear around the ZDT. Both measurements demonstrate that the additional mirror leads to significantly enhanced optical cross-talk, which can be used to calibrate the zero delay time in a HBT-based photon correlation experiment. All histogram plots in Fig 3.20 were taken over a 10→12 hour time period with ≈1000 cps in each APD channel. Increasing the laser power will reduce the significance of the cross-talk coincidences compared to ‘real’ coincidences from actual laser photons and will therefore suppress the cross-talk signal. This is due to the fact that the number of secondary photon emissions in APDs is determined by the bias voltage [106] and not on the incoming photon number.

Although many experiments use free-space optics for HBT experiments due to minimal photon losses, in some circumstances it is desirable to use fibre-based photon correlation set-ups, in order to, for example, improve filtering efficiency in fibre-based confocal microscopy experiments [107]. The beamsplitter and ‘vacuum’-port mirror in the free-space setup can be replaced by fibre beamsplitters and fibre-based mirrors which can be bought off the shelf and are real ‘plug-and-play’ devices. Our cross-talk technique can be easily adapted to such a fibre-based HBT, as Fig 3.21 (a) and 3.21 (b) demonstrate. These are autocorrelation data taken with Lasers 3 and 4. All histogram plots in Fig 3.21 were taken over a 1 hour time period with ≈ 4000 cps in each APD channel. Again, we see peaks appear at approximately ±30 ns from the ZDT in the upper traces of Figs 3.21 (a) and 3.21 (b), when the mirror is present. As before, these peaks disappear when the extra mirror is removed. In both cases, the cross-talk peaks are located at considerably longer delay and are considerably broader compared to those found in Figs 3.20 (a) and 3.20 (b).

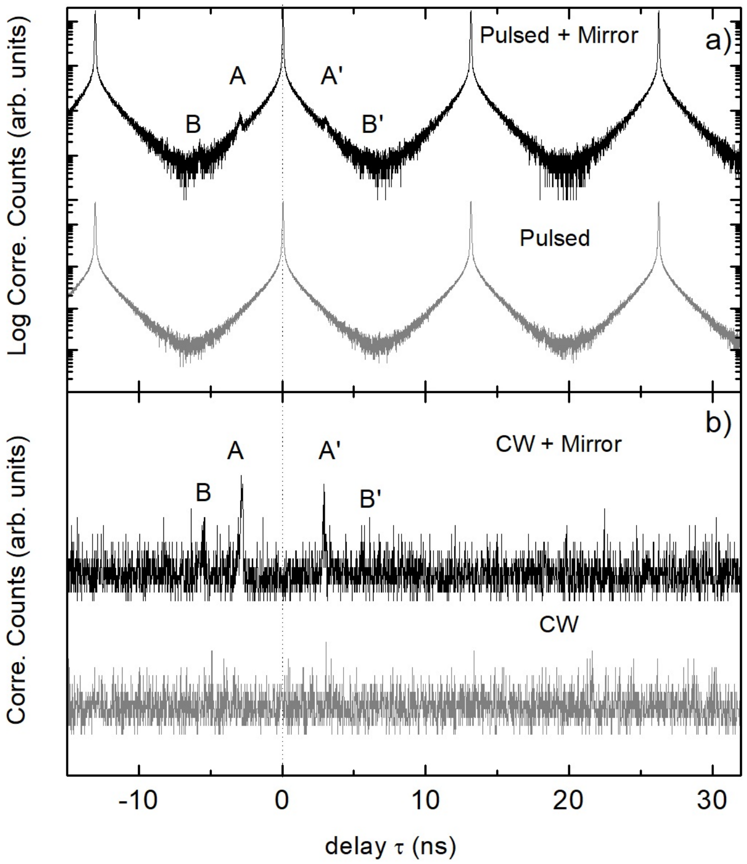

Figure 3.21: ***Fibre based HBT photon correlations with optical cross-talk.*** *Raw photon-autocorrelation data in the fibre-based HBT configuration for both pulsed* **(a)** *and CW* **(b)** *laser operation. The upper traces of* **(a)** *and* **(b)** *were taken with the extra 'vacuum' port mirror present while for the lower traces the mirror was removed. The upper traces of* **(a)** *and* **(b)** *show peaks A, A′ ~30 ns away from the main peak. This corresponds to the in-fiber time-of-flight between the two detectors and an effective fiber length of approximately 2 x 3 m (entire optical path of the reflected light). These peaks vanish in the lower traces of panels* **(a)** *and* **(b)** *with the extra mirror removed.*

We attribute this to the longer optical path (total light travel in the fiber is 6 m, with refractive index n∼1.463) in combination with the strong dispersion in the fibers. This results in a slower group velocity of the wave packet and longer time of flight, shifting the peaks further away in time from the zero delay. The width is likely to result from optical dispersion of the wavelength components of the Si-APD secondary emission, and potentially from the presence of additional nonlinear processes present in the fibre.

In our experiment, the calibration of the ZDT is critical, as the expected antibunching signal is in the region of only a few percent. If the ZDT is not clearly and precisely known, later analysis of the correlation histogram will become impossible as it will be unclear where the antibunching signal actually occurs in time, and therefore comparison with the uncorrelated signal cannot be performed as is necessary for calculating $g^{(2)}(0)$.

4

Quantum-correlated photons from semiconductor cavity polaritons

In this chapter, photon correlation measurements of optically confined quantum well polaritons in two microcavities are presented and analysed. We observe small but distinct photon antibunching which is a result of strongly interacting microcavity polaritons. The analysis protocols for the second order autocorrelation function analysis is also included to provide a clear understanding on the determination of $g^{(2)}(0)$ *with its errors and fitting confidence of numerical models to experimental trends. The findings presented in this chapter are published in Nature Materials [87].*

In order to observe the anticipated polariton blockade regime in our fibre-based microcavity system, resonant photon correlations will be performed using the standard Hanbury-Brown and Twiss interferometer technique. In order to improve our ability to observe the polariton blockade, the microcavity polariton parameter measurements and parameters presented in Chpt 3 give us important information about the behaviour of the polariton system. From this information, it is clear that the polarisation splitting of the polariton mode and the negative trion state will play an important role in any resonant photon correlation measurements.

4.1 Photon Correlation of Optically Confined Microcavity Polaritons

4.1.1 Photon Correlation Measurements

We carried out a first set of correlation measurements for three different cavity-exciton detunings Δ's. At each Δ, we took data for five different laser detunings (Δ_{LP}'s), where $\Delta_{LP} = 0$ corresponds to the laser at resonance with the π_X polariton mode an uncertainty imposed by the resolution of spectrometer used to modify the laser pulses ~ 45 meV. While we tried to excite predominantly the π_X mode, the polarisation was not monitored and actively corrected during correlation measurements. We note, though, that in an independent characterisation measurement, we found the polarisation to be stable over hours. For each pair (Δ_{LP}, Δ), a raw coincidence trace like the one shown in Fig 4.1 is obtained.

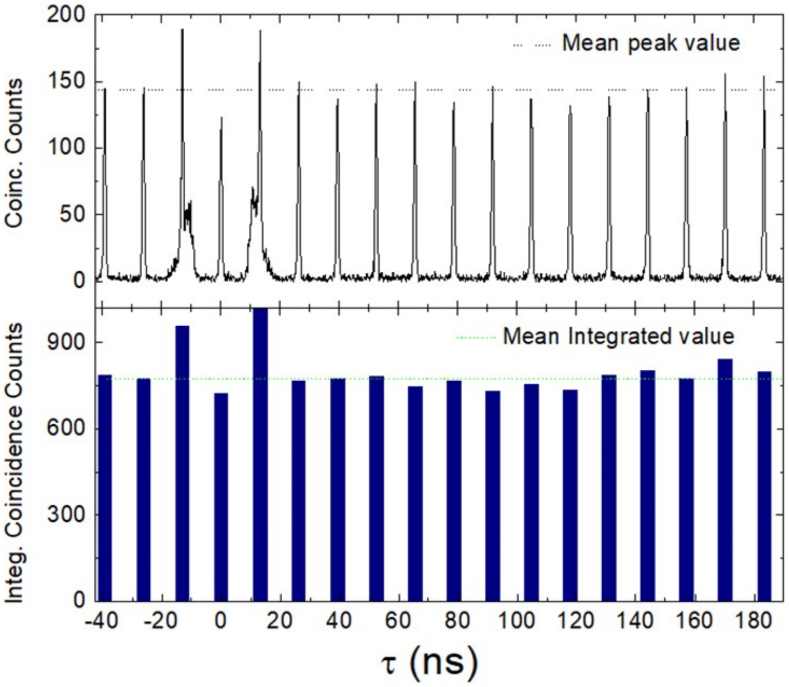

Figure 4.1: ***Antibunched raw coincidence data and integrated coincidences histogram.*** *Upper panel: Extended coincidence counts histogram for the raw data. The mean peak value is indicated by a dotted black line. Lower panel: Integrated coincidences histogram (blue bars) extracted from the raw data by following the analysis protocol described in section 4.1.3. The mean integrated value is indicated by the dotted green line.*

A zoomed-in version of the full scale trace shown in Fig 4.1 is presented in Fig 4.2 (d). The arrow in Fig 4.2 (d) indicates the position of the zero-delay peak that contains the quantum correlations of the system which is used to extract $g^{(2)}(\tau = 0)$. The immediate neighboring peaks are neglected in the analysis since they exhibit bunching due to APD crosstalk (see section 3.6.1). All other peaks being far apart in time ($n \times 13$ ns) constitute a reference of purely uncorrelated detection events. From raw traces such as this one, $g^{(2)}(0)$ as well as its 1σ confidence interval is extracted (see section 4.1.3). The result of this analysis for the fifteen pairs (Δ_{LP},Δ) is shown in Fig 4.2 (a)-(c).

The experimental plots of $g^{(2)}(0, \Delta_{LP})$ obtained in this way exhibit substantial deviations from the uncorrelated baseline $g^{(2)}(0) = 1$. Consistently, and in line with the theoretical expectation, $g^{(2)}(0, \Delta_{LP})$ is mostly smaller than 1 for negative Δ_{LP} and larger than 1 for positive Δ_{LP}. These deviations from 1 reflect the presence of additional quantum correlations generated by transmission through the fiber-cavity polariton system. However, for some of the data points (in particular Fig 4.2 (c)), the deviations are not in line with theoretical expectations from the single-mode polariton blockade model.

In order to get a quantitative understanding of our data, we use the theoretical model in Eqn (2.39) to perform numerical simulations, taking into account our experimental parameters, the

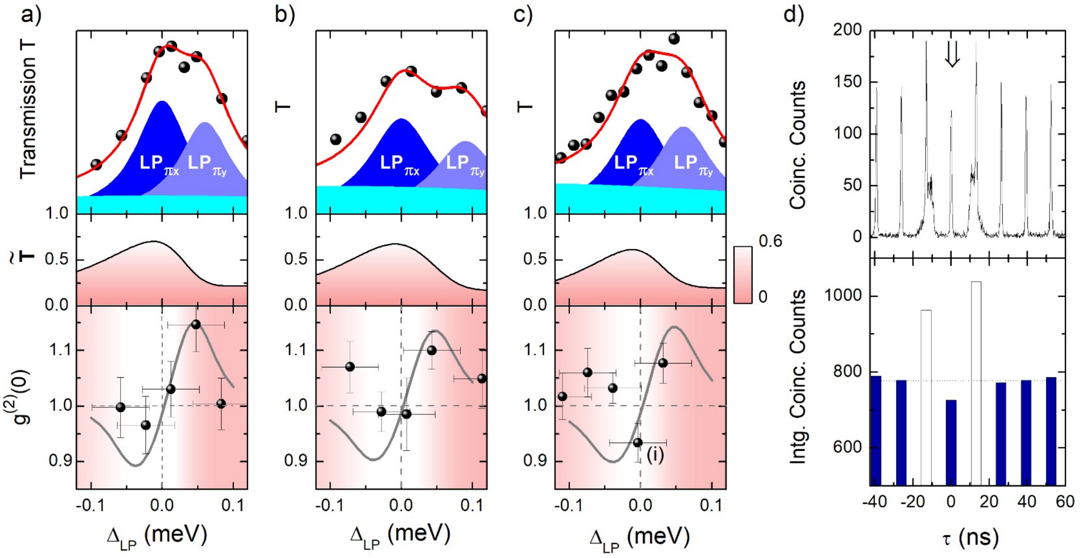

Figure 4.2: ***Quantum correlated photons with cavity-exciton detuning***. ***(a)****-****(c)*** *Photon autocorrelation data $g^{(2)}(0)$ for three different cavity-exciton detunings $\Delta = 0.14$* ***(a)****, 0.83* ***(b)*** *and 1.11 meV* ***(c)****. At each Δ, we measure $g^{(2)}(0)$ for five different laser detunings, Δ_{LP}. Each subfigure contains three subpanels, with the top panel showing the corresponding resonant laser scan. The bottom panel displays the corresponding correlation data (black dots) along with the calculation from the single-mode theory (two lines corresponding to upper and lower bounds of the interaction strength). The middle panel contains a plot of the transmission fraction $\tilde{T}$. This parameter gives an indication of the perturbation of the mode of interest, π_x through the presence of the orthogonally polarized polariton mode π_y and the trion resonance. Both are expected to lead to a significant deviation of the measured $g^{(2)}(0)$ from the single-mode theory. Hence, only regions with large $\tilde{T}$ are expected to give correlation data that are close to the expected theory values. In subfigure* ***(c)*** *only the data point* ***(i)*** *around zero detuning Δ_{LP} shows negligible influence from π_y and the trion resonance. It exhibits antibunching around $g^{(2)}(0) = 0.93 \pm 0.04$, with the corresponding raw data displayed in subfigure* ***(d)****. The dip at zero time delay is clearly visible both in the raw correlation trace and the integrated coincidences plot.*

pulsed nature of the excitation, and the experimental integration over all possible correlation times. Including a quantitative description of how photon correlations are affected by the trion resonance or the neighboring polariton mode π_Y would require new theoretical developments that clearly go beyond the scope of this thesis. Instead, in order to make sense of the comparison between experiment and theory, we determine the range of validity of the model. To do so, we define $\tilde{T}(\Delta_{LP}) = T_X(\Delta_{LP})/[T_X(\Delta_{LP}) + T_Y(\Delta_{LP}) + T_{X^{-1}}(\Delta_{LP})]$ which quantifies the fraction of transmitted laser light explained by the π_X polariton mode alone. It estimates the amount of perturbation this mode is subject to for a given Δ_{LP}, due to its spectral overlap with the other perturbing transitions. $T_X(\Delta_{LP})$, $T_Y(\Delta_{LP})$, and $T_{X^{-1}}(\Delta_{LP})$ are the contributions to the transmission spectra of the π_X and π_Y polariton modes, and of the trion resonance respectively, determined from the transmission measurements. Hence, $\tilde{T}$ equal to 1 means that the π_X polariton mode is unperturbed. For this ideal case, we expect the best possible agreement with the single-mode theory. The smaller $\tilde{T}$, the more the π_X polariton mode is perturbed, and the more the experiment is expected to depart from the single-mode theoretical expectation.

The resulting $\tilde{T}(\Delta_{LP})$ is shown as middle panels in Figs 4.2 (a)-(c) and Fig 4.3 (a). In addition, it is also underlaid as a color map with the measured $g^{(2)}(0)$ data points in the lowest panels of Figs. 4.2 (a)-(c) and Fig 4.3 (a). Interestingly, data points lying in high values of $\tilde{T}$ (light areas) exhibit a very good quantitative agreement with the theoretical expectation. This is the case for example of most points close to resonance ($\Delta_{LP} \simeq 0$), where a trend towards antibunching is visible.

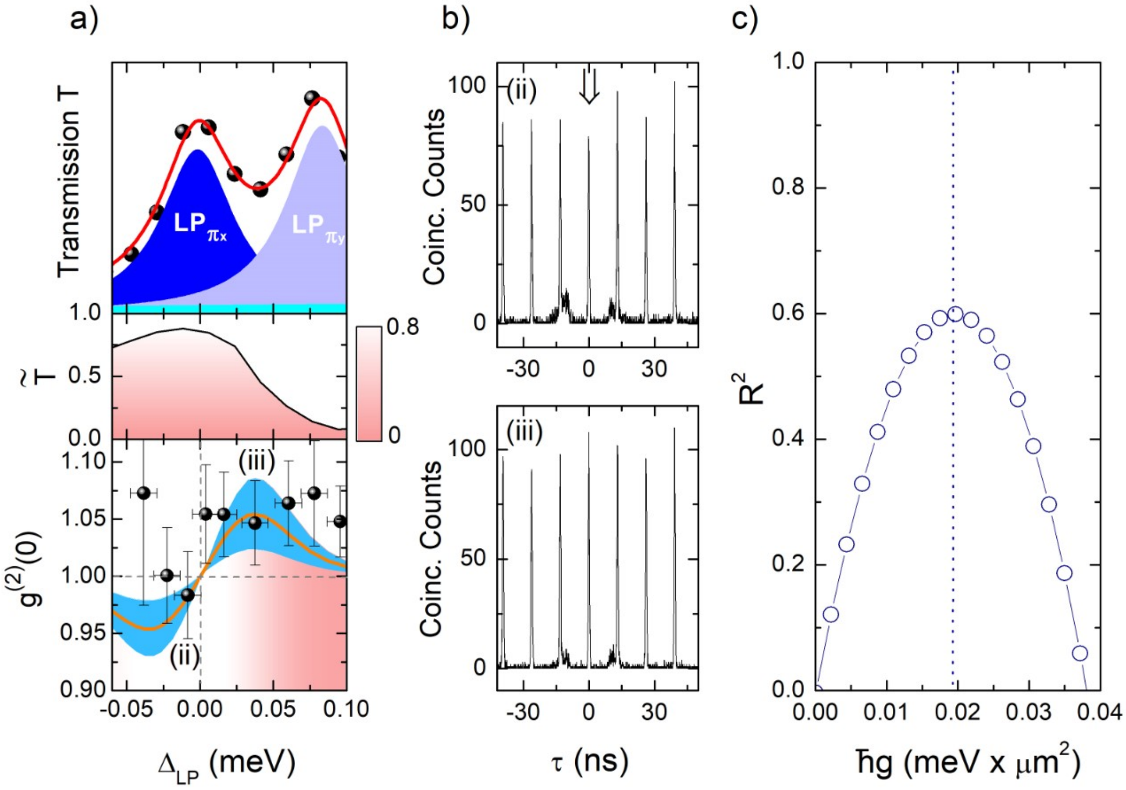

Figure 4.3: ***Polariton-Polariton interaction constant***. ***(a)*** *Correlation data near cavity-exciton resonance. The top panel contains the corresponding resonant transmission laser scan while the middle panel shows the calculated transmission fraction* $\tilde{T}$. *The bottom panel displays* $g^{(2)}(0)$ *as a function of laser detuning* Δ_{LP} *from the position of the LP* π_x*-resonance for a cavity-exciton detuning of* $\Delta = 0.07$ *meV. Except for the two rightmost points which are heavily influenced by the* π_y *mode, all other data points are from almost pure* π_x*-mode photons.* ***(b)*** *Example raw correlation traces from the two points* ***(ii)*** *and* ***(iii)*** *in subfigure* ***(a)***. ***(c)*** *Coefficient of determination* R^2 *of the data fit with the theoretical model versus interaction parameter* $\hbar g$. *The most likely value is* $\hbar g_0 = 0.020 \pm 0.011$ *meV·μm*^{2}.

The point labeled (i) in Fig 4.2 (c) is particularly interesting as it benefits both from a good $\tilde{T}$, a large excitonic fraction, and $\Delta_{LP} \approx 0$, a situation in favor of the strongest antibunching among all data points. Despite this, the measurement uncertainty remains rather large and the perturbation is non-zero ($\tilde{T} = 0.65$), so that it is hard to infer the actual value of $g^{(2)}(0)$ we would find in an ideal measurement, and in absence of perturbation from the trion.

Points lying in low $\tilde{T}$ areas on average exhibit an excess of bunching as compared to the theory. This is particularly clear for the three leftmost points in Fig 4.2 (c), for which the perturbation is mostly due to interaction with the trion resonance. This trend is actually expected, as coupling with the trion transition, and in particular re-emission through the polariton mode, will generate classical noise of thermal origin (mediated by trion-phonon or trion-free charges interaction). When the perturbation comes from the neighboring cross polarized polariton mode, the influence on $g^{(2)}(0)$ seems less dramatic (compare, for example, the two rightmost points in Fig 4.2 (a) and Fig 4.2 (b)). This also makes sense as a polariton mode is much shorter lived and much less coupled to thermal noise mediated by phonons or free charges. In this case, the polariton-polariton correlations are largely lost due to a loss of the single mode character of the polariton modes and thus an effective loss of the interaction strength. We thus see that our entire data-set can be qualitatively, and to some extent quantitatively, explained by polariton-interaction mediated correlations that are significantly altered by the presence of unwanted transitions, namely, the trion resonance and the cross-polarised polariton mode.

For the final measurement, we therefore attempted to optimize the microcavity parameters such that $\tilde{T}$ is as large as possible over a broad window of Δ_{LP}. This situation is met for a detuning $\Delta = 0.07$ meV, for which the polarization split polariton modes are well separated, and the trion resonance lies far away on the blue side of the polariton mode. The results are shown in Fig 4.3 (a) (bottom panel), together with the transmission spectrum (top panel) and $\tilde{T}(\Delta_{LP})$ (middle panel). The results are consistent with our previous analysis: the rightmost points that approach the trion resonance as well as the π_Y polariton mode exhibit a slight excess of bunching (which lies within the error bars). The left side points, which are very well protected from the sources of perturbation, are well in-line with the theoretical prediction. The leftmost point being strongly detuned from the polariton mode has weak transmission and thus suffers from a low count number, which is reflected by its extremely large error bar. The raw coincidence traces for points labeled (ii: $g^{(2)}(0) = 0.98 \pm 0.04$) and (iii: $g^{(2)}(0) = 1.06 \pm 0.04$) are shown in Fig 4.3 (b) as an illustration of the kind of raw correlation traces obtained for a high photon number.

Owing to a better signal-to-noise, we take advantage of this latter data-set to estimate quantitatively the strength of the polariton-polariton nonlinearity, by comparing it with our model. The best fit is obtained for a confinement-enhanced exciton-exciton interaction constant $\hbar\omega_{NL} = 0.018 \pm 0.010$ meV. The calculated $g^{(2)}(0, \Delta_{LP})$ for this central value is shown as the solid line in Fig 4.3 (a). For this fitting procedure, we have excluded the two rightmost points at large positive Δ_{LP} since, as explained above, they have a low $\tilde{T}$ and are thus not expected to fit the theory.

To obtain a more generic polariton-polariton interaction strength $\hbar g$ it is necessary to scale $\hbar\omega_{NL}$ by the mode overlap between the photonic cavity mode and the exciton wavefunction using the Gaussian mode waist size of $w_0 = 1.17$ μm calculated in section 3.3. In this case, $\hbar g = \hbar\omega_{NL}|C_x|^4\pi w_0^2$, using the scaling area πw_0^2. With an excitonic fraction $|C_x|^2 = 51\%$ this analysis yields $\hbar g_0 = 0.020 \pm 0.011$ meV·μm^2. The confidence of this value is illustrated by the plot in Fig 4.3 (c) that shows the coefficient of determination $R^2(\hbar g)$ of the theoretical fit to our data. $R^2(\hbar g)$ exhibits a clear maximum for $g = g_0$, as well as a peaked structure from which the uncertainty is well-defined. Our measurement returns an exciton-exciton interaction strength $\hbar\kappa = 0.076 \pm 0.042$ meV·μm^2, which is in good agreement with previously reported values in literature [3, 84, 108] and also is in good agreement with the value determined in a similar measurement by the ETH Quantum Photonics group[109].

4.1.2 Photon correlation measurement in a second cavity

We carried out a second set of photon correlation measurements in a second fiber cavity with different cavity parameters. While the radius of curvature for this cavity was similar to the previous one, the cavity lifetime of 8.3 ps was significantly shorter than for the other cavity. Fig 4.4 (a) displays the low-temperature photoluminescence (PL) map as a function of cavity detuning (Δ), obtained under non-resonant excitation (at $E_L = 1.55$ eV). The characteristic avoided crossing of the excitonic and photonic modes was observed, producing the Lower Polariton (LP) and Upper Polariton (UP) dressed states. We find a vacuum Rabi splitting of $2\hbar\Omega_R = 3.04$ meV, with slightly higher QW exciton energy ($E_X = 1480.65$ meV) than in the spot studied in section 4.1.1.

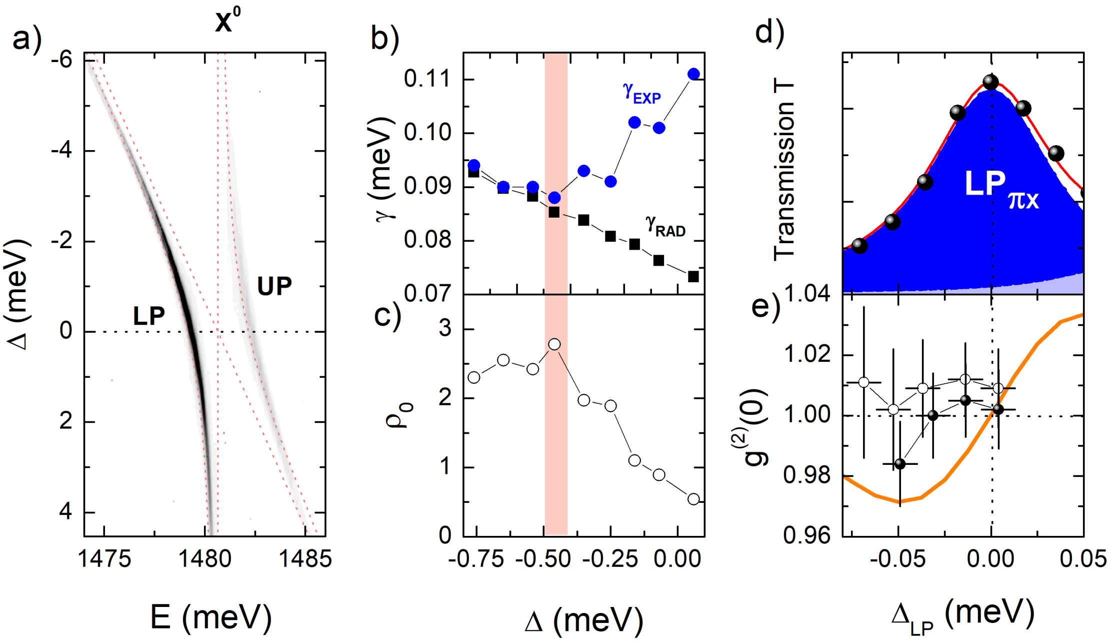

Figure 4.4: ***Optical characterisation and photon correlation measurement in a second fiber cavity.*** ***(a)*** *Low-temperature photoluminescence (PL) map as a function of cavity detuning* (Δ). ***(b)*** *Experimental LP linewidth* (γ_{Exp}) *(blue filled circles) and the calculated LP radiative linewidth* (γ_{Rad}) *(black filled squares) as a function of* Δ. ***(c)*** *Evolution of the figure of merit* ρ_0 *as a function of* Δ. *In both* ***(b)*** *and* ***(c)*** *figures* $\Delta = -0.45$ *meV (redish shadow) shows the best signal-to-noise ratio for the photon correlation measurements.* ***(d)*** *Measured resonant transmission spectra of the the* π_X *LP transition (black dots), and Lorentzian fitting to both linear LP transitions (bluish shadows). The red continuous line represents the cumulative fit.* ***(e)*** *Photon correlation measurements as a function of laser detuning* (Δ_{LP}) *for* $\Delta = -0.45$ *meV and two excitation powers: 700 pW (open circles) and 200 pW (filled circles).*

In order to evaluate the best Δ to carry out photon correlation measurements and to minimize the effect of the trion transition, we measured resonant transmission spectra in the close vicinity of $\Delta = 0$. Fig 4.4 (b) displays the evolution of the experimental LP linewidth (γ_{Exp}) (blue filled circles) and the calculated LP radiative linewidth (γ_{Rad}) (black filled squares) as a function of Δ. As displayed, at $\Delta \simeq -0.45$ meV both quantities start to diverge as a consequence of the losses produced by the scattering with the trion transition.

As a second control parameter, we calculated the following figure of merit ρ_0:

$$\rho_0 = \frac{|C_X|^4\sqrt{R_0}}{\gamma_{Exp}} \times f_P; \;\; f_P = \frac{\gamma_{Rad}}{\gamma_{Exp}}; \;\; R_0 = \frac{R_{Det}^2}{\theta} \tag{4.1}$$

where R_{Det} is the detector count rate and θ is the pulsed laser frequency. ρ_0 therefore measures the detector count rate versus the polariton linewidth promising the best signal-to-noise ratio for the measurements at its maximum value. Fig 4.4 (c) shows the evolution of ρ_0 as a function of Δ, with $\Delta = -0.45$ meV corresponding to the position of its maximum. As both direct linewidth and ρ_0 criteria coincide, we have performed photon correlation measurements as a function of laser detuning (Δ_{LP}) for $\Delta = -0.45$ meV and two excitation powers. Fig 4.4 (e) shows the measured $g^{(2)}(0)$ value when scanning the low energy tail of the π_X LP transition (Fig 4.4 (d)) with the excitation laser. Here we use two different average excitation powers: 700 pW (open circles) and 200 pW (filled circles). When using high excitation power, all measurements return $g^{(2)}(0) \geq 1$. However, when the excitation power is reduced to 200 pW, we find a clear minimum $g^{(2)}(0) = 0.984 \pm 0.014 < 1$ at $\Delta_{LP} \simeq -0.05$ meV. Due to the low count rate at this power, the integration time for this single data point was 96 hours. The result from our polariton-model simulations with $\hbar\omega_{NL} = 0.018$ meV is shown as continuous orange line.

The loss of antibunching statistics with higher excitation power is in line with the theoretical prediction of Verger *et al.*[42], and coincides with the results presented by Delteil *et al.*[109], with their data following a very similar trend to the one observed here.

4.1.3 Second order correlation function analysis protocol

The avalanche photodetectors (APDs) that we used in this experiment have a time resolution of ≃350 ps. Since the polariton dynamics under resonant excitation is < 40 ps, we can reasonably assume that the correlations between two photons delayed by this timescale are equally spread over the whole measured zero-delay coincidence peak. On the other hand, it also means that since the other coincidence peaks are separated by an integer multiple of 13 ns (laser repetition period), they cannot feature any polariton correlations. Fig 4.1 shows an extended raw two-photon coincidences histogram and the corresponding integrated coincidences histogram for our strongest antibunching in Fig 4.2 (c) of data point (i). Given the rather small contrast of the antibunching and the overall noise in the data, a careful statistical analysis is needed.

In order to maximize the statistical significance of our data, we chose to truncate the data of the zero delay peaks (centered at bin zero) at time bins $\pm W$, and hence reject the far edges of the peaks which contain more dark coincidence counts from the APDs than actual signal. To determine the optimal W, we modeled the coincidence counts in each time bin j as being the sum of the signal S_j, the statistical noise related to the number of counts uncertainty and the dark coincidence counts. As a result, the sum of the zero delay coincidences reads:

$$A_0 = \sum_{j=-W}^{W} S_j, \tag{4.2}$$

and the corresponding signal-to-noise as:

$$SNR(W) = \frac{\sum\limits_{j=-W}^{W} S_j}{\sqrt{\sum\limits_{j=-W}^{W} S_j + (2W+1)S_D}}, \tag{4.3}$$

where S_D is the number of dark coincidence counts which is a constant over all bins (whether it is due to dark/dark, dark/signal or signal/dark coincidences).

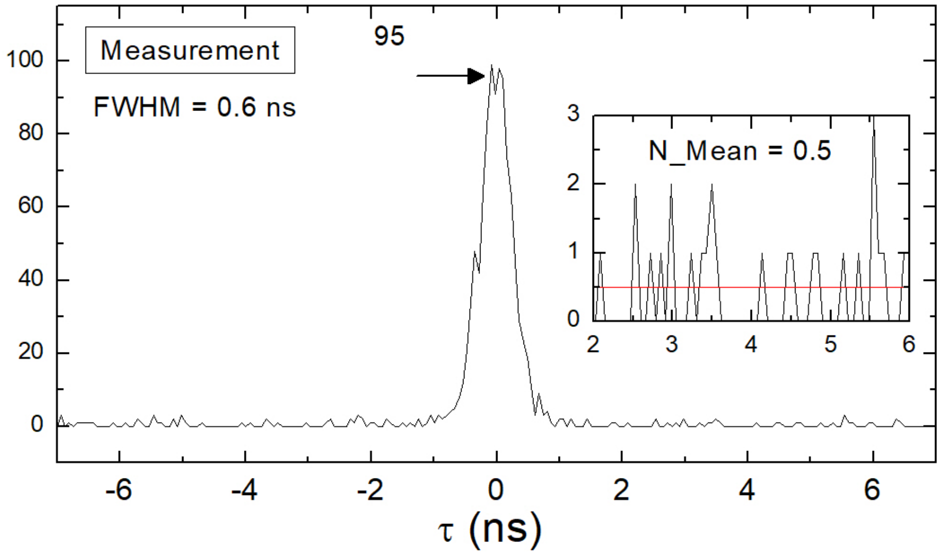

Figure 4.5: ***Typical zero-delay raw coincidences peak.*** *The FWHM of the zero-delay peak is 0.6 ns, with a maximum of 95 coincidence counts. Dark coincidence counts from the detectors are delay independent, and amount here to 0.5 counts on average (Inset).*

The signal-to-noise function (Eqn (4.3)) exhibits a maximum that depends on these parameters. Fig 4.5 shows a typical raw zero delay correlation peak. A dark count of $S_D = 0.5$ counts per bin is found, and the Gaussian best fit of the peak exhibits a full width at half maximum of 600 ps and an amplitude of 95 counts in the central bin. With these parameters the largest signal-to-noise ratio is achieved for a truncation window of $2W = 896$ ps full width.

$g^{(2)}(0) = \frac{A_0}{\langle A \rangle}$ is then determined as the ratio of the sum of the counts in the zero delay peak within the truncation window (A_0) and the average sum of the counts in the uncorrelated peaks within the same truncation window ($\langle A \rangle$). The experimental uncertainty on A_0 is derived from the measured standard deviation σ of A_k, the sum of the counts in the peak k (also truncated) where k runs over every peak of uncorrelated events (300 peaks in total). Then, according to the central limit theorem, the uncertainty over $\langle A \rangle$ is given by $\epsilon(\langle A \rangle) = \sigma/\sqrt{N_p}$, where $N_p = 300$ is the number of peaks of uncorrelated events. We have also included two more corrections: subtraction of the noise correlations from the APD dark counts [110] and the compensation of the slow long delay decay caused by the finite efficiency of the detectors and by the count rate of the APDs. Fig 4.6 shows the $g^{(2)}(0)$ values obtained and their error bars after applying this method. It corresponds to Fig 4.3 (a) in section 4.1.1.

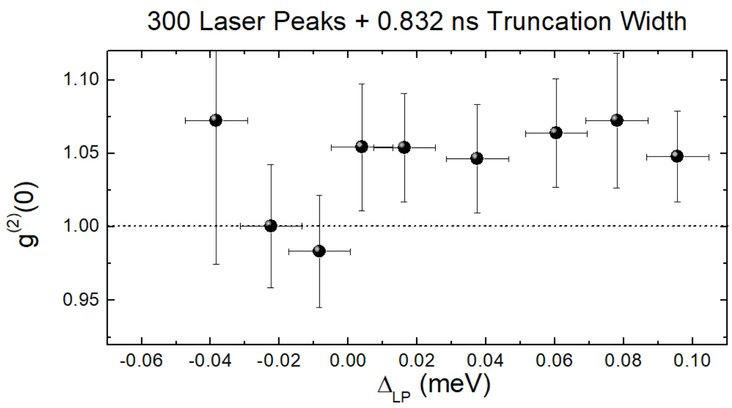

Figure 4.6: ***Extracted second order autocorrelation function at zero time delay.*** $g^{(2)}(0)$ *values extracted following the analysis protocol described.*

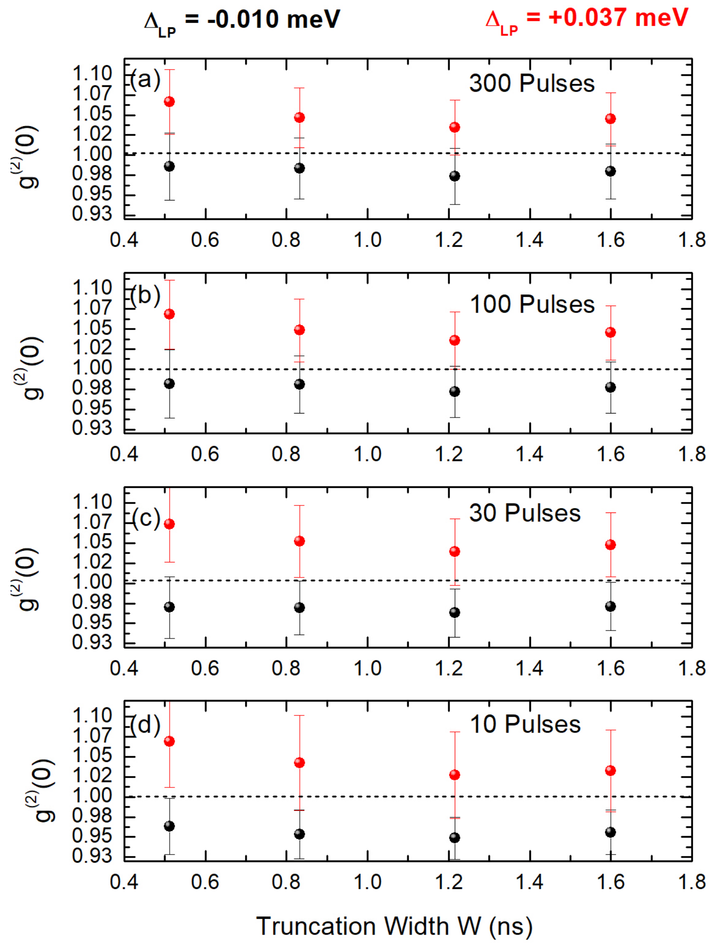

Figure 4.7: ***Sensitivity of the result on the analysis parameters.*** *Values obtained for* $g^{(2)}(0)$ *(at* Δ_{LP}*) = -0.010 meV and +0.037 meV in Fig 4.6), from analysis of the raw data, using W = {0.512,0.832,1.216,1.600} ns, and* n_p *= {300, 100,30,10} peaks.*

In order to check the robustness of our method, we analysed two values of $g^{(2)}(0)$ (Δ_{LP} = -0.010 meV and +0.037 meV in Fig 4.6), as a function of W and N_p, for W = 0.512 ns, 0.832 ns, 1.216 ns and 1.600 ns, and n_p = 300, 100, 30 and 10 peaks. Fig 4.7 shows the result: As expected, accounting for the maximum number of peaks, plus a truncation width W chosen within this time interval maximises the signal to noise ratio. Fig 4.8 shows raw photon correlation measurement, for both laser detunings until 11 consecutive correlated pulses.

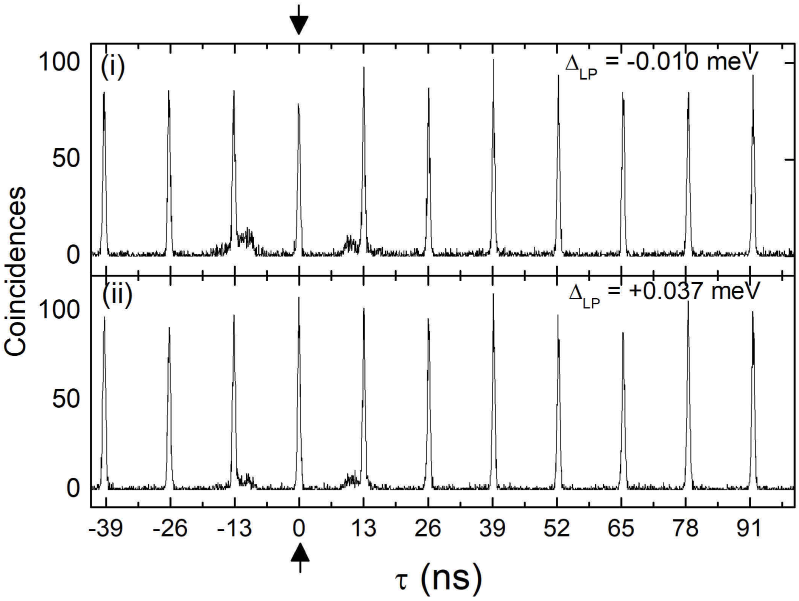

Figure 4.8: ***Raw photon correlation histograms.*** *(i) Raw photon correlation histogram from main text Figure 4.b with laser detuning Δ_{LP} = -0.010 meV until 11 consecutive correlated pulses. (ii) Raw photon correlation histogram from main text Figure 4.b with laser detuning Δ_{LP} = +0.037 meV until 11 consecutive correlated pulses. Arrows indicate the position of the zero delay peak.*

In summary, we have demonstrated the first indications of the quantum polariton blockade regime by the presence of small but distinct photon antibunching in a single QW microcavity system. Through the use of semi-integrated, fibre microcavities which tightly confine polariton through its photonic component, different cavity-exciton detunings of the lower polariton state could be studied. At each of these cavity-exciton detunings, several energies across the polariton transition were selected with a resonant modified pulsed laser with a pulse width approximately matching the polariton lifetime, with the photon correlations measured at each energy. At a cavity-exciton detuning of 1.11 meV, our best antibunching value of $g^{(2)}(0)$ = 0.93 ± 0.04 is achieved. To quantify and understand the dynamics occurring in the confined polariton system, numerical simulations of the experimental system are performed taking into account the pulsed nature of the excitation, and the experimental integration over all possible correlation times. These simulations are fitted to the experimental results, yielding and exciton-exciton interaction constant of $\hbar\omega_{NL}$ = 0.018 ± 0.010 meV, and exciton-exciton interaction strength of $\hbar\kappa$ = 0.076 ± 0.042 meV·μm^2 and a polariton-polariton interaction strength of $\hbar g_0$ = 0.020 ± 0.011 meV·μm^2. These photon correlation measurements were repeated in a second cavity, with similar findings to those found in the first measurements, however, with reduced uncertainty in the measurements, validating these results.

5

Emerging quantum correlations of non-resonantly excited polaritons

In this chapter, preliminary results on the observation of quantum correlations from non-resonantly driven microcavity polaritons are presented. In order to give an explanation of the observed correlations, a work-in-progress model for the system dynamics is introduced. It must be emphasised that the results presented in this chapter are still preliminary and subject to further investigation.

In the paper initially describing the polariton blockade regime [42], all discussions and simulations were given with resonant excitation of the LP transition. What was not discussed in this paper was the prospect of using non-resonant excitation of the system to create single photons. For QDs strongly coupled to photonic crystal cavities, quantum correlated photons can be easily produced by off-resonant pumping [111]. The strong nonlinear nature of the QD itself takes care of the discrete excitation nature of the system. For confined cavity polaritons with their relatively weak nonlinearity, the excitation through the reservoir is not one-by-one. This raises the question whether incoherent excitation can be used at all to create antibunched photons from LP polaritons. However, it turns out that by using a narrow-band optical filter it seems possible to get quantum correlated photons under off-resonant excitation. It seems that the filter in combination with the polariton-polariton interactions leads to sizeable quantum correlations - here we present preliminary photon correlation data under non-resonant excitation and a corresponding Master equation model that captures the relevant features. While the effect seems to be there, more measurements and more careful modelling are currently under way.

5.1 Photon correlations of spectrally filtered polariton photoluminescence

In order to intuitively understand the potential occurrence of quantum correlations from our off-resonantly driven polariton system, it is worth having a look into the case of the biexciton cascade in QDs. The typical cross-correlation function for the QD biexciton cascade [112] exhibits both antibunching and bunching. While the cross-correlation function is recorded as a function of delay time, it does contain a mapping between color and antibunching/bunching behavior. This idea is illustrated in Fig 5.1. In Fig 5.1 (a), the QD exciton-biexciton ladder for the neutral exciton is shown. Under two-photon excitation, the system exhibits a cascade effect as the biexciton decays into the neutral exciton state first, and from there down to the ground state. If the photoluminescence is spectrally filtered ($\Delta_{LP} = \omega_{X^0} - \omega_{filter}$) and the biexciton and exciton photons are used as a start/stop signal for two-colour cross-correlations, one obtains the typical antibunching/bunching signature for the biexciton cascade. This two-colour cross-correlation tells much about the system: If a red (biexciton) photon is detected first, it means that the biexciton has decayed and there is a high probability that a blue photon from the exciton decay will follow quickly thereafter. This implies that red (biexciton) photons are associated with bunching. If a blue (exciton) photon is detected first, the biexciton has likely already decayed and the system will need to be re-excited again. This results in a delay till the next red photon can be detected. Hence for blue (exciton) photons, antibunching will occur. The mapping between photon color and antibunching/bunching behavior is possible due to the fact that the QD system is highly nonlinear and the exciton/biexciton energies are well separated. Note that if the biexciton had higher energy than the exciton, the mapping between photon statistics and color would be reversed.

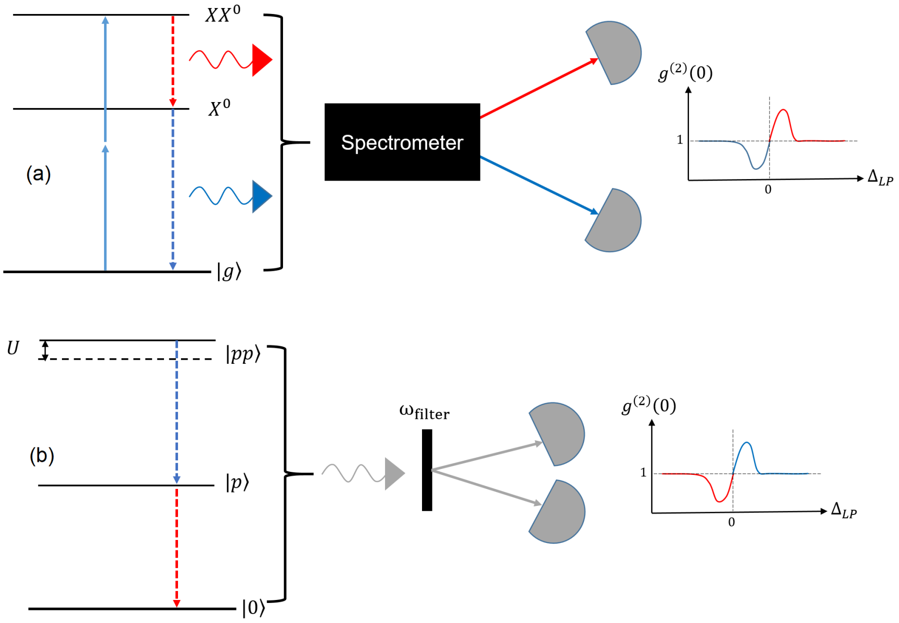

Figure 5.1: ***Biexciton cascade with two-colour correlations.*** ***(a)*** *The biexciton cascade with two-colour correlations where* $\Delta_{LP} = \omega_{LP} - \omega_{filter}$. *Note in this graph frequency is used, but in reality, this is actually* $g^{(2)}(\tau)$ *as a function of delay time. With the spectrometer providing the spatial filtering of the photoluminescence, bunching will occur on the red side of the neutral exciton transition, and antibunching on the blue side for the two-colour correlation shown in the graph on the RHS of* ***(a)****.* ***(b)*** *Polariton cascade with a monochromatic filter with centre frequency* ω_{filter}. *Due to the cascade nature of the process, photon antibunching is expected on the red-detuned of the neutral exciton, and photon bunching on the blue-detuned side.*

In principle, a similar cascading behavior should be observable for a polariton cascade. However, the polariton excitation ladder nonlinearity is weak, unlike the biexciton cascade - hence efficient photon filtering for cross-correlation measurements is not possible. Yet, as it turns out, by using a narrow-band filter and autocorrelation measurements, a similar antibunching/bunching behavior can be observed. The following hypothetical situation is illustrated in Fig 5.1 (b): here the energy ladder consists of the two-polariton and one-polariton state with the two transition energies only weakly separated. Now imagine that a photon red detuned from the LP transition is detected. Clearly, the probability of this photon coming from the lower of the two transitions in the cascade is higher. Therefore, a red photon indicates that the system is projected into the ground state and needs to be re-excited before another photon can be seen. Thus, a red photon leads to antibunching. The reverse is true for a blue photon; detecting a blue photon enhances the probability that this photon has been emitted on the higher lying transition. Hence the probability of seeing another photon right after from the lower transition is enhanced and the system exhibits bunching. Hence, relative to the LP resonance, we expect photons from the red side ($\Delta_{LP} < 0$) to exhibit antibunching, and blue photons ($\Delta_{LP} > 0$) to exhibit bunching (similar to what is seen in resonant excitation in the blockade case). In the experiment, we isolate photons according to their colour using a narrow-band optical filter. It is important to note that the selective filtering of photons to perform autocorrelation measurements of the LP resonance does not give immediately the same information about the system as the two-colour cross-correlation measurement used for the biexciton cascade. This is due to the mapping between delay time, photon energy and photon statistics behaviour [113]. In the case of autocorrelations measurements, only a single photon energy is measured in a given measurement, so some information about the system is not present. However, if the narrow-band optical filter is moved over several photon energies across the LP resonance, the same information about the system i.e. photon energy and photon statistics can be reconstructed.

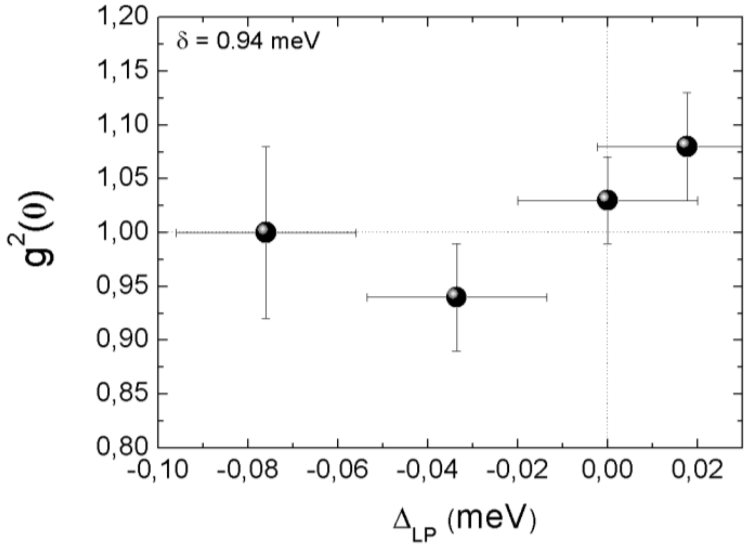

Figure 5.2: ***Non-resonant g$^{(2)}$(0) measurements as a function of filter-polariton detuning.*** *Measurements were taken at a cavity-exciton detuning of δ = 0.94 meV and show clear signs of antibunching when the filter is red detuned from the centre of the polariton transition. Photon bunching is also present when the filter is blue detuned, following similar behaviour to the resonant measurements.*

In order to measure photon correlations for non-resonantly excited microcavity polaritons, a similar setup was used as shown previously in Fig 3.2 with one key difference: now, spectral selection of the LP transition is done by filtering the emitted light from the cavity, rather than by resonantly exciting the LP transition. The spectral filtering is required as the photoluminescence light emitted by the cavity spans the entire LP transition due to the population of higher lying polariton states (see Fig 5.3). To perform the spectral filtering, we placed the Acton SP2750 spectrometer (previously used for laser pulse shaping) into the detection path of the experiment, before the HBT interferometer. Laser pulse shaping is no longer necessary as the LP mode is not directly excited and so spectral matching of the LP linewidth is not required. With the filtering afforded by the spectrometer that we are using (~25 pm), the LP mode can be selectively probed across the transition by changing the angle of the grating inside the spectrometer.

With the altered experimental setup, we performed photon correlations across the the LP transition at a cavity-exciton detuning of $\delta = 0.94$ meV and excited with a pulsed laser with centre wavelength of 1.553 eV, with a pulse width of ~6 ps. The resulting integrated coincidence plot of the photon correlation measurements is shown in Fig 5.2.

Clearly, there are deviations from the uncorrelated baseline of $g^{(2)}(0)$ =1 with $g^{(2)}(0)$<1 shown for negative values of Δ_{LP} and larger than 1 for Δ_{LP} ≥0. Interestingly, the non-trivial correlations indicate similar behaviour as was observed for the resonant measurements in chapter 4, with an antibunching of $g^{(2)}(0) = 0.93 \pm 0.06$. Error bars are calculated in the same way as was described in section 4.1.3. The quantum correlations observed in Fig 5.2 add validity to the hypothesis that quantum correlations can be observed under non-resonant excitation conditions. With no theoretical model available to quantify our results, no analysis could be performed on them. However, we have started to develop a theoretical model to describe our findings, with particular emphasis on the role of the exciton reservoir.

5.2 Spectrally filtered polariton photoluminescence

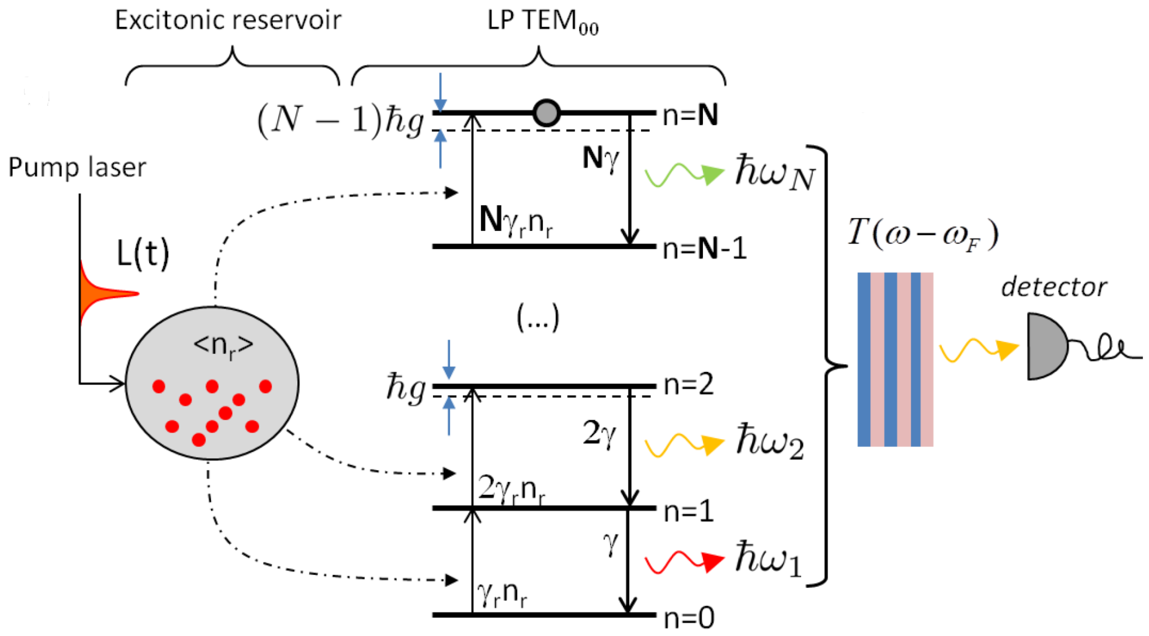

Figure 5.3: ***Spectrally filtered photoluminescence.*** *From left to right: the pump laser excites an incoherent long-lived excitonic population dubbed the 'excitonic reservoir'. This reservoir induces upward transitions in the polaritonic anharmonic excitation ladder. Downward transitions correspond to the emission of a photon in the detection channel. The emitted photons are frequency selected by a narrow band filter of transmission spectrum* $T(\omega-\omega_F)$ *prior to photodetection. L(t) is the pulsed laser excitation, <*n_r*> is the expectation value of the reservoir population,* γ_r *is the reservoir linewidth,* γ *is the polariton emission rate and g is the polariton-polariton interaction constant.*

In the work already presented in this thesis, polaritons are generated directly using a pulsed laser with a photon energy resonant with the polariton transition. If the excitation laser is changed to a higher photon energy, an incoherent population of long-lived excitons are formed, the so-called *excitonic reservoir*. The reservoir feeds the polariton states by incoherent, inelastic scattering via either phonons or mutual collisions as shown in Fig 5.3. With significant polariton-polariton interactions, the polariton transition energy blueshifts for increasing polariton number as more polaritons contribute to the interaction strength. The photoluminescence light that leaks out of the microcavity polariton system incorporates photons from all these transitions. If the PL light is passed through a narrow spectral filter with transmission spectrum $T(\omega-\omega_F)$, then due to the interactions that couple the emission frequency with the polariton number, the filter will increase or decrease the probability of detecting a photon.

Provided that the spectral filter linewidth γ_F is considerably smaller than the polariton emission linewidth, $\gamma_F \ll \gamma_{LP}$, non-trivial photon correlations are expected after the filter depending on the detuning of the filter with respect to the peak of the polariton emission and the features of the reservoir-cavity dynamics. This behaviour resembles that of Eqn 2.38 where the probability of photon detection increases as the cavity-laser detuning becomes positive. This is due to the driving laser approaching the two-photon resonance of the cavity.

The probability of exciting the two-photon resonance increases further as the linewidths of the single and two-photon transition begin to overlap. However, in this case, it is the single polariton and two-polariton transitions that overlap, as explained in Fig 5.1 (b).

In order to model the system theoretically in the off-resonant excitation regime, a Master equation approach is taken. In this particular Master equation, two Lindblad terms are used. The first one describes the polariton losses by photon leakage out of the cavity:

$$\hat{\mathcal{L}} = \gamma \left(b\rho b^{\dagger} - \frac{1}{2} b^{\dagger} b\rho - \frac{1}{2} \rho b^{\dagger} b \right) \tag{5.1}$$

Here, γ is the polariton linewidth, ρ is the intracavity polariton density matrix, and $b^{\dagger}, b$ are the polariton creation and annihilation operators. The other Lindblad term describes polariton pumping through the reservoir:

$$\hat{\mathcal{L}}_p\left(n_r\right) = \gamma_r n_r \left(b^{\dagger}\rho b - \frac{1}{2} b b^{\dagger} \rho - \frac{1}{2} \rho b b^{\dagger} \right) \tag{5.2}$$

where $n_r(t)$ is the time-dependent exciton reservoir population and γ_r is the reservoir linewidth. The Master equation for the system is then:

$$\dot{\rho} = -\frac{i}{\hbar}\left[\mathcal{H}, \rho\right] + \hat{\mathcal{L}} + \hat{\mathcal{L}}_r\left(n_r\right) \tag{5.3}$$

where $\mathcal{H}$ is the polariton Hamiltonian given in Eqn (2.25). In the simplest case, the exciton reservoir dynamics reads:

$$\dot{n}_r = L(t) - \gamma_r n_r \left(\bar{n} + 1\right) \tag{5.4}$$

Here, $L(t) = L_0\delta(t)$ is the pulsed laser excitation of the reservoir. It must be emphasised that the exact influence of the exciton reservoir is yet unclear at the time of writing this thesis. Nonetheless, several important questions can be asked: What is the magnitude of the noise induced by the reservoir?

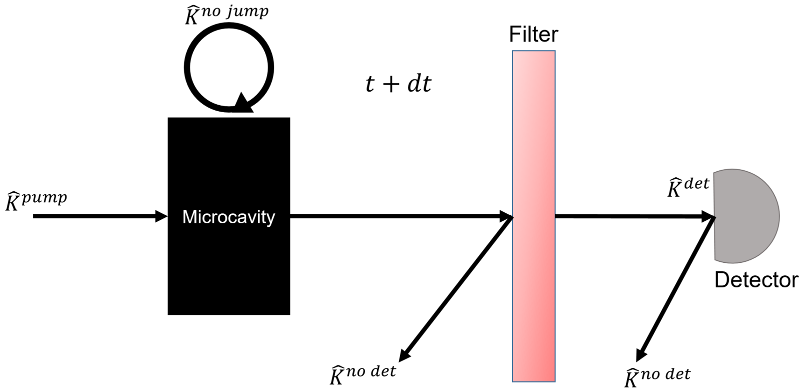

Figure 5.4: ***Quantum events for microcavity polaritons under non-resonant excitation.*** *There are four possible events for the system to evolve in a time interval* $t + dt$. $\hat{K}^{det}$ *involves a photon emission from the system which passes through the filter and is detected.* $\hat{K}^{no\ det}$ *involves an emission event, but the photon either is rejected by the filter or is not detected due to the quantum efficiency of the detector.* $\hat{K}^{pump}$ *involves the injection of a polariton into the system. Finally,* $\hat{K}^{no\ jump}$ *describes a no emission event. All these possibilities describe the system dynamics when placed in the Master equation.*

How large are the effective polariton-polariton interactions in the presence of the exciton reservoir and what are the reservoir contributions to the observed photon correlations? The answers to these questions determine the approach for simulating the system properly. For now, the simplest description is used for the reservoir to give an initial point from which to conduct further investigation and development of theory.

To find the corresponding photon statistics, the system is represented using four possible events that can occur in the system, which are described by so-called Kraus operators which define the probabilities of a certain event happening in a time interval $t + dt$. These events are graphically shown in Fig 5.4.

The first event is the emission of a photon which passes through the filter and is detected ($\hat{K}^{det}$). The second event is the emission of a photon which is not detected either due to rejection by the spectral filter or due to the finite efficiency of the detectors ($\hat{K}^{no\ det}$). Thirdly, no photon emission occurs ($\hat{K}^{no\ jump}$) and finally, the addition of a polariton in the cavity from the reservoir ($\hat{K}^{pump}$). These events defined by the Kraus operators can be used to 'unravel' the Master equation to yield the hidden dynamics of the system. The explicit formulation of the Kraus operators have not been included in this thesis as this theoretical work is outside the scope of this thesis and is still under active investigation.

With the Master equation given in Eqn (5.3), numerical simulations were carried out using experimental parameters which are shown in Fig 5.5.

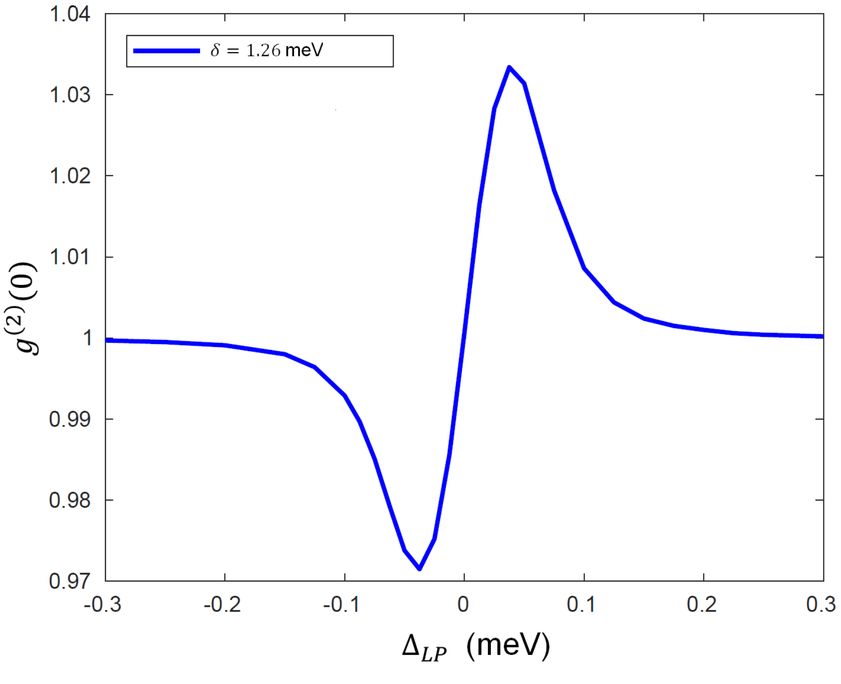

Figure 5.5: $g^{(2)}(0)$ ***under non-resonant excitation as a function of filter frequency-LP detuning.*** $g^{(2)}(0)$ *becomes antibunched on the red detuned side of the transition and bunched on the blue detuned side. This behaviour resembles what has been observed previously with the system under resonant excitation. Parameters:* $\omega_{nl} = 12\ \mu eV$*, input power = 12 pW, pulsewidth = 40 ps.*

Comparing these simulations to Fig 5.2, $g^{(2)}(0)$ follows the same trend as the filter frequency is scanned across the polariton transition. This is consistent with Eqn (2.38) where the position of the filter acts in the same way as the frequency selection with a resonant laser.

If the frequency selection is made on the lower energy (red detuned) side of the transition of the one-polariton state, there is a reduced probability of the detection of a photon. On the high energy (blue detuned) side, especially if the two-polariton linewidth is large, there is an increased probability of the detection of a photon.

It is clear that more simulations and deeper modelling are required to fully develop the concepts presented here, with emphasis on the contribution and role of the exciton reservoir on the system dynamics.

6

Conclusion

This thesis has reported the emergence of quantum correlations from a confined, fibre-based, microcavity polariton system under resonant excitation. Our results clearly demonstrate that the quantum regime for polariton-polariton interactions is achievable. Our results act as a door opener to a new field of research previously unattainable: quantum polaritonics. In this new field, concepts and ideas such as all-photonic quantum simulators which can model complex many-body systems seem potentially possible, with far reaching implications for the future. Yet, while we have opened the door to the field of quantum polaritonics with our work, we have only begun to scratch the surface. To move this new field forward and much deeper into the strongly interacting regime, improvements and advances in photonics, materials and excitonic engineering are needed.

Our fiber cavity approach introduces strong polariton-polariton interactions through tight optical confinement. This idea can be further expanded by continued engineering of the photonic part of the polariton wavefunction to increase confinement and thus, interactions. An immediate course of action that can be undertaken is to produce fibre mirrors with smaller radii of curvature. While CO_2 laser ablation does produce mirrors with exceptional smoothness and RoCs on the order of ~5-10 μm [51], to reach smaller RoCs, focused ion beam (FIB) milling could be used instead. RoCs less than 5 μm on fibres might be possible, as has been demonstrated with silica substrates [69]. Another idea that is being investigated at the time of writing this thesis is the use of etched lenses on the surface layer of the QW sample. Through the extension of the top GaAs capping layer on top of the QW, lenses can be etched onto the surface using FIB techniques. Matching the ROC of the lens to the fiber mirror ROC should lead to significantly tighter mode confinement by increasing the effective NA of the cavity mode. In the ideal case, the effective mode area at the position of the quantum well should be reduced by a factor $n^2 \approx 13$. Further, photonic crystal cavities (PCC) could be used to increase photonic confinement. These structures afford good optical quality and extremely small mode volumes. They have been used in the past with multiple QW samples [48]. However, one serious issue with photonic crystal cavities is the fact that the etched holes lead to increased polariton losses.

On the material engineering side, we found in our experiments that the QW sample presumably had too many DBR layers, which increased the chance of photon absorption.

While a higher number of layers increases the cavity finesse and Q-factor in theory, the increased number of layers likely reduced the photon count rate at the APDs, greatly reducing the efficiency of our correlation measurements. In the future, QW samples with less DBR layers will facilitate increased signal to the APDs, decreasing the integration time and enabling much faster integration, thereby also reducing the impact of drifts in the system. The QW linewidth is also another avenue for improvement. Our present sample is not at the limit of what is technically possible. If the QW is narrow enough compared to the collective vacuum Rabi splitting, then QW disorder can be largely eliminated, leading to a narrowing of the LP resonance which in turn should allow for a stronger blockade effect.

While GaAs has the strongest exciton nonlinearity of any known semiconductor system, other materials might open a different avenue for realising strong photon-photon interactions. In particular, the 2D transition metal dichalcogenide (TMD), mono-layer materials such as Molybdenum Disulfide (MoS_2) or Tungsten Diselenide (WSe_2) could provide a material platform in this direction [114]. While the excitons in these materials are extremely tightly bound and therefore have comparatively small interaction constants, the strong excitonic effects might lend themselves to excitonic engineering approaches, i.e. exploring excitonic resonances (biexciton) or higher-lying bound exciton complexes (Rydberg states) [115].

Another approach to excitonic engineering is provided by the use of indirect excitons to achieve the polariton blockade regime [43, 44]. The use of indirect excitons that have large dipole moments shows great promise; the double QW samples needed to create them could, in principle, be readily placed inside our existing fibre cavities. An alternative approach for enhancing interactions could also be the Feshbach blockade effect that exploits the QW biexciton state. In principle, our tunable fibre microcavities are ideal for observing this effect [45], however, GaAs might not be the best material to observe the effect, as opposed to the TMDs.

Another idea for producing antibunched light from a weakly nonlinear material system was put forward a few years ago. The idea is to use the phenomenon of quantum interference in the so-called unconventional polariton blockade [47]. In this proposal, the polaritons in adjacent cavities can tunnel between the cavities with a small nonlinearity present in one of them. The coupling between the cavities produces a quantum interference effect leading to polariton blockade. Unconventional blockade has been demonstrated for microwave systems and for QDs but not yet for polaritons. As part of the initial batch of fibre mirrors made for the work presented in this thesis, several multi-indentation fibres were also produced. It is speculated that the multiple indentations in close proximity to each other could provide a suitable platform to test the unconventional blockade concept. However, at time of writing this thesis, the corresponding experiments have yet to be performed.

In the last chapter of this thesis, correlation measurements showed that quantum correlations can in principle be achieved using non-resonant excitation of polaritons. Further investigation is clearly indicated both theoretically and experimentally. At the time of writing this thesis, efforts are already underway to improve the accuracy and linewidth of the filter by using fibre Bragg gratings (FBG) which can be precisely tuned and have a narrow transmission spectrum. In addition, the group recently acquired superconducting single-photon detectors (SSPDs) from Single Quantum with $> 90\%$ quantum efficiency and a time-resolution of around 14 ps. This should enable much faster integration and direct access to quantum correlations on short timescales and will clearly be a game changer for all the experiments planned.

References

[1] A. D. Greentree, C. Tahan, J. H. Cole, and L. C. L. Hollenberg. *Quantum phase transitions of light*. Nature Physics **2**, 856 EP (2006). Article, URL https://doi.org/10.1038/nphys466.

[2] J. Kasprzak, M. Richard, S. Kundermann, A. Baas, J. K. P. Jeambrun, F. Marchetti, M. Szymanska, R. Andre, J. Staehli, V. Savona, P. Littlewood, B. Deveaud, and L. S.Dang. *Bose-einstein condensation of exciton polaritons*. Nature **443**, 409 (2006).

[3] A. Amo, J. Lefrère, S. Pigeon, C. Adrados, C. Ciuti, I. Carusotto, R. Houdré, E. Giacobino, and A. Bramati. *Superfluidity of polaritons in semiconductor microcavities*. Nature Physics **5**, 805 EP (2009). URL http://dx.doi.org/10.1038/nphys1364.

[4] L. Ferrier, E. Wertz, R. Johne, D. D. Solnyshkov, P. Senellart, I. Sagnes, A. Lemaître, G. Malpuech, and J. Bloch. *Interactions in confined polariton condensates*. Phys. Rev. Lett. **106**, 126401 (2011). URL https://link.aps.org/doi/10.1103/PhysRevLett.106.126401.

[5] O. E. Daïf, A. Baas, T. Guillet, J.-P. Brantut, R. I. Kaitouni, J. L. Staehli, F. Morier-Genoud, and B. Deveaud. *Polariton quantum boxes in semiconductor microcavities*. Applied Physics Letters **88**(6), 061105 (2006). https://doi.org/10.1063/1.2172409, URL https://doi.org/10.1063/1.2172409.

[6] K. Hennessy, A. Badolato, M. Atatüre, A. Imamoglu, and E. Hu. *Photonic crystal nanocavities positioned and tuned for cavity-qed*. In *Integrated Photonics Research and Applications/Nanophotonics*, p. NWA6 (Optical Society of America, 2006). URL http://www.osapublishing.org/abstract.cfm?URI=NANO-2006-NWA6.

[7] X. Liu, J. Gao, J. Gao, H. Yang, X. Wang, T. Wang, Z. Shen, Z. Liu, H. Liu, J. Zhang, Z. Li, Y. Wang, and Q. Li. *Microcavity electrodynamics of hybrid surface plasmon polariton modes in high-quality multilayer trench gratings*. Light: Science & Applications **7**(1), 14 (2018). URL https://doi.org/10.1038/s41377-018-0009-x.

[8] B. Besga, C. Vaneph, J. Reichel, J. Estève, A. Reinhard, J. Miguel-Sánchez, A. m. c. Imamoğlu, and T. Volz. *Polariton boxes in a tunable fiber cavity*. Phys. Rev. Applied **3**, 014008 (2015). URL https://link.aps.org/doi/10.1103/PhysRevApplied.3.014008.

[9] T. G. Walker. *Strongly interacting photons*. Nature **488**, 39 EP (2012). URL https://doi.org/10.1038/nature11384.

[10] Y. O. Dudin and A. Kuzmich. *Strongly interacting rydberg excitations of a cold atomic gas*. Science **336**(6083), 887 (2012). https://science.sciencemag.org/content/336/6083/887.full.pdf, URL https://science.sciencemag.org/content/336/6083/887.

[11] M. H. Anderson, J. R. Ensher, M. R. Matthews, C. E. Wieman, and E. A. Cornell. *Observation of bose-einstein condensation in a dilute atomic vapor*. Science **269**(5221), 198 (1995). http://science.sciencemag.org/content/269/5221/198.full.pdf, URL http://science.sciencemag.org/content/269/5221/198.

[12] M. J. Hartmann, F. G. S. L. Brandão, and M. B. Plenio. *Strongly interacting polaritons in coupled arrays of cavities*. Nature Physics **2**, 849 EP (2006). Article, URL https://doi.org/10.1038/nphys462.

[13] M. P. A. Fisher, P. B. Weichman, G. Grinstein, and D. S. Fisher. *Boson localization and the superfluid-insulator transition*. Phys. Rev. B **40**, 546 (1989). URL https://link.aps.org/doi/10.1103/PhysRevB.40.546.

[14] D. G. Angelakis, M. F. Santos, and S. Bose. *Photon-blockade-induced mott transitions and xy spin models in coupled cavity arrays*. Phys. Rev. A **76**, 031805 (2007). URL https://link.aps.org/doi/10.1103/PhysRevA.76.031805.

[15] N. G. Berloff, M. Silva, K. Kalinin, A. Askitopoulos, J. D. Töpfer, P. Cilibrizzi, W. Langbein, and P. G. Lagoudakis. *Realizing the classical XY Hamiltonian in polariton simulators*. Nat. Mater. **16**, 1120 (2017).

[16] M. Girardeau. *Relationship between systems of impenetrable bosons and fermions in one dimension*. Journal of Mathematical Physics **1**(6), 516 (1960). https://doi.org/10.1063/1.1703687, URL https://doi.org/10.1063/1.1703687.

[17] D. E. Chang, V. Gritsev, G. Morigi, V. Vuletic, M. D. Lukin, and E. A. Demler. *Crystallization of strongly interacting photons in a nonlinear optical fibre*. Nature Physics **4**, 884 EP (2008). Article, URL https://doi.org/10.1038/nphys1074.

[18] J. I. Cirac and P. Zoller. *Goals and opportunities in quantum simulation*. Nature Physics **8**, 264 EP (2012). URL https://doi.org/10.1038/nphys2275.

[19] E. T. Jaynes and F. W. Cummings. *Comparison of quantum and semiclassical radiation theories with application to the beam maser*. Proceedings of the IEEE **51**(1), 89 (1963).

[20] A. Imamoḡlu, H. Schmidt, G. Woods, and M. Deutsch. *Strongly interacting photons in a nonlinear cavity*. Phys. Rev. Lett. **79**, 1467 (1997). URL https://link.aps.org/doi/10.1103/PhysRevLett.79.1467.

[21] K. M. Birnbaum, A. Boca, R. Miller, A. D. Boozer, T. E. Northup, and H. J. Kimble. *Photon blockade in an optical cavity with one trapped atom*. Nature **436**(7047) (2005).

[22] A. Reinhard, T. Volz, M. Winger, A. Badolato, K. J. Hennessy, E. L. Hu, and A. Imamoglu. *Strongly correlated photons on a chip*. Nature Photonics **6**(2) (2011).

[23] T. Sattler, E. Peinke, J. Bleuse, J. Claudon, W. L. Vos, and J. M. GÃľrard. *Cavity switching: A novel resource for solid-state quantum optics*. In *2017 19th International Conference on Transparent Optical Networks (ICTON)*, pp. 1–4 (2017).

[24] T. Volz, A. Reinhard, M. Winger, A. Badolato, K. J. Hennessy, E. L. Hu, and A. Imamoglu. *Ultrafast all-optical switching by single photons*. Nature Photonics **6**, 605 EP (2012). URL https://doi.org/10.1038/nphoton.2012.181.

[25] D. Englund, A. Majumdar, M. Bajcsy, A. Faraon, P. Petroff, and J. Vučković. *Ultrafast photon-photon interaction in a strongly coupled quantum dot-cavity system*. Phys. Rev. Lett. **108**, 093604 (2012). URL https://link.aps.org/doi/10.1103/PhysRevLett.108.093604.

[26] R. Bose, D. Sridharan, H. Kim, G. S. Solomon, and E. Waks. *Low-photon-number optical switching with a single quantum dot coupled to a photonic crystal cavity*. Phys. Rev. Lett. **108**, 227402 (2012). URL https://link.aps.org/doi/10.1103/PhysRevLett.108.227402.

[27] J. Hwang, M. Pototschnig, R. Lettow, G. Zumofen, A. Renn, S. Götzinger, and V. Sandoghdar. *A single-molecule optical transistor*. Nature **460**, 76 EP (2009). URL https://doi.org/10.1038/nature08134.

[28] H. Kim, R. Bose, T. C. Shen, G. S. Solomon, and E. Waks. *A quantum logic gate between a solid-state quantum bit and a photon*. Nature Photonics **7**, 373 EP (2013). URL https://doi.org/10.1038/nphoton.2013.48.

[29] F. Deppe, M. Mariantoni, E. P. Menzel, A. Marx, S. Saito, K. Kakuyanagi, H. Tanaka, T. Meno, K. Semba, H. Takayanagi, E. Solano, and R. Gross. *Two-photon probe of the jaynes-cummings model and controlled symmetry breaking in circuit qed*. Nature Physics **4**, 686 EP (2008). URL https://doi.org/10.1038/nphys1016.

[30] R. Ma, B. Saxberg, C. Owens, N. Leung, Y. Lu, J. Simon, and D. I. Schuster. *A dissipatively stabilized mott insulator of photons*. Nature **566**(7742), 51 (2019). URL https://doi.org/10.1038/s41586-019-0897-9.

[31] H. Lan and Y. Ding. *Ordering, positioning and uniformity of quantum dot arrays*. Nano Today **7**(2), 94 (2012). URL http://www.sciencedirect.com/science/article/pii/S1748013212000242.

[32] C. Weisbuch, M. Nishioka, A. Ishikawa, and Y. Arakawa. *Observation of the coupled exciton-photon mode splitting in a semiconductor quantum microcavity*. Phys. Rev. Lett. **69**, 3314 (1992). URL https://link.aps.org/doi/10.1103/PhysRevLett.69.3314.

[33] A. Imamoglu, R. J. Ram, S. Pau, and Y. Yamamoto. *Nonequilibrium condensates and lasers without inversion: Exciton-polariton lasers*. Phys. Rev. A **53**, 4250 (1996). URL https://link.aps.org/doi/10.1103/PhysRevA.53.4250.

[34] G. Tosi, G. Christmann, N. G. Berloff, P. Tsotsis, T. Gao, Z. Hatzopoulos, P. G. Savvidis, and J. J. Baumberg. *Sculpting oscillators with light within a nonlinear quantum fluid*. Nature Physics **8**, 190 EP (2012). URL https://doi.org/10.1038/nphys2182.

[35] D. Gerace and I. Carusotto. *Analog hawking radiation from an acoustic black hole in a flowing polariton superfluid*. Phys. Rev. B **86**, 144505 (2012). URL https://link.aps.org/doi/10.1103/PhysRevB.86.144505.

[36] O. Bleu, D. D. Solnyshkov, and G. Malpuech. *Interacting quantum fluid in a polariton chern insulator*. Phys. Rev. B **93**, 085438 (2016). URL https://link.aps.org/doi/10.1103/PhysRevB.93.085438.

[37] I. Carusotto and C. Ciuti. *Probing microcavity polariton superfluidity through resonant rayleigh scattering*. Phys. Rev. Lett. **93**, 166401 (2004). URL https://link.aps.org/doi/10.1103/PhysRevLett.93.166401.

[38] G. Nardin, G. Grosso, Y. Léger, B. Pietka, F. Morier-Genoud, and B. Deveaud-Plédran. *Hydrodynamic nucleation of quantized vortex pairs in a polariton quantum fluid*. Nature Physics **7**, 635 EP (2011). Article, URL https://doi.org/10.1038/nphys1959.

[39] D. Sanvitto, S. Pigeon, A. Amo, D. Ballarini, M. De Giorgi, I. Carusotto, R. Hivet, F. Pisanello, V. G. Sala, P. S. S. Guimaraes, R. Houdré, E. Giacobino, C. Ciuti, A. Bramati, and G. Gigli. *All-optical control of the quantum flow of a polariton condensate*. Nature Photonics **5**, 610 EP (2011). URL https://doi.org/10.1038/nphoton.2011.211.

[40] K. G. Lagoudakis, T. Ostatnický, A. V. Kavokin, Y. G. Rubo, R. André, and B. Deveaud-Plédran. *Observation of half-quantum vortices in an exciton-polariton condensate*. Science **326**(5955), 974 (2009). http://science.sciencemag.org/content/326/5955/974.full.pdf, URL http://science.sciencemag.org/content/326/5955/974.

[41] A. Amo, S. Pigeon, D. Sanvitto, V. G. Sala, R. Hivet, I. Carusotto, F. Pisanello, G. Leménager, R. Houdré, E. Giacobino, C. Ciuti, and A. Bramati. *Polariton superfluids reveal quantum hydrodynamic solitons*. Science **332**(6034), 1167 (2011). http://science.sciencemag.org/content/332/6034/1167.full.pdf, URL http://science.sciencemag.org/content/332/6034/1167.

[42] A. Verger, C. Ciuti, and I. Carusotto. *Polariton quantum blockade in a photonic dot*. Phys. Rev. B **73**, 193306 (2006). URL https://link.aps.org/doi/10.1103/PhysRevB.73.193306.

[43] E. Togan, H.-T. Lim, S. Faelt, W. Wegscheider, and A. Imamoglu. *Strong interactions between dipolar polaritons* (2018).

[44] T. Byrnes, G. V. Kolmakov, R. Y. Kezerashvili, and Y. Yamamoto. *Effective interaction and condensation of dipolaritons in coupled quantum wells*. Phys. Rev. B **90**, 125314 (2014). URL https://link.aps.org/doi/10.1103/PhysRevB.90.125314.

[45] I. Carusotto, T. Volz, and A. Imamoĝlú. *Feshbach blockade: Single-photon nonlinear optics using resonantly enhanced cavity polariton scattering from biexciton states*. EPL **90**(3), p1 (2010).

[46] J. M. Hutson. *Feshbach resonances in ultracold atomic and molecular collisions: threshold behaviour and suppression of poles in scattering lengths*. New Journal of Physics **9**(5), 152 (2007). URL https://doi.org/10.1088%2F1367-2630%2F9%2F5%2F152.

[47] T. C. H. Liew and V. Savona. *Single photons from coupled quantum modes*. Phys. Rev. Lett. **104**, 183601 (2010). URL https://link.aps.org/doi/10.1103/PhysRevLett.104.183601.

[48] S. Azzini, D. Gerace, M. Galli, I. Sagnes, R. Braive, A. Lemaítre, J. Bloch, and D. Bajoni. *Ultra-low threshold polariton lasing in photonic crystal cavities*. Applied Physics Letters **99**(11), 111106 (2011). https://doi.org/10.1063/1.3638469, URL https://doi.org/10.1063/1.3638469.

[49] C. Grossmann, C. Coulson, G. Christmann, I. Farrer, H. E. Beere, D. A. Ritchie, and J. J. Baumberg. *Tuneable polaritonics at room temperature with strongly coupled tamm plasmon polaritons in metal/air-gap microcavities*. Applied Physics Letters **98**(23), 231105 (2011). https://doi.org/10.1063/1.3597304, URL https://doi.org/10.1063/1.3597304.

[50] D. Hunger, T. Steinmetz, Y. Colombe, C. Deutsch, T. W. Hansch, and J. Reichel. *A fiber fabry pérot cavity with high finesse*. New Journal of Physics **12**(6), 065038 (2010). URL http://stacks.iop.org/1367-2630/12/i=6/a=065038.

[51] A. Muller, E. B. Flagg, J. R. Lawall, and G. S. Solomon. *Ultrahigh-finesse, low-mode-volume fabry perot microcavity*. Opt. Lett. **35**(13), 2293 (2010). URL http://ol.osa.org/abstract.cfm?URI=ol-35-13-2293.

[52] A. Delteil, T. Fink, A. Schade, S. Höfling, C. Schneider, and A. Imamoglu. *Towards polariton blockade of confined exciton-polaritons*. Nature Materials **18**(3), 219 (2019). URL https://doi.org/10.1038/s41563-019-0282-y.

[53] C. Kittel (John Wiley and Sons, Inc), 8 ed.

[54] E. Khramtsov, P. Belov, P. S. Grigoryev, I. Ignatiev, S. Verbin, S. A. Eliseev, Y. Efimov, V. A. Lovtcius, V. V. Petrov, and S. Yakovlev. *Excitons in square quantum wells: microscopic modeling and experiment* **119** (2015).

[55] B. Laikhtman. *Are excitons really bosons?* Journal of Physics: Condensed Matter **19**(29), 295214 (2007). URL http://stacks.iop.org/0953-8984/19/i=29/a=295214.

[56] A. Kogar, M. S. Rak, S. Vig, A. A. Husain, F. Flicker, Y. I. Joe, L. Venema, G. J. MacDougall, T. C. Chiang, E. Fradkin, J. van Wezel, and P. Abbamonte. *Signatures of exciton condensation in a transition metal dichalcogenide*. Science **358**(6368), 1314 (2017). http://science.sciencemag.org/content/358/6368/1314.full.pdf, URL http://science.sciencemag.org/content/358/6368/1314.

[57] T. Usui. *Excitations in a high density electron gas. 1*. Progress of Theoretical Physics **23**(5), 787 (1960). /oup/backfile/content_public/journal/ptp/23/5/10.1143/ptp.23.787/2/23-5-787.pdf, URL http://dx.doi.org/10.1143/PTP.23.787.

[58] E. Hanamura and H. Haug. *Condensation effects of excitons*. Physics Reports **33**(4), 209 (1977). URL http://www.sciencedirect.com/science/article/pii/0370157377900126.

[59] S. Ben-Tabou de Leon and B. Laikhtman. *Exciton-exciton interactions in quantum wells: Optical properties and energy and spin relaxation*. Phys. Rev. B **63**, 125306 (2001). URL https://link.aps.org/doi/10.1103/PhysRevB.63.125306.

[60] C. Ciuti, V. Savona, C. Piermarocchi, A. Quattropani, and P. Schwendimann. *Role of the exchange of carriers in elastic exciton-exciton scattering in quantum wells*. Phys. Rev. B **58**, 7926 (1998). URL https://link.aps.org/doi/10.1103/PhysRevB.58.7926.

[61] M. Combescot, O. Betbeder-Matibet, and R. Combescot. *Exciton-exciton scattering: Composite boson versus elementary boson*. Phys. Rev. B **75**, 174305 (2007). URL https://link.aps.org/doi/10.1103/PhysRevB.75.174305.

[62] J. J. Hopfield. *Theory of the contribution of excitons to the complex dielectric constant of crystals*. Phys. Rev. **112**, 1555 (1958). URL https://link.aps.org/doi/10.1103/PhysRev.112.1555.

[63] A. Amo, J. Lefrere, S. Pigeon, C. Adrados, C. Ciuti, I. Carusotto, R. Houdre, E. Giacobino, and A. Bramati. *Superuidity of polaritons in semi-conductor microcavities*. Nature Physics **5**, 805 (2009).

[64] H. Deng, H. Haug, and Y. Yamamoto. *Exciton-polariton bose-einstein condensation*. Rev. Mod. Phys. **82**, 1489 (2010). URL https://link.aps.org/doi/10.1103/RevModPhys.82.1489.

[65] V. Savona. *Linear optical properties of semiconductor microcavities with embedded quantum wells*. In H. Benisty, C. Weisbuch, É. Polytechnique, J.-M. Gérard, R. Houdré, and J. Rarity, eds., *Confined Photon Systems*, pp. 173–242 (Springer Berlin Heidelberg, Berlin, Heidelberg, 1999).

[66] S. Reitzenstein, C. Hofmann, A. Gorbunov, M. StrauB, S. H. Kwon, C. Schneider, A. Löffler, S. Höfling, M. Kamp, and A. Forchel. *Alas/gaas micropillar cavities with quality factors exceeding 150.000*. Applied Physics Letters **90**(25), 251109 (2007). https://doi.org/10.1063/1.2749862, URL https://doi.org/10.1063/1.2749862.

[67] K. J. Vahala. *Optical microcavities*. Nature **424**, 839 EP (2003). URL https://doi.org/10.1038/nature01939.

[68] B. Besga. *Coherent control with polaritons*. Lecture notes (2014).

[69] S. Dufferwiel, F. Fras, A. Trichet, P. M. Walker, F. Li, L. Giriunas, M. N. Makhonin, L. R. Wilson, J. M. Smith, E. Clarke, M. S. Skolnick, and D. N. Krizhanovskii. *Strong exciton-photon coupling in open semiconductor microcavities*. Applied Physics Letters **104**(19), 192107 (2014). https://doi.org/10.1063/1.4878504, URL https://doi.org/10.1063/1.4878504.

[70] C. Ciuti, P. Schwendimann, and A. Quattropani. *Theory of polariton parametric interactions in semiconductor microcavities*. Semiconductor Science and Technology **18**(10), S279 (2003). URL https://doi.org/10.1088%2F0268-1242%2F18%2F10%2F301.

[71] Y. Sun, Y. Yoon, M. Steger, G. Liu, L. N. Pfeiffer, K. West, D. W. Snoke, and K. A. Nelson. *Direct measurement of polariton-polariton interaction strength*. Nature Physics **13**, 870 (2017).

[72] I. Carusotto and C. Ciuti. *Quantum fluids of light*. Rev. Mod. Phys. **85**, 299 (2013). URL https://link.aps.org/doi/10.1103/RevModPhys.85.299.

[73] T. Jacqmin, I. Carusotto, I. Sagnes, M. Abbarchi, D. D. Solnyshkov, G. Malpuech, E. Galopin, A. Lemaître, J. Bloch, and A. Amo. *Direct observation of dirac cones and a flatband in a honeycomb lattice for polaritons*. Phys. Rev. Lett. **112**, 116402 (2014).

[74] F. Baboux, L. Ge, T. Jacqmin, M. Biondi, E. Galopin, A. Lemaître, L. Le Gratiet, I. Sagnes, S. Schmidt, H. E. Türeci, A. Amo, and J. Bloch. *Bosonic condensation and disorder-induced localization in a flat band*. Phys. Rev. Lett. **116**, 066402 (2016).

[75] G. Dagvadorj, J. M. Fellows, S. Matyjaśkiewicz, F. M. Marchetti, I. Carusotto, and M. H. Szymańska. *Nonequilibrium phase transition in a two-dimensional driven open quantum system*. Phys. Rev. X **5**, 041028 (2015).

[76] S. Klembt, P. Stepanov, T. Klein, A. Minguzzi, and M. Richard. *Thermal decoherence of a nonequilibrium polariton quantum fluid*. Phys Rev Lett **120**, 035301 (2018).

[77] E. Estrecho, T. Gao, N. Bobrovska, D. Comber-Todd, M. Fraser, M. Steger, K. West, L. N. Pfeiffer, J. Levinsen, M. M. Parish, T. C. H. Liew, M. Matuszewski, D. W. Snoke, A. G. Truscott, and E. Ostrovskaya. *Measurement of polariton-polariton interaction strength in the thomas-fermi regime of polariton condensation* (2018).

[78] M. Pieczarka, M. Boozarjmehr, E. Estrecho, Y. Yoon, M. Steger, K. West, L. Pfeiffer, K. A. Nelson, D. Snoke, A. G. Truscott, and E. Ostrovskaya. *Effect of optically-induced potential on the energy of trapped exciton-polaritons below the condensation threshold* (2018).

[79] A. J. Hoffman, S. J. Srinivasan, S. Schmidt, L. Spietz, J. Aumentado, H. E. Türeci, and A. A. Houck. *Dispersive photon blockade in a superconducting circuit*. Phys. Rev. Lett. **107**, 053602 (2011). URL https://link.aps.org/doi/10.1103/PhysRevLett.107.053602.

[80] *Preface*. Semiconductor Science and Technology **18**(10) (2003). URL http://stacks.iop.org/0268-1242/18/i=10/a=000.

[81] I. Carusotto and C. Ciuti. *Probing microcavity polariton superfluidity through resonant rayleigh scattering*. Phys. Rev. Lett. **93**, 166401 (2004). URL https://link.aps.org/doi/10.1103/PhysRevLett.93.166401.

[82] S. Swain. *Master equation derivation of quantum regression theorem*. Journal of Physics A: Mathematical and General **14**(10), 2577 (1981). URL http://stacks.iop.org/0305-4470/14/i=10/a=013.

[83] S. Ferretti and D. Gerace. *Single-photon nonlinear optics with kerr-type nanostructured materials*. Phys. Rev. B **85**, 033303 (2012). URL https://link.aps.org/doi/10.1103/PhysRevB.85.033303.

[84] L. Ferrier, E. Wertz, R. Johne, D. D. Solnyshkov, P. Senellart, I. Sagnes, A. Lemaître, G. Malpuech, and J. Bloch. *Interactions in confined polariton condensates*. Phys. Rev. Lett. **106**, 126401 (2011). URL https://link.aps.org/doi/10.1103/PhysRevLett.106.126401.

[85] A. Reinhard, T. Volz, M. Winger, A. Badolato, K. J. Hennessy, E. L. Hu, and A. Imamoglu. *Strongly correlated photons on a chip*. Nature Photonics **6**, 93 EP (2011). URL http://dx.doi.org/10.1038/nphoton.2011.321.

[86] A. Wood, X. Vidal, G. Muñoz-Matutano, and T. Volz. *Non-invasive zero-delay time calibration of hanbury-brown and twiss interferometers*. Measurement **137**, 562 (2019). URL http://www.sciencedirect.com/science/article/pii/S0263224119300880.

[87] G. Muñoz-Matutano, A. Wood, M. Johnsson, X. Vidal, B. Q. Baragiola, A. Reinhard, A. Lemaître, J. Bloch, A. Amo, G. Nogues, B. Besga, M. Richard, and T. Volz. *Emergence of quantum correlations from interacting fibre-cavity polaritons*. Nature Materials **18**(3), 213 (2019). URL https://doi.org/10.1038/s41563-019-0281-z.

[88] D. Najer, M. Renggli, D. Riedel, S. Starosielec, and R. J. Warburton. *Fabrication of mirror templates in silica with micron-sized radii of curvature*. Applied Physics Letters **110**(1), 011101 (2017). https://doi.org/10.1063/1.4973458, URL https://doi.org/10.1063/1.4973458.

[89] C. Deutsch. *High finesse Fabry-Pérot resonators: production, characterisation and applicatiosn.* Ph.D. thesis, Ludwig-Maximilians Universität München (2008).

[90] S. Gehrsitz, F. K. Reinhart, C. Gourgon, N. Herres, A. Vonlanthen, and H. Sigg. *The refractive index of* $Al_xGa_{1x}As$ *below the band gap: Accurate determination and empirical modeling*. Journal of Applied Physics **87**(11), 7825 (2000).

[91] T. J. Bright, J. I. Watjen, Z. M. Zhang, C. Muratore, A. A. Voevodin, D. I. Koukis, D. B. Tanner, and D. J. Arenas. *Infrared optical properties of amorphous and nanocrystalline* Ta_2O_5 *thin films*. Journal of Applied Physics **114**(8), 083515 (2013).

[92] L. Gao, F. Lemarchand, and M. Lequime. *Refractive index determination of* SiO_2 *layer in the uv/vis/nir range: spectrophotometric reverse engineering on single and bi-layer designs*. Journal of the European Optical Society - Rapid publications **8**(0) (2013).

[93] T. Fink, A. Schade, S. Höfling, C. Schneider, and A. Imamoğlu. *Signatures of a dissipative phase transition in photon correlation measurements*. Nat. Phys. **First Online, 11.12.2017** (2017).

[94] B. Deveaud, L. Kappei, J. Berney, F. Morier-Genoud, M. Portella-Oberli, J. Szczytko, and C. Piermarocchi. *Excitonic effects in the luminescence of quantum wells*. Chem. Phys. **318**, 104 (2005).

[95] G. Muñoz-Matutano, B. Alén, J. Martínez-Pastor, L. Seravalli, P. Frigeri, and S. Franchi. *Selective optical pumping of charged excitons in unintentionally doped inas quantum dots*. Nanotechnology **19**, 145711 (2008).

[96] B. Sermage, S. Long, I. Abram, J. Y. Marzin, J. Bloch, R. Planel, and V. Thierry-Mieg. *Time-resolved spontaneous emission of excitons in a microcavity: Behavior of the individual exciton-photon mixed states*. Phys. Rev. B **53**, 16516 (1996). URL https://link.aps.org/doi/10.1103/PhysRevB.53.16516.

[97] R. Hanbury Brown. *A Test of a New Type of Stellar Interferometer on Sirius*. nat **178**, 1046 (1956).

[98] R. E. P. Kapusta, M. Wahl. *Advanced Photon Counting. Applications, Methods, Instrumentation*, vol. 15 (Springer International Publishing, 2015).

[99] B. Piccione, X. Jiang, and M. Itzler. *Spatial modeling of optical crosstalk in InGaAsP Geiger-mode APD focal plane arrays*. Opt. Express **24**(10), 10635 (2016). URL http://www.opticsexpress.org/abstract.cfm?URI=oe-24-10-10635.

[100] I. Rech, A. Ingargiola, R. Spinelli, I. Labanca, S. Marangoni, M. Ghioni, and S. Cova. *A new approach to optical crosstalk modeling in single-photon avalanche diodes*. IEEE Photonics Technology Letters **20**(5), 330 (2008).

[101] R. D. Younger, K. A. McIntosh, J. W. Chludzinski, D. C. Oakley, L. J. Mahoney, J. E. Funk, J. P. Donnelly, and S. Verghese. *Crosstalk Analysis of Integrated Geiger-mode Avalanche Photodiode Focal Plane Arrays*, vol. 7320 (Proc. of SPIE, 2009).

[102] B. F. Aull, D. R. Schuette, D. J. Young, D. M. Craig, B. J. Felton, and K. Warner. *A study of crosstalk in a* 256×256 *photon counting imager based on silicon Geiger-mode avalanche photodiodes*. IEEE Sensors Journal **15**(4), 2123 (2015).

[103] D. A. Kalashnikov, S.-H. Tan, and L. A. Krivitsky. *Crosstalk calibration of multi-pixel photon counters using coherent states*. Opt. Express **20**, 5044 (2012). URL http://www.opticsexpress.org/abstract.cfm?URI=oe-20-5-5044.

[104] C. Zinoni. *Optical characterisation of single quantum dots emitting at 1300 nm* (2007). Ècole polytechnique fèdèrale de Lausanne EPFL.

[105] W. Becker. *Advanced Time-Correlated Single Photon Counting Techniques* (Springer-Verlag, 2005).

[106] T. Huang, J. Shaom, X. Wang, L. Xiao, and S. Jia. *Photon emission characteristics of avalanche photodiodes*. Optical Engineering **44**(7), 074001 (2005). URL http://dx.doi.org/10.1117/1.1950087.

[107] G. Muñoz-Matutano, D. Barrera, C. R. Fernández-Pousa, R. Chulia-Jordan, L. Seravalli, G. Trevisi, P. Frigeri, S. Sales, and J. Martínez-Pastor. *All-optical fiber Hanbury Brown and Twiss interferometer to study 1300 nm single photon emission of a metamorphic inas quantum dot*. Sci. Rep **6**, 27214 (2016). URL http://dx.doi.org/10.1038/srep27214.

[108] P. M. Walker, L. Tinkler, B. Royall, D. V. Skryabin, I. Farrer, D. A. Ritchie, M. S. Skolnick, and D. N. Krizhanovskii. *Dark solitons in high velocity waveguide polariton fluids*. Phys. Rev. Lett. **119**, 097403 (2017).

[109] A. Delteil, T. Fink, A. Schade, S. Hofling, C. Schneider, and A. Imamoğlu. *Quantum correlations of confined exciton-polaritons*. arXiv: 1805.04020 [cond-mat.mes-hall] (2018).

[110] G. Muñoz-Matutano, D. Barrera, C. Fernández-Pousa, R. Chulia-Jordan, L. Seravalli, G. Trevisi, P. Frigeri, S. Sales, and J. Martínez-Pastor. *All-optical fiber hanbury brown & twiss interferometer to study 1300 nm single photon emission of a metamorphic inas quantum dot*. Scientific Reports **6**, 27214 (2016).

[111] K. Hennessy, A. Badolato, M. Winger, D. Gerace, M. Atatüre, S. Gulde, S. Fält, E. L. Hu, and A. Imamoglu. *Quantum nature of a strongly coupled single quantum dot-cavity system*. Nature **445**, 896 EP (2007). URL https://doi.org/10.1038/nature05586.

[112] C. S. Muñoz, F. P. Laussy, C. Tejedor, and E. del Valle. *Enhanced two-photon emission from a dressed biexciton*. New Journal of Physics **17**(12), 123021 (2015). URL https://doi.org/10.1088%2F1367-2630%2F17%2F12%2F123021.

[113] A. Gonzalez-Tudela, F. P. Laussy, C. Tejedor, M. J. Hartmann, and E. del Valle. *Two-photon spectra of quantum emitters*. New Journal of Physics **15**(3), 033036 (2013). URL https://doi.org/10.1088%2F1367-2630%2F15%2F3%2F033036.

[114] S. Schwarz, S. Dufferwiel, P. M. Walker, F. Withers, A. A. P. Trichet, M. Sich, F. Li, E. A. Chekhovich, D. N. Borisenko, N. N. Kolesnikov, K. S. Novoselov, M. S. Skolnick, J. M. Smith, D. N. Krizhanovskii, and A. I. Tartakovskii. *Two-dimensional metal chalcogenide films in tunable optical microcavities*. Nano Letters **14**(12), 7003 (2014). PMID: 25375802, https://doi.org/10.1021/nl503312x, URL https://doi.org/10.1021/nl503312x.

[115] V. Walther, R. Johne, and T. Pohl. *Giant optical nonlinearities from rydberg excitons in semiconductor microcavities*. Nature Communications **9**(1), 1309 (2018). URL https://doi.org/10.1038/s41467-018-03742-7.